Controlled Removal of Trace O_2 in an H_2 Environment of a Small-scale Electrolyser

by

Marc-Alexander Schwarze

in partial fulfillment of the requirements for the degree of

Master of Science

in Sustainable Energy Technology at the Delft University of Technology,
to be defended publicly on Friday July 17, 2020 at 13:00.

Student number:	4622804	
Project duration:	September 1, 2019 – May 31, 2020	
Thesis committee:	Dr. ir. W. Haverkort,	TU Delft
	Prof. dr. ir. S. Klein,	TU Delft
	Prof. dr. D.J.E.M. Roekaerts,	TU Delft, chair and supervisor
	Ir. J. van Kranendonk,	ZEF B.V., supervisor

This thesis is confidential and cannot be made public until July 17, 2022.

TU Delft Delft University of Technology

Abstract

Power-to-gas (PtG) technology represents a promising route in providing long-term energy security and involves pairing volatile sources of renewable energy (solar and wind energy) with alkaline water electrolysis (AWE) to create a wide range of products based on intermediate hydrogen gas for end-users across various industries such as in fuels, chemicals and power sectors. However, PtG currently lacks the technical adaptability to match the intermittency of these sources caused by daily and seasonal weather patterns, and suffers from a low turn-down ratio (TDR) as a consequence.

Zero Emission Fuels (ZEF) B.V. aim to adapt this process to create an autonomous, dynamically-operated solar panel add-on known as a *micro-plant* that will produce methanol from CO_2 and H_2O in the atmosphere. In doing so, the company looks to extend the TDR, but requires the micro-plant and by extension, its AWE unit to operate in wider partial load ranges, in which lower current densities dominate. These cause a rise in gas crossover within the electrolyser, creating impure and potentially flammable H_2-O_2 mixtures in the outlet that hinder the functionality of the micro-plant. Specifically within the AWE unit, the risk of oxygen crossover has been qualitatively identified as likely a safety hazard. Therefore, the focus of this thesis was set on studying the feasible development of a prototype (gas scavenger) that can remove trace O_2 within the techno-economic scope of ZEF's micro-plant and electrolyser.

To determine a viable method that meets ZEF's constraints on cost, size, weight and efficiency, industry techniques were studied that either purify hydrogen gas streams or destructively remove flammable H_2-O_2 mixtures. Based on a subsequent numerical estimation on each method's limiting factors, a local combustion process in the form of a *micro-combustor* was identified to be the most suitable method.

To quantitatively estimate the safety risk crossover poses, two models were developed: a non-dimensional model to analyse how 50 bar pressure influences crossover during operation, and a two-dimensional, transient diffusion model to analyse the extent of trace O_2 contamination overnight. Results indicate that to mitigate dangerous impurity levels, a gas scavenger needs to be implemented: (a) above a 0.1% difference in pressure between electrolyser half-cells during operation, and (b) upon startup to remove overnight gas accumulation that may not pose an immediate severe risk at 0.079 mol% contamination relative to amount of stored hydrogen, but has the potential to build-up on a monthly timescale.

Finally, the feasibility of the micro-combustor was preliminarily characterised at 50 bar and 80 °C through flame simulations. The variability in low amounts of trace oxygen content show that the mixture is normally non-flammable. Further studies on geometry design and control strategies of the micro-combustor must consider how to achieve optimal ignition conditions, determined to be at richer fuel mixtures between $\phi = 1.03 - 1.40$, and how to contain the flame within a well-defined region. Initial suggestions include using a small volume to induce ignition and relying on wall effects to promote flame quenching.

Acknowledgments

The work presented in this document is not just a result of my efforts over the past year, but the culmination of a long, and at times difficult journey that appeared unlikely even just one year ago, and would most definitely not have been possible without the help of an amazing support network. I stand on the shoulders of a number of these people and would not be where I am today if it were not for them.

I would like to thank the founding team of Zero Emission Fuels, Hessel Jongebreur, Ulrich Starke and Jan van Kranendonk. More than a thesis opportunity to explore a subject matter that I feel passionately about, my time at ZEF has been a positive learning experience both technically and personally. Thank you for your trust in my abilities, your positivity and support at as well as outside of work, and your mentorship that steered me out of rabbit holes when I got lost in the details.

My time at ZEF was also shaped by the amazing team mates that I was fortunate to be surrounded by. Thank you Halid, Marios, Ilias, Martin and Rebecca for lending an ear when I was unsure, for your help when I was stuck, and for the laughs over coffee, lunch or a beer.

I would like to extend my gratitude to Prof. dr. Dirk Roekaerts, whose guidance and insights led to interesting discussions, brought me clarity and helped push my work further. Thank you for your guidance throughout my thesis.

I would also like to acknowledge Dr. ir. David Vermaas. Thank you for your understanding and advice during an important time in my life that helped me reflect on my motivation and goals, bringing me to where I am today.

Ultimately, people make the place and my stay here in Delft would not be the same without the friends that I made. Thank you to Intan, Agis, Ali, Juan, Jorge, Theo, Jesse, Alex, Simona and Monica for always being a constant source of encouragement and enjoyment over the many dinners, movie nights, and journeys we had, making my experience during our master's an unforgettable one.

A special thanks goes out to Ghanshyam for his camaraderie throughout my time at TU Delft. As one of my closest friends, I want to thank you for showing up during the important moments and being there every step along the way, for the insightful discussions, memorable adventures and unconditional support you have shown over the years - never change!

Finally, the person I am today is in no small part due to the amazing support, love and care I have received from my family. This journey has been every bit mine as it has been yours. Thank you to my grandparents for always putting things in perspective and reminding me what is truly important in life. Mum, dad, Max, Tashi and Sean - I am extremely grateful for the sacrifices you made for me to pursue this programme. Thank you for always believing in me, and for the numerous phone calls and texts offering comforting words of advice and support when I needed it most, bridging the distance and time zone change between us. This thesis would never have been completed without you.

Xander Schwarze - Delft, $13^{th}\ July, 2020$

Company Profile

This study was performed in collaboration with Zero Emission Fuels (ZEF) B.V., an early-stage start-up founded at the Delft University of Technology. ZEF aims to be a front runner in the solar fuels and chemicals sector by developing a small-scale processing plant that creates renewably produced, industry-grade methanol. The company is developing a modular, dynamically operated processing plant that works as an add-on to a photovoltaic panel. An abundant source of solar energy will power the *micro-plant*, allowing it to capture carbon dioxide and water contained in our atmosphere, split this water into hydrogen gas before further reacting it with the carbon dioxide to create the target commodity. This enables ZEF to operate location independently and supports its vision of establishing off-grid solar fuel farms to bring cost-effective methanol to a growing global market.

ZEF manages its project through a subdivision into specialised engineering disciplines that equate to distinct work packages, each of which advances the development of a specific subsystem. This specialisation is key to ZEF's fast prototyping and has allowed the company to move from a successful proof-of-concept demonstration in December 2017 to its fifth iteration in a short time span, with the launch of a fully integrated micro-plant on the horizon. Recent efforts have been focused on the continuing reduction in cost (down to the order of €10^2) and weight (to ca. 12 kg) while improving upon its total efficiency (target: 55%, excluding the PV panel's performance) to hit desired manufacturing and performance markers. By opting for an innovative approach of numbering up as opposed to scaling up, ZEF plans to set up a 12 MW solar methanol farm by 2022, consisting of each 40 000 solar panels and ZEF micro-plants.

The company's vision is to contribute to shaping the renewable energy landscape by tackling fundamental, hydrocarbon-heavy industries that our society relies on, such as in chemical manufacturing, metal processing and long-haul logistics - areas that have been difficult to electrify through sustainable sources. ZEF has recognised in order to make this a reality, a multi-disciplinary approach must be researched. Therefore, a collaborative model has been adopted. It works with students, university professors as well as industry experts of varying backgrounds to conduct its work at the intersection where academia meets business, accumulating a rich foundation of both in-depth theoretical and practical expertise.

List of Figures

List of Tables

Contents

1

Introduction

1.1. Power-to-Gas Technology

1.1.1. A Global Need in a Shifting Energy Landscape

Since the adoption of the Paris Agreement in the context of the United Nations Framework Convention on Climate Change, countries across the globe have been working actively towards fulfilling their nationally set goals in minimising their carbon footprint and contributing to climate-change solutions. Although the progress made represents an important milestone in this global undertaking, power fluctuation of renewable energy sources (RES) remains a major hurdle in the realisation of a stable energy supply. With sights set on achieving 2050 targets, addressing problems of intermittency is essential to lower the barrier to market entry for an even greater share of RES [26–28].

The recent success of energy storage via batteries and supercapacitors has been a key tool in RES growth, in particular for daily grid operations [29]. The instantaneous delivery of electricity and its immediate response to changes in load demand make these technologies ideal for utilisation on shorter time scales, and will continue to play a vital role in the energy landscape [12, 29]. However, there is a growing need to provide a long-term, secure supply of energy in the form of sustainably-produced gases and synthetic fuels. These can further stabilise the grid and overcome the shortcomings of these technologies [24, 26, 30].

A promising pathway in producing these green energy storage alternatives is the introduction of coupled power-to-gas (PtG) systems. This consists of pairing volatile RES such as solar and wind energy with water electrolysis units to create a range of energy carriers. In this manner, a reserve can be secured that is independent of weather and season, offering predictability and adaptability to an evolving grid [12, 28, 31].

1.1.2. The Case for Hydrogen as an Energy Building Block

A main driver in the appeal of PtG technology is the production of green hydrogen. Its importance in its storage use is being recognised as central to a ground-up approach in achieving a highly versatile, RES-integrated energy infrastructure, meeting the demand of various end-users across many industries (Fig. 1.1) [28, 30, 32].

Firstly, as a direct energy carrier, green hydrogen can be re-electrified via fuel cells, combusted or partially fed into the natural gas grid. This route plays a vital role in heating and electricity generation sectors [28, 33]. This facilitates the increase in the grid's capacity from RES, where, unlike batteries, the delivery of power can be sustained at desired levels over longer periods [30]. Furthermore, it implies grid diversity, enabling load balancing without over-reliance on a limited number of sources, which may ease grid strain in times of peak

demand and prevent load shedding [28].

Secondly, through further processing, green hydrogen can also be converted into synthetic fuels or *e-fuels*, thereby providing a means to close the carbon-loop for long-haul freighters. This is particularly true for the aviation, shipping and trucking industries, and can play a role in powering next generation personal transport industries [26, 28, 33].

Finally, hydrogen remains an essential compound in the chemicals industry, from synthesising ammonia to methanol production, with up to 96% of the hydrogen market stemming from fossil-fuel-reliant pathways [26, 32]. Green hydrogen, therefore, can additionally play a decarbonising role as a decisive chemical feedstock [24, 28].

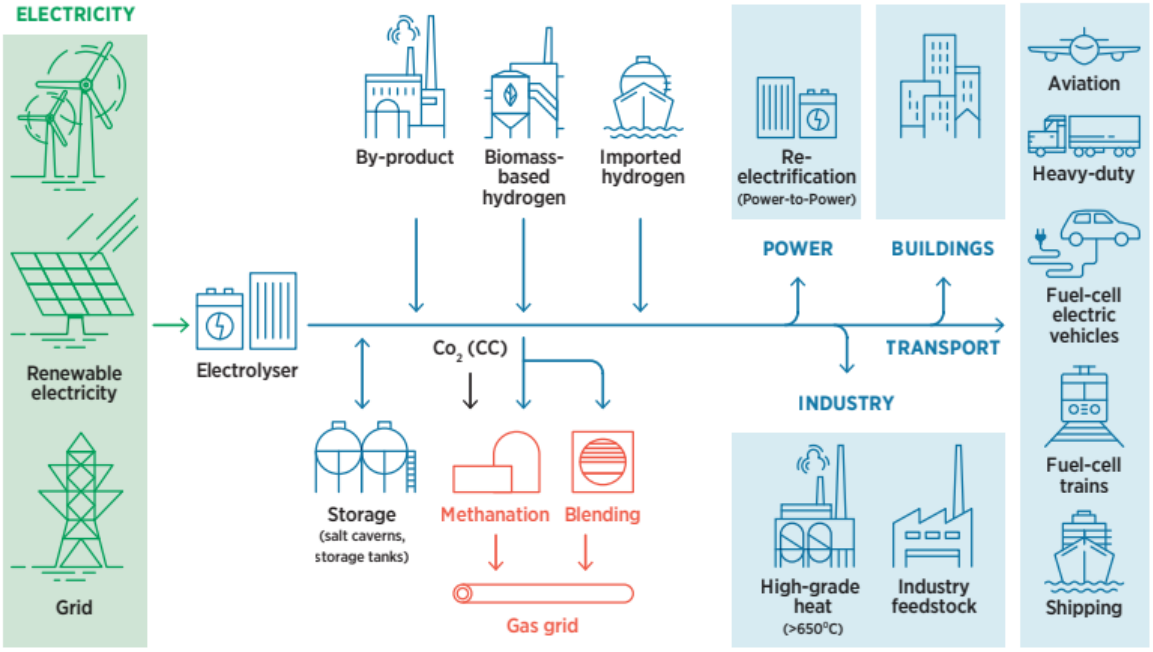

Figure 1.1: The framework of a renewable energy landscape catalysed by the introduction of power-to-hydrogen technology (electrolyser) that meets various end-users [1].

1.1.3. Technical Obstacles in Deployment

A compelling PtG option to produce hydrogen involves the use of alkaline electrolysis systems (AES). Decades worth of experience with AES has established it as the industry standard through reliable operations [27, 28, 30, 31]. Moreover, AES represent the most deployed, cost-effective choice amongst current electrolyser technologies [26] and showcase long lifetimes of up to 30 years [27].

The principle design of current generation AES, however, is intended for steady, continuous operation suited for power from the grid [26, 28]. In order for PtG to succeed in the context of green hydrogen's value chain, AES will have to function dynamically to account for a larger span of variable load inputs generated by RES [26, 27, 30]. While AES is able to respond quickly to load changes [12], it is not optimised for such operation as it suffers particularly from a low turndown ratio [28]. Presently, it is capable of running at 10-40% of its nominal load [24, 27], depending on the membrane type employed [31]. In this minimum partial-load range, inefficient lower current density profiles dominate and AES becomes prone to *gas crossover* or cross-contamination of the product gases [24, 30, 31]. This phenomenon can be

traced to electrolyte-dissolved gas species emerging in adjacent half-cells and subsequently degas. Trace amounts of oxygen appear in the cathodic chamber and hydrogen stream, termed *cathodic oxygen content*, whereas trace amounts of hydrogen appear in the anodic chamber and oxygen stream, termed *anodic hydrogen content* [21]. Crossover poses a safety hazard, reduces a PtG's capacity factor and presents a quality assurance issue.

As a safety precaution, it is common practice in industry to shutdown operations at a critical tolerance level set halfway to the upper (UEL) and lower explosion limits (LEL), forcing a shutdown in AES at 98 vol% and 2 vol% mixtures of H_2:O_2 (1 bar, 80°C), respectively [14, 24]. Therefore, to both avoid possible defects and, in worst cases, explosions, AES must be halted and purged. Given the current state of AES, this will also be necessary during start-up of coupled PtG systems to remove any (residual) contaminants that may have accumulated during down or stand-by periods following night cycles or cloudy conditions, respectively [30, 31].

From an operational expenditure perspective, crossover sets a constraint on the operating framework of PtG technology [24]. This is not only due to spent energy lost in the form of trace contaminants [30], but purging causes difficulties in restarting systems mid-operation, taking up to an hour to reset [26]. A delay in resuming operations means valuable time (e.g. sun hours, availability of wind) is wasted. This decreases the amount of hydrogen output and affects the cost of operations. Competitive pricing of green hydrogen remains an essential move towards a hydrogen based economy [32, 33]. Thus, to greatly improve the required maintenance and acceptance of coupled PtG systems, minimising the number of forced shutdowns by widening the operational range of AES and reducing start-up times is necessary [28].

Furthermore, the different aforementioned downstream processes in green hydrogen's supply chain have varying impurity tolerance levels [4, 26, 34]. Therefore, to facilitate the integration across all industries, high purity in hydrogen distribution is necessary. Addressing crossover is undoubtedly crucial in the next step of creating an RES-incorporated energy landscape.

1.2. Company Collaboration: ZEF's Role

For details regarding ZEF B.V., the reader is referred to the preface section.

1.2.1. The Micro-plant

ZEF represents an example of a company building its business model around the synthetic fuels and chemicals branches of a PtG-enabled supply chain. The company's device, a small-scale processing plant that functions as a solar panel add-on and known as the *micro-plant*, fundamentally makes use of the PtG concept to create green hydrogen through its compact electrolyser stack. However, the micro-plant is more aptly considered a power-to-liquid (PtL) technology as it extends beyond a simple PtG unit to include a wide-range of additional scaled-down processes to produce industry-grade methanol (Fig. 1.2):

- A direct air capture (DAC) unit is integrated to provide the raw material inputs by harnessing ambient atmospheric CO_2 and H_2O through chemisorption.
- A gas scrubber subsequently removes trace CO_2 dissolved in the condensed H_2O to provide a pure feed for the electrolyser.
- An alkaline electrolytic cell (AEC) further splits the water feed into O_2 and H_2, used in the gas scrubber and methanol reactor, respectively.
- A methanol synthesis (MS) reactor then combines the incoming H_2 with the captured CO_2 to produce CH_3OH and H_2O.

- A distillation (DS) unit finally separates the MS reactor's exit stream to produce high-purity methanol and recycles the water back into the AEC.

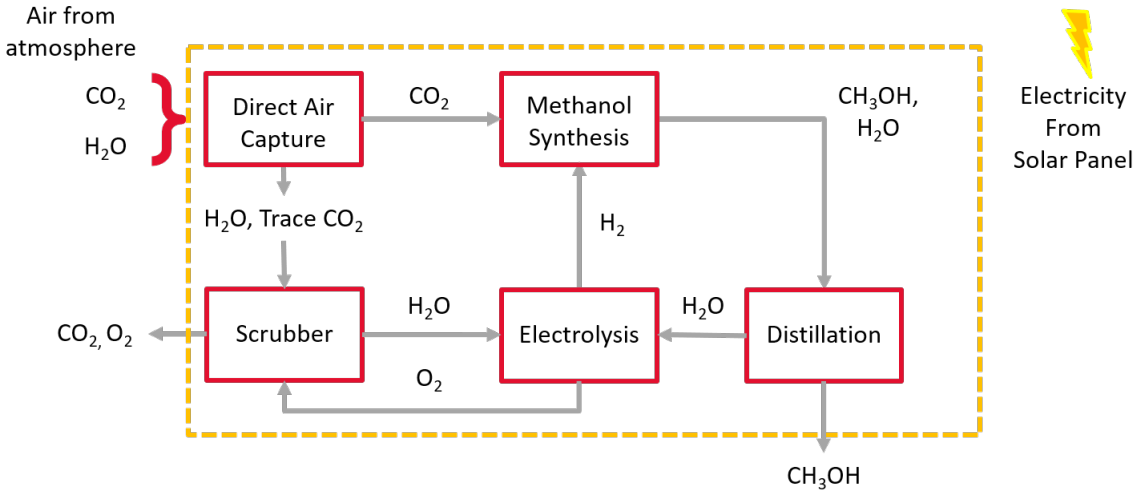

Figure 1.2: A simplified process overview of ZEF's *micro-plant*, illustrating the five main components and their respective flow streams.

The micro-plant is also equipped with a high degree of in-house-developed process control tools to maintain a high level of autonomous functionality and optimise system efficiency. Both features enable the micro-plant to operate highly dynamically, capable of responding to the sudden changes in daily weather fluctuations. In the wider context, these features are important aspects in the company's approach for off-grid solar fuel farms.

1.2.2. AEC Technical Features

Table 1.1 summarises the design specifications of the AEC. It is designed to operate in a 30 wt% potassium hydroxide electrolyte at elevated temperatures and pressures, set at 80°C and 50 bar, respectively. These parameters have been chosen to improve the kinetics, thermodynamics and ultimately, the efficiency of the water splitting reaction while also matching pressure requirements of the downstream methanol production [35, 36]. A zero-gap membrane electrode assembly (MEA) design is employed in an overall bipolar cell configuration to further improve efficiencies by reducing ohmic losses associated with the electrolyte resistance and voltage drop between the electrodes [10, 37]. *For details on the aforementioned design aspects, the reader is referred to subsection 3.1.*

These characteristics allow ZEF to create a 20-cell, compact and roughly 3.4 L electrolyser stack suited to their micro-plant layout. The membrane type applied is a Zirfon Perl UTP 500 separator membrane and the expanded nickel mesh electrodes used have been provided by Permascand AB with its proprietary coating.

Table 1.1: Principal design and operation parameters of ZEF's AEC.

Parameter [Unit]	Value
Pressure [bar]	50
Temperature [^{o}C]	80
Cell Design	Zero-gap
Target Current Density [mA/cm^{2}]	330
Target Voltage [V]	2 per cell
Electrolyte Concentration [wt.%]	KOH, 30
Electrolyte Circulation	Natural convection, separated product streams

ZEF does not employ a pump to circulate its electrolyte through the stack, but relies on the induced local differences in liquid electrolyte density caused by the evolving gas bubbles, which saves on valuable plant space and energy use. A two-phase flow of product gas and KOH emerges from each half-cell that feeds into separate hydrogen and oxygen exit streams. Each of these flows into individual flash tanks to separate the product gas from the residual KOH, which is fed back into the AEC. The hydrogen gas is collected in a 0.5 L storage tank or *buffer* before its use in the MS reactor; the oxygen is temporarily stored in the flash tank, but is consistently purged to strip the upstream carbon dioxide from the feed water during operation (Fig 1.2). As a result, gas crossover is hypothesised to accumulate much less in the stored oxygen than in the stored hydrogen. The build-up of trace contaminants, therefore, not only depends on different rates of molar production (*discussed later in chapter 3.2*), but on different time-scales caused by contrasting modes of operation and use.

1.3. Scope of Study

1.3.1. Thesis Objectives

As with industrial AES, dynamic operation poses a gas crossover problem within the context of ZEF's AEC. A previous fault tree analysis study conducted by ZEF has shown qualitatively that the build-up of trace impurities in each gas storage element can pose a likely failure point, but is particularly true for the stored hydrogen. Though trace hydrogen is likely to emerge in the oxygen flash tank, consistent purging on a minute scale averts any accumulation to dangerous levels and poses a relatively low risk in comparison to the hydrogen storage buffer that potentially allows trace oxygen contaminants to build up on an hourly or daily basis. An unwanted ignition of such a mixture as it enters the MS reactor that runs at over 200°C may not only cause a defect in the operation, but, in the case of detonation, may compromise the integrity of the buffer and reactor, and with it the entire micro-plant (Fig. 1.2).

Accordingly, at the desired level of autonomy and tolerance for variable input loads, the company has expressed its goal to expand research into understanding the effects of gas crossover on its AEC to ensure appropriate safety levels and stable process management for down- and upstream operations are met. By means of ex situ treatment of crossover species, ZEF plans to widen the turndown ratio of the AEC and, effectively, the micro-plant, to run for longer, uninterrupted periods. Therefore, the objectives of this study are:

1. to quantify and predict the degree of crossover accumulation in each product gas stream that occurs during operation and in the hydrogen buffer during downtime forced by night cycles or cloudy weather conditions;

2. to research a treatment option that enables the controlled removal of gas contamination and meets ZEF's size, cost and performance markers;

3. to investigate the chosen technology's constraints and evaluate its feasibility through process simulations.

1.3.2. Thesis Modules

Though related in topic, each objective pertains to an inherently different portion of the topic, requiring a different set of tools to address each individually. To do so, three distinct *modules* were implemented and formed the groundwork for the research conducted.

The first module involved assessing the limitations of various industry methods to remove trace contaminants, i.e. oxygen, from a hydrogen environment. A basic technical and economic analysis was performed to determine critical factors when applying these processes within ZEF's context. The assessment revealed a local combustion process to be the option of interest that was further researched.

The second module was the development of a numerical model to quantify the mass transfer process involved in gas crossover. Dominant modes of mass transfer in AES were studied from literature and the theory as well as thermodynamic properties were adapted to model crossover under ZEF's AEC operating conditions and geometry.

The third and final module involved assessing the feasibility of implementing the local combustion process to mitigate an explosion hazard caused by crossover. Here, a first study of the ignition behaviour of different H_2:O_2 compositions was made at various conditions to estimate situations that maximise a safe, deliberate burn and which give an unwanted ignition.

1.3.3. Research Questions

Accordingly, the main research question can be formulated as follows:

"Can a device be developed within ZEF's working budget and micro-plant layout that functions ex situ to the AEC's stack and successfully removes oxygen trace impurities caused by crossover?"

In the context of this work, this device will be referred to as the (gas) *scavenger*.

To help navigate this thesis work, the following guide questions were proposed:

1. What methods exist in industry to remove trace impurities from hydrogen and what are their limitations in the context of a scaled-down, off-grid and autonomous operation? (Chapter 2).

2. What causes and effects gas crossover in AES, to what extent does it cause a problem in ZEF's AEC and what models have been used in literature to simulate dominant mass transport phenomena? (Chapters 3, 4).

3. Given a theoretical framework of combustion modelling, what conditions, if any, can be set to optimally remove contaminants and what tool can be best utilised to preliminarily simulate this environment? (Chapters 3, 5).

1.3.4. Thesis Map

An overview of this thesis work is summarised in the following graphic (Fig. 1.3):

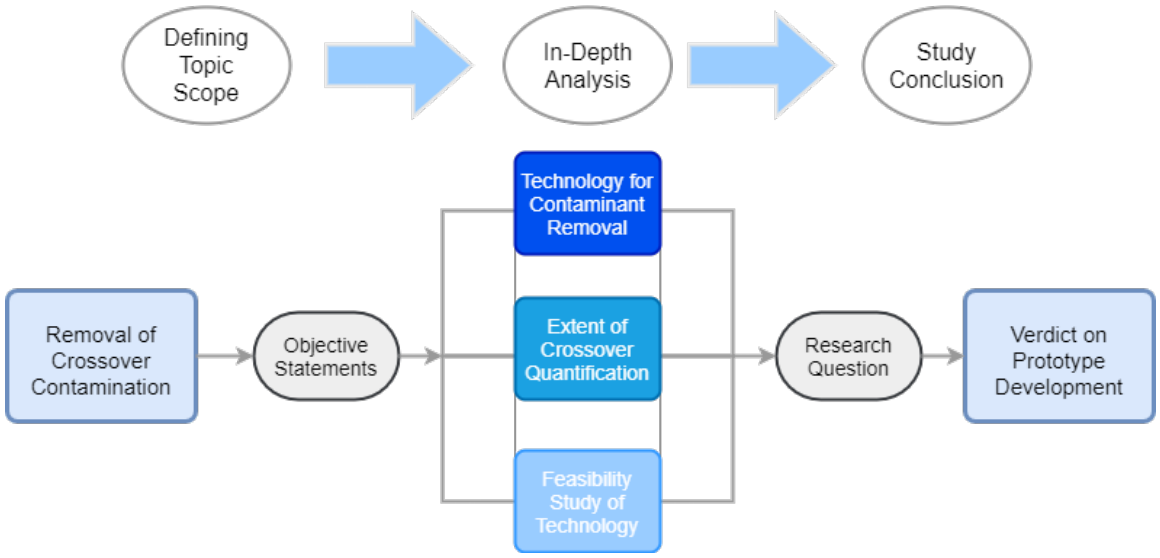

Figure 1.3: A process overview mapping out the structure of the thesis study.

1.4. Document Structure

To provide the reader with an overview, the thesis study is structured as follows. Chapter 2 presents the literature-based assessment of various purification methods discussed in the context of ZEF's microplant. In chapter 3, the technical framework and methodology applied to develop crossover models and combustion simulations are described. This includes relevant background information, governing equations, an overview describing model architecture and flow. Results of crossover mass transfer modelling are presented in chapter 4, while the preliminary results on controlled combustion modelling are presented in chapter 5. Finally, conclusions are drawn in chapter 6 and the implications for ZEF are considered. Recommendations for improved crossover model accuracy, next-stage combustion simulations and design considerations are also discussed that can pave the path for the development of a potential prototype.

2

Process Evaluation for Trace Impurity Removal

This chapter describes the assessment of viable, industrial options that can be applied to ZEF's AEC system to remove trace impurities. In section 2.1, ZEF's project requirements are defined to build a criteria framework for the assessment. Section 2.2 presents a literature-based shortlist of feasible methods. These are subsequently evaluated on critical technical or economic aspects in section 2.3 and the outcome of the evaluation is presented.

2.1. ZEF Criteria Definition

ZEF's long-term goal is to set up a 12 MW pilot plant solar fuel farm, which will consist of each 40 000 solar panels and methanol micro-plants, with the target production cost of each device set at an order of magnitude in the €10^2 range. The inherent nature of creating a fully functioning micro-plant as an add-on to a solar panel requires ZEF to operate within fine margins on the design's size, weight and efficiency. These parameters are directly linked to the cost of investment and operations, and demand the optimisation of each aspect in order to realise ZEF's business case. This applies to every technological level of the project and must be considered in preliminarily assessing a viable option for ZEF's gas scavenger.

A compatible method must, therefore, demonstrate safe scalability to smaller operations while retaining a high-degree of efficiency with respect to overall energy use and hydrogen purity. The process' complexity, defined here by the amount of auxiliary components and procedures needed to run (e.g. control systems, use of catalysts, etc.), determines how readily a method can be integrated into the existing framework of ZEF's system. It also establishes to what extent the method contributes to the total cost. Minimising process complexity is, thus, favourable. Additionally, reliability and flexibility in the treatment option's operation and design should be considered. Handling an array of varying conditions, particularly in regard to the range of impurity concentrations and variable load inputs, is important to match the dynamic and autonomous character of the micro-plant. Lastly, the lifetime of the method should be comparable to that of the AEC, spanning in the range of 10 years.

2.2. Scope of Methods

The following methods were shortlisted from an initial literature exploration and presented potential in its application for ZEF's system. Details of each method's benefits and drawbacks were compiled and are listed below. The nature and intention of these methods differs substantially and include separation techniques employed in industry, such as adsorption and

membrane technology to purify hydrogen streams, as well as destructive in-situ methods, as is the case for oxidation reactions in the catalytic recombination and ignition techniques, where the goal is to minimise the build-up of flammable mixtures.

2.2.1. Pressure Swing Adsorption

Adsorption technology remains prevalent in the (petro-)chemicals industry, among which pressure swing adsorption (PSA) is favoured as a reliable method for the supply of high-grade hydrogen purified from rich off-gas streams, such as from the steam reforming of methane [2, 34, 38]. According to Shorer et al., PSA purifies 85% of the hydrogen supply worldwide [38].

Technology Specifications

PSA is based on the principle that certain gases have higher affinities (adsorption strengths) than others to bond or adsorb to the surface of specific materials: typically, the heavier the molecule, the stronger it adsorbs (Fig. 2.1) [2, 39]. This effect is intensified at higher pressures. By utilising packed bed columns filled with adsorbent materials, such as activated carbon, molecular sieves or zeolites, the separation capacity can be adjusted and tuned to target a wide range of impurity types, offering adaptability in its design [7, 40]. PSA can reach up to 99.999% hydrogen purity, but has a H_2 recovery rate of 65-90%, with a fraction of the hydrogen lost in the purging process, and is suitable for gas mixtures containing 60-90 mol% of hydrogen [2, 38]. Generally, PSA is optimised for large scale, on-site processing with multiple columns (of up to 12) working cyclically to ensure a continuous production of purified H_2 [2, 7, 34, 38].

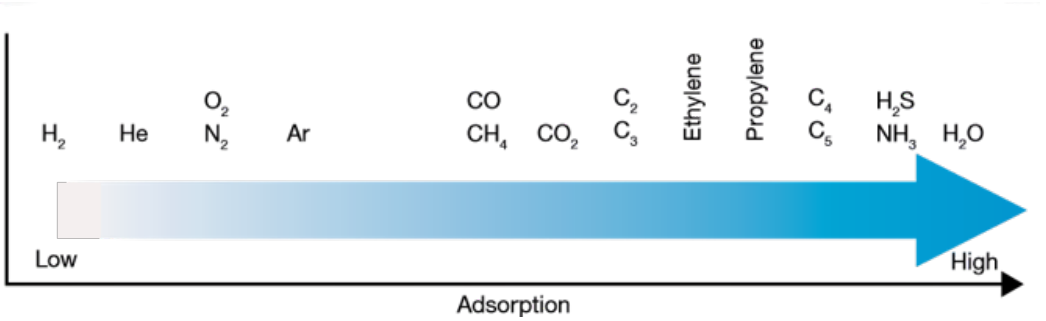

Figure 2.1: Adsorption strength spectrum of various commonly processed gases in industry. Reproduced from Air Products' report by J. Benson and A. Celin [2].

Limitations of PSA

PSA remains an energy-intensive and, thus, costly process, but cost of operations is commonly offset by its capacity to treat larger quantities of gas to take advantage of economies of scale [7, 34]. Part of the energy consumption is used towards the refrigeration system to maintain isothermal conditions within the column: it is generally operated near ambient temperatures and is necessary for reliable adsorption performance [2, 34, 39]. Though catalyst lifetimes can be assumed to last up to 10 years, inconsistent and elevated temperatures may cause sintering, reducing the surface area and deactivating the catalyst [41]. However, the largest contributor to PSA's high energy use revolves around the compression work to pressurise the gas at the inlet and maintain target pressures across column for outlet flows [34, 38]. Its operational pressure range is kept between 1-10 bar, but higher pressures of up to 40 bar can be necessary to achieve higher purity of low-H_2 containing feeds (at the expense of lower efficiencies) or match downstream process needs (e.g. storage and transportation of hydrogen) [34, 38].

2.2.2. Membrane Technology

Technology Specifications

Membrane-based hydrogen purification has attracted the interest of industry and academia alike as a cost-competitive alternative to PSA, displaying similar purities (99.999%) [42]. Based on its straight-forward, compact design, membrane purification can be easier to maintain and handle, given the reduced space and amount of auxiliary components needed, and can be simply scaled or integrated with hydrogen production steps, depending on the needs of the project [3, 42]. With higher energy efficiencies, membrane technology offers a less energy-intensive route towards the supply of purified hydrogen while displaying lower investment and operational costs over its industrial counterpart [3].

Hydrogen gas separation is driven by a difference in partial pressures across the membrane, selectively transporting a H_2 from a high partial pressure gas mixture side (feed) to a low partial pressure side (permeate) [3, 34, 42]. Membrane performance is measured in terms of its permeability and selectivity, i.e. how much hydrogen the membrane transports and how well it preferentially allows hydrogen to cross against other gas species [34].

Palladium Membranes

Though further research is consistently being conducted to bring more cost-effective and better performing membranes based on abundant materials to market, dense-metal palladium membranes control the industry space for hydrogen purification [34]. They currently outperform their porous, polymeric and ceramic analogues, and show the highest hydrogen solubility across a wide range of temperatures among other dense-metal based membranes (Fig. 2.2) [3, 34]. In addition to its high solubility, palladium membranes' appeal for commercial utilisation are based on its high hydrogen permeability and selectivity as well as its reliable and steady performance over extended periods [3, 34].

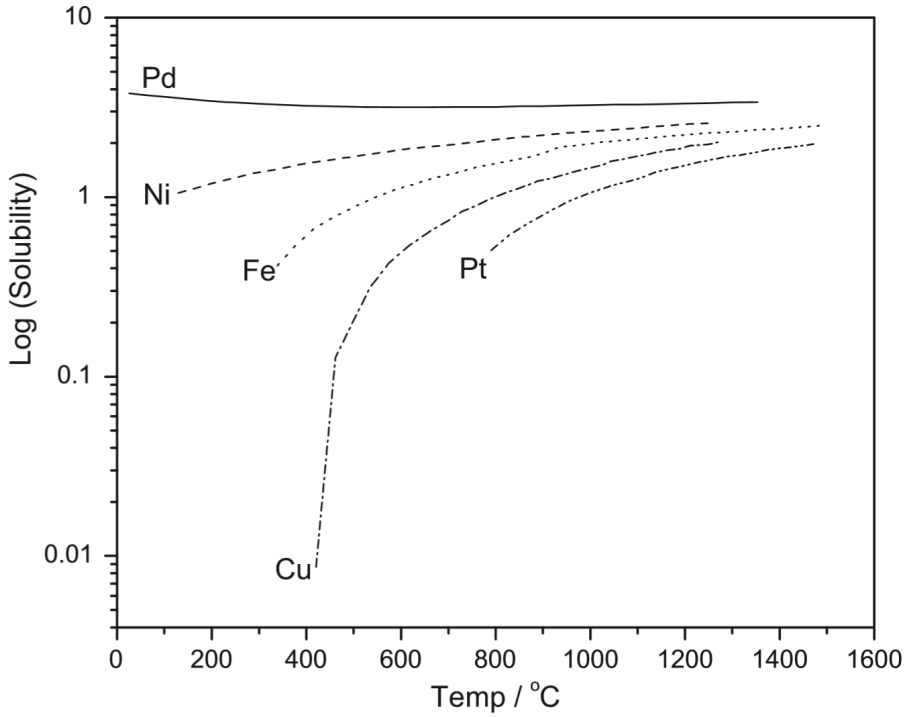

Figure 2.2: The hydrogen solubility of various dense-metal based membranes, measured at 1 atm in standard cubic centimeter (cm^3) of H_2 per 100g of metal. Reproduced from S. Yun and S.T. Oyama's work [3].

Limitations of Palladium Membrane

These characteristics are generally achieved at higher temperatures and specific pressure gradients, meaning stable performance is reliant on specific, rigid conditions. Furthermore, palladium membranes are prone to defect formation under 300 °C and 2 bar, and can also suffer from hydrogen embrittlement, a phenomenon whereby the material begins to break due to prolonged exposure to hydrogen [3, 42]. Finally, the flow of purified hydrogen is dependent on the flux across the membrane and mass transfer limitations could mean target output is not met. This can only be overcome by employing a larger membrane surface area, which can translate into higher investment costs [34].

2.2.3. Electrochemical Hydrogen Purification

Technology Specifications

Although this method is based on membrane technology as well, electrochemical hydrogen compression/purification's (EHC/P) driving force differs from pressure-gradient-based membranes and has gained new-found interest as a potential constituent in realising a hydrogen economy [42, 43]. It is, thus, treated separately in this evaluation; the focus lies on its purification capabilities.

Its operation and design are similar to that of an electrolyser and fuel cell, respectively, but instead of splitting water or producing usable work, hydrogen is purified or compressed [38, 42, 44]. An electrical potential is applied to a proton-exchange-membrane-based (PEM) MEA, which, with the aid of an active catalyst layer on each electrode, drives the oxidation of H_2 from a gas mixture to protons and electrons at the anode and recombines these at the cathode to produce a purified output of hydrogen (Fig. 2.3) [4, 34, 38]. This catalyst layer is usually made of platinum to overcome the kinetic limitations of the reactions at either side of the membrane [4, 34].

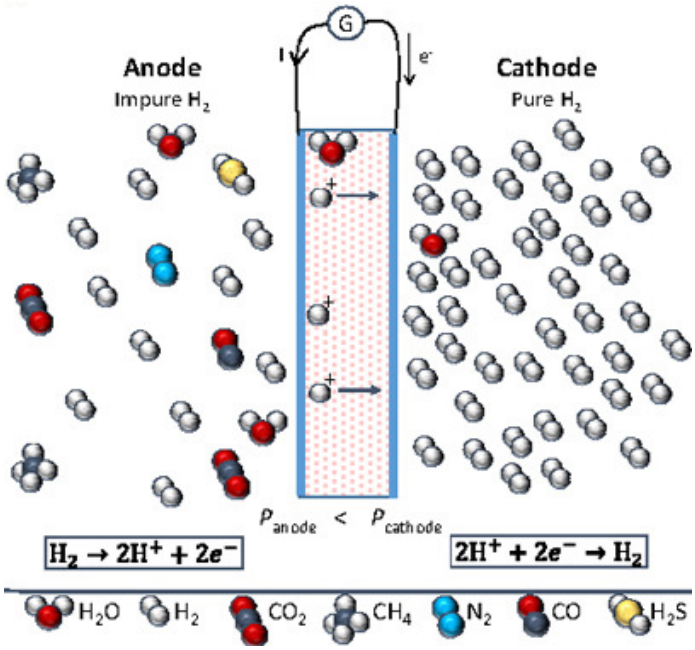

Figure 2.3: Overview of how an electrochemical hydrogen membrane functions as a compressor. Adapted from Trégaro et al.'s work [4].

EHP Characteristics

Like other membrane technologies, its compact design allows for EHP to be readily integrated into an existing framework and makes it a viable option for small scale operations [4, 34, 38]. EHP demonstrates high efficiencies and uniquely low energy use (predicted by the Nernst equation), dependent only on the potential applied, which is largely used to tackle inefficiencies that arise in practice due to ohmic resistances [34, 44]. Generally, a 100% H_2 recovery rate is reached at low temperature operations (<200°C) [34, 38]. Furthermore, EHP shows promising applications for a wide range of feed H_2 purities, with the extraction of hydrogen from low concentration feeds made possible as well [42].

Limitations of EHP

In theory, a 100% purity level is obtainable, but EHP's susceptibility to hydrogen back-diffusion and the degradation in the performance of its gas diffusion layer over time cause impurities to leak through [7, 34]. Additionally, an important factor in EHP's operation is proper water management for membrane hydration, a lack of which causes the membrane to perform erratically and unreliably [42, 44]. These factors can increase the MEA's total resistivity, which dictate the energy use, membrane area of the EHP and, in effect, the cost [38, 44].

2.2.4. Catalytic Recombination

Platinum in Industry

The effective use of platinum as a catalyst has been well documented in the automotive industry [45]. Historically used in a car's catalytic converter, platinum has gained recent attention for its utility in PEM based fuel cell vehicles as an important electrocatalyst for both the anode and cathodes of its MEA [45, 46]. Platinum exhibits optimal stability and activity towards both the anodic hydrogen oxidation and cathodic oxygen reduction reactions, and is generally considered the reference point for comparison of novel catalyst development [45, 46].

Additionally, platinum has been considered as a means to address localised hydrogen gas accumulation within the enclosed areas of nuclear power plants [47, 48]. As part of a passive autocatalytic recombiner (PAR) (Fig. 2.4), platinum's suitable affinity towards both H_2 and O_2 allow the device to catalytically oxidise or *recombine* the gases to form steam, thereby mitigating any risks of deflagration or detonation in the event of an accident [47]. Within Lopez-Alonso et al.'s simulation study, the effect of 40 PAR units, intentionally placed and spread out around a pressurised water reactor (PWR) nuclear facility's containment structure, were shown to decrease the accumulation of hydrogen by 30-45% of the final concentration [48].

PAR Considerations

The temperature of PARs needs to be monitored due to the exothermic nature of the hydrogen oxidation reaction (Eqn. 2.1), which could locally heat up sections of the device to or above the autoignition temperature of hydrogen at 500 °C [47]:

$$2\,H_2(g) + O_2(g) \longrightarrow 2\,H_2O(g) \quad \Delta H = -244.9\ \text{kJ mol}^{-1} \tag{2.1}$$

However, Sheplin et al. demonstrated that an ignition risk can be mitigated through proper process design and thermal management by incorporating a metal grid into the catalyst layer that distributes the generated heat [47]. Furthermore, as hydrogen molecules diffuse faster relative to the oxygen molecules, reliable PAR operation is strongly tied to excess oxygen conditions in order to address recombination reaction limitations imposed by mass transfer limits [47, 48].

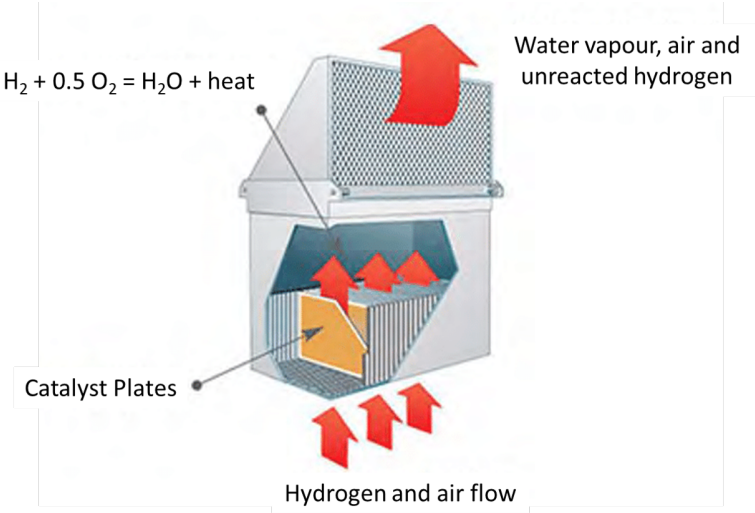

Figure 2.4: Schematic illustrating the basic functionality and common design of a passive autocatalytic recombiner (PAR) [5].

2.2.5. H_2 Ignition

Mitigation through H_2 Combustion in Industry

Although a less common method, intentional hydrogen ignition finds its applicability in fields involving high explosion hazards, where fast risk mitigation is necessary. Similar to a PAR, ignition has been proposed to control or decrease the risk of detonation posed by local gas accumulation in nuclear power plants in the event of a severe accident [49–51]. Additionally, NASA has applied a *hydrogen burn-off igniter* on rocket launchpads to nullify a chance of explosion potentially caused by hydrogen that may leak from the rocket's engines and collect by its aft [52]. In each example, the manner in which ignition was achieved or controlled differs, from the method of ignition to how the flame was quenched, e.g. by means of a flame arrester [51]. It illustrates that this method offers versatility in its execution, but also that its applicability or efficiency needs to be assessed for its intended use on a case-by-case basis, as discussed by H. Karwat [50].

Technology Specifications

The purpose of ignition is to deliberately burn off excess amounts of hydrogen to a safe level below the flammability limit at 4 vol% (for hydrogen-air mixtures at 1 bar, 20°C), taking advantage of hydrogen's wide flammability range and its low ignition energy (17 µJ at stoichiometric mixtures) [14, 49]. Safety is crucial to the operation of any combustion system, especially in the case of hydrogen, because unlike other fuels, H_2 possesses a high deflagration index - an indication of an explosion's severity - that is 10 times higher than that of methane [53].

H_2 Combustion in Micro-reactors

One approach in implementing safe hydrogen ignition is the use of micro-reactors, which involves the miniaturisation of classically large reactors. Dimensions can range from the 10^{-6} to the 10^{-2} m scale [6, 54, 55]. Generally, its scale provides a higher surface area-to-volume ratio that provides new options for reactor control over thermal and mass transfer processes.

Furthermore, a smaller volume means: (a) faster response times, which enables improved optimisation for efficiency, (b) local concentration or heat accumulation zones can more readily be devised and identified, and (c) less space and material requirements, and, thus lower energy use [6, 54]. In the context of hydrogen ignition, a micro-reactor offers inherent safety

through a reduced volume of an explosive mixture and flame arresting capabilities of the micro-channels that prevent the spread of a flame [54].

Additionally, the explosion limits that set in typically at 420 °C and 10^5 Pa for a reactor with a one meter channel diameter, are shifted towards higher temperatures through miniaturisation [54, 55]. Alone a decrease in channel diameter by a factor of 1000, i.e. to the millimeter scale, shifts the explosion limit to 750 °C, with evidence supporting a micro-reactor sees even higher shifts in temperature as well as pressure [55].

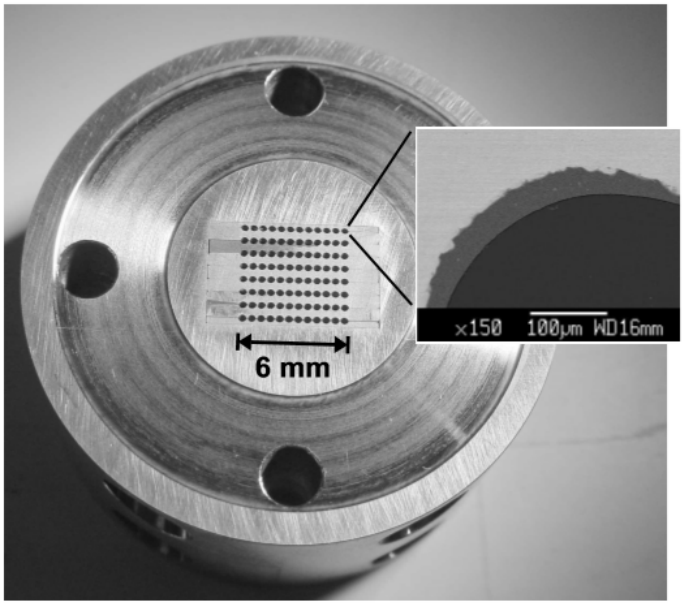

Figure 2.5: A micro-reactor example depicting 96 micro-channels, each at a length of 1.5 cm and a diameter of 400 µm, which are coated in a catalyst layer (inset) [6].

Limitations of Micro-scale Combustion

Despite the numerous benefits, manufacturing combustors or reactors at this scale requires excellent precision and may be prone to defects or be capital intensive based on the choice of materials [6, 55]. Furthermore, this method cannot be applied to a mixture if the H_2 to O_2 levels are outside the flammability limits [51].

Finally, the features that give micro-reactors shortened residence times and improved thermal control can also restrict its use: proper in-situ mixing may not be achieved while generated heat that may sustain the reaction could be lost at higher than expected rates [6, 56]. These aspects further underline the need for specific research to cater the design to the needs of the project.

2.3. Feasibility Assessment and Outcome

The purpose of the assessment was to determine a single candidate to pursue for further research. When possible, basic calculations on critical factors, technical or economic, have been carried out to gain a rough estimate on the potential impracticality of the treatment options. These results are strongly tied to the assumptions considered, but offer a quantitative insight into the bottleneck of an option. Otherwise, to identify a promising candidate, each of the aforementioned criteria (Section 2.1) was taken into consideration, providing a reference point in the discussion of credible options.

2.3.1. Pressure Swing Adsorption

PSA in ZEF's System

PSA may be the most technologically developed, but appears to be impractical for ZEF-scale operations, given its moderate to low recovery rate as well as complex management and maintenance requirements that add to integration difficulties, and the investment and operational costs [2, 38, 42]. This extends to the catalyst and its possible replacement due to deactivation, the refrigeration and the system cycle controls [2, 34, 41]. Its reliability is determined by a limited, rigid operational window that does not make it suitable for ZEF's dynamic operation [7, 38].

Theoretical Energy Use

The largest constraint pertains to its energy use, which strains the micro-plant's balance of power with only a finite output of solar energy available. To estimate to what degree this strain exists, an approximation was extrapolated based on an approach adapted from Nordio et al.'s work [7, 34], using a fitted data correlation of a single column PSA's total energy consumption. Calculations were based on ZEF's daily target production of 37.45 mol d^{-1} of hydrogen. As reflected in Fig. 2.6, total power consumption is shown to scale linearly with increased output pressures.

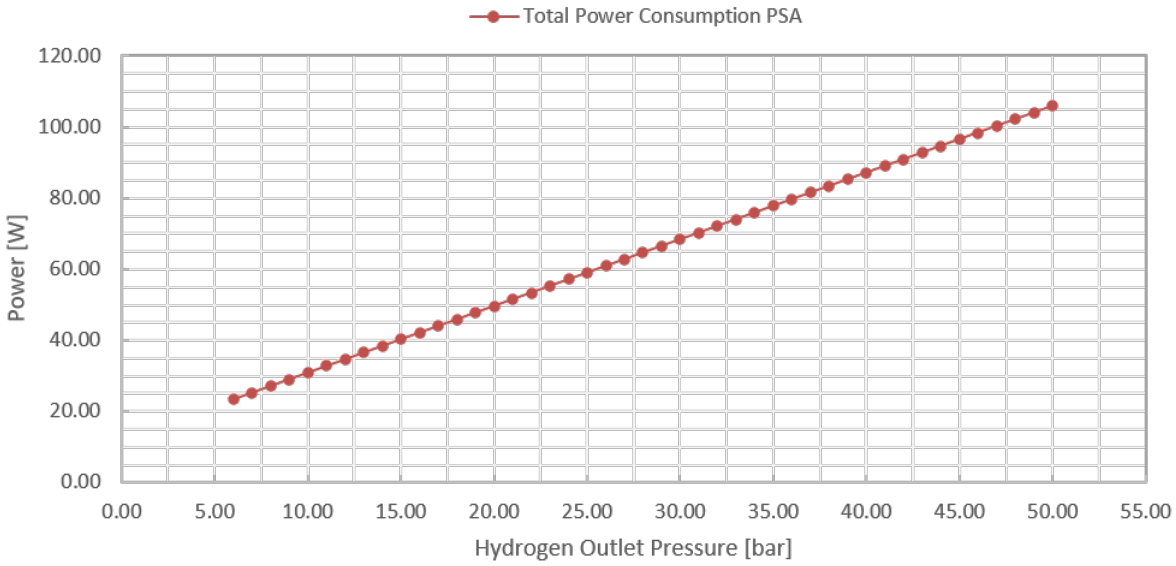

Figure 2.6: Theoretical power requirements for a single PSA column (red) in ZEF's system based on approximations by Nordio et al. [7]. Note: the fitted data set assumed an inlet pressure of six bar and is, therefore, missing data points from zero to five bar.

With this data, estimations on achieving a hydrogen outlet pressure of 50 bar for a PSA run time of two, four and eight hours were carried out. Based on a standard 360 W_p solar panel, as offered by Zonnefabriek B.V. [22], data showed that continuous operation of PSA consumes up to 29% of the PV panel's eight-hour energy output (Table 2.1). Even under the assumption of the PSA column running for a quarter of the time, it would account for just below 10% of the total energy output. As one of many components in the AEC alone, PSA was not regarded as a feasible choice due to its high energy consumption and was, therefore, not further investigated in this study.

Table 2.1: Energy consumption of a single PSA column as a percentage of total solar energy output. Estimate is based on works by Nordio et al. [7], PV panel data is adapted from Zonnefabirek B.V. [22].

Assumptions					
Sun Hours	PV Panel Peak Power	Solar Output	PSA Operation Time	PSA Total Consumption - Nordio et al.	
[h]	[Wp]	[Wh]	[h]	[Wh] at 50 bar	% of Total
8.00	360.00	2880.00	2.00	211.59	7.35%
			4.00	423.19	14.69%
			8.00	846.37	29.39%

2.3.2. Membrane Technology

Palladium Membranes in ZEF's System

In terms of commercially available membrane materials, the focus was set on palladium, which was experimentally shown to be more advanced than other membrane types and well within the expected permeability and selectivity ranges to economically compete on an industrial scale for H_2 purification [3, 42]. Its small size, overall lower energy use when compared to PSA and high efficiencies also support its implementation in ZEF's framework [34, 42]. Experimental data has also shown that though Pd-membranes have a relatively high hydrogen solubility across a wide temperature range (Fig. 2.2), performance markers were highest at elevated temperatures around 600-800K with a pressure difference of ca. 1-4 bar across the membrane [3]. Temperature regulation and compression post-membrane to maintain a 50 bar outlet pressure are, thus, necessary and complicate its integration into ZEF's micro-plant.

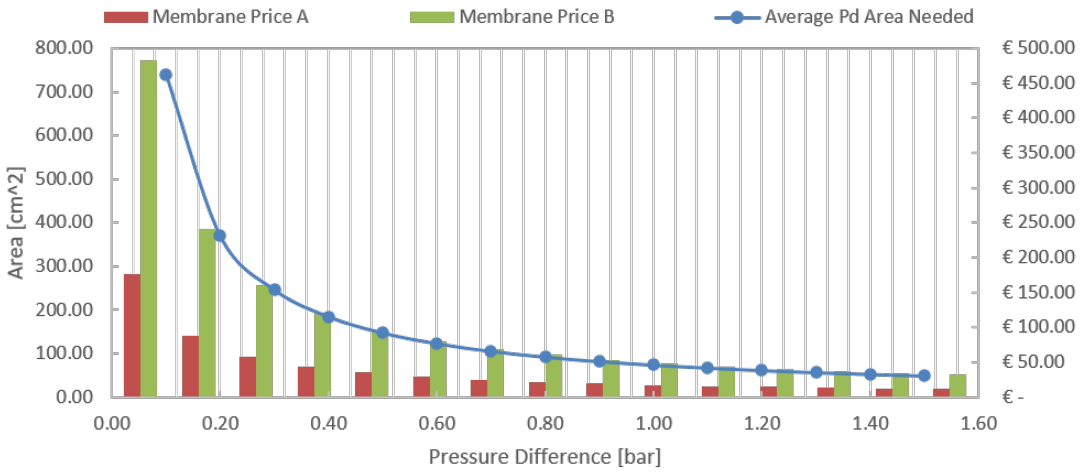

Figure 2.7: Average palladium membrane area as a function of the membrane differential pressure to drive hydrogen permeation [3]. Prices are shown relative to the required area and are adapted from: A - [8] and B - [9].

Cost Estimation

Finally, an estimate on the membrane size required to process ZEF's target 37.45 mol d^{-1} hydrogen production rate and its equivalent price was carried out based on average values collected from Yun et al.'s work [3]. An average membrane area was calculated as a function of the pressure differential across the membrane [3], along with two price estimates of palladium that represent an upper and lower bound (Fig. 2.7) [8, 9].

The calculations demonstrate that as the required pressure difference across the membrane increases, a reduced palladium area is needed, which in turn translates into a lower price. However, data from Yun et al.'s work has reflected that on average, a minimum pressure difference of 1 bar is required to drive permeation [3], and was, thus, used as the basis for cost calculations. At this condition, the data shows that a 74 cm^2 membrane per microplant is needed, and would cost on average 11 to 34% of the capital expense at lower budget ranges (€100-300 per device) (Table 2.3) [8, 9]. However, this does not take into account the replacement of membranes due to thermally induced defect formation or cracks caused by hydrogen embrittlement [3, 34, 42], which may drive the cost up further. The suitability and benefits of this method do not outweigh the difficulty in implementation and costs, and was, thus, not pursued any further in this thesis work.

Table 2.2: Total investment costs of palladium membranes as a percentage of total target CAPEX for ZEF's solar fuel farm of 40,000 units. Price estimates are adapted from: A - [8] and B - [9].

Pd Cost per Micro-plant		ZEF Target Price Magnitude per Unit	CAPEX Solar Farm Estimate Based on ZEF's Target	CAPEX for Palladium		Percentage of ZEF's Target	
A	B			A	B	A	B
€ 17.58	€ 48.25	€ 100.00	€ 4,000,000.00	€ 700,000.00	€ 2,000,000.00	17.50%	50.00%
		€ 300.00	€ 12,000,000.00			5.83%	16.67%

2.3.3. Electrochemical Hydrogen Purification

EHP in ZEF's System

Another option applicable for ZEF's small scale is EHP, which demonstrates low energy requirements, high purification efficiencies as well as the highest (theoretical) recovery rates among any of the methods considered [34, 38]. Its low temperature operation, simple design and adaptability to a wide range of conditions allow it to be easily integrated into ZEF's dynamic process [4, 34, 42]. However, its use of platinum catalysts and polymeric membranes reduces the cost-efficiency gained from its performance [34, 42].

Furthermore, impurity leaks caused by degradation of the gas diffusion layer over time and hydrogen back-diffusion remain an issue, and can intensify the loss in efficiency as well as increase the electrical power demand. Currently, few approaches exist to address these issues, but largely involve expensive equipment, which adds to the integration complexity and incurs an even greater cost [34, 43]. Additionally, this cost can be further exacerbated by EHP's volatile reliability that has been shown to be directly tied to the strict water management for membrane hydration [7, 38, 44].

EHP's Technology Readiness Level

EHC/P has seen early-stage industry exposure and is involved in a number of EU sponsored projects, with Hyet B.V. spearheading the path for widespread technology commercialisation [43]. Although the outlook is promising, more research needs to be conducted for EHC/P to compete with current incumbent industrial processes to optimise and understand operations at varying temperature and pressure conditions [38, 42]. In this respect, EHP's feasibility for

ZEF's micro-plant may be appropriate, but given its current state, has not proven to meet ZEF's criteria. The areas for further investigation include: novel membrane materials, improving process performance issues as well as cost-effective catalysis exploration. These are aspects that fall outside the scope of this thesis, thus, limiting the capacity for improvements through additional research. EHP was, therefore, discarded as an option.

2.3.4. Catalytic Recombination

PAR in ZEF's System

Platinum in the form of a PAR has been shown to be an effective close-packed, low-effort and low-maintenance alternative in mitigating explosion risks, with Shepelin et al. supporting its applications in the context of electrolysers [47, 48]. For safe implementation, the dispersion of heat formed in the process needs to be addressed through proper design considerations [47]. Its small-scale, passive operation and design flexibility support its integration into ZEF's system. However, while oxygen concentrations were found to limit the continuous operation of PAR [47, 48], additional research needs to be conducted into the limits on tolerable compositions and flow rates under 50 bar pressure conditions, and into a PAR's sizing relative to target gas throughput volumes. This should also extend to understanding the role of water management. On the one hand, steam formation contributes to the inherent safety of the PAR through dilution of explosive mixtures [48]. On the other hand, it can hinder gas diffusion to catalyst active sites, preventing the recombination reaction from taking place [47].

Cost Estimation

A final constraint on its feasibility is the cost of platinum as it is a scarce precious metal [45]. The surface reactions have been inferred from Trégaro et al.'s work [4]:

$$H_2 + 2\,Pt \longrightarrow 2\,Pt{-}H \tag{2.2a}$$

$$0.5\,O_2 + Pt \longrightarrow Pt{-}O \tag{2.2b}$$

$$2\,Pt{-}H + Pt{-}O \longrightarrow 3\,Pt + H_2O \tag{2.2c}$$

Based on recombination reaction stoichiometry, it was calculated that for a theoretical minimum of platinum[1], it would cost on average between 10 to 31 % of ZEF's capital expense at lower budget ranges (€100-300 per device) (Table 2.3) [4, 9, 23]. Though no catalyst deactivation is expected to incur a replacement cost, a PAR only represents a small constituent of ZEF's micro-plant, yet could cost up to almost a third of the investment. This coupled with its uncertainty in operation rule out its use in the AEC.

Table 2.3: Total investment costs of platinum catalysts as a percentage of total target CAPEX for ZEF's solar fuel farm of 40,000 units. Price estimates are adapted from: A - [23] and B - [9].

Pt Cost per Micro-plant		ZEF Target Price Magnitude per Unit	CAPEX Solar Farm Estimate Based on ZEF's Target	CAPEX for Platinum		Percentage of ZEF's Target	
A	B			A	B	A	B
€ 21.02	€ 39.08	€ 100.00	€ 4,000,000.00	€ 840,000.00	€ 1,600,000.00	21.00%	40.00%
		€ 300.00	€ 12,000,000.00			7.00%	13.33%

[1] This approximated value was re-calculated post-assessment for a minimum platinum amount based on the amount of oxygen crossover data obtained in Section 4.2.5

2.3.5. H_2 Ignition

Micro-Combustor in ZEF's System

As the final shortlisted option considered in this work, hydrogen ignition was not simply chosen by default through process of elimination, but its merits establish it as a promising candidate for gas crossover removal. Through controlled ignition, the oxygen impurities can be burnt off. As with the catalytic recombination, some hydrogen is lost in the formation of water, but this is outweighed by the fact that a potential risk of detonation through impurity accumulation is dealt with quickly (Eqn. 2.1) [49]. To do so, safety precautions in design and execution must be strictly considered and studied [51]. By employing a micro-reactor, for instance, it was shown that a large risk associated with hydrogen's explosive nature can be eliminated through the inherent safety of a smaller control volume, offering improved thermal and mass transfer control as well as faster response times [54, 55].

These features match the autonomous, dynamic nature of the micro-plant. Furthermore, as a micro-reactor uses up less space, energy and materials, integration can be made more accessible. Additionally, none of ZEF's overall cost, size, weight or efficiency targets would be extensively compromised [6, 54], presenting a degree of freedom in the design method. For instance, opting for dimensions at the upper bounds of the defined length spectrum would retain the advantages discussed while simplifying the manufacturing process to keep defects caused by imprecision low [6, 55]. Lastly, a micro-reactor also offers the possibility of fast prototyping, meaning the time it takes for a design to be adopted from laboratory to final use can be shortened, while scaling up is simply a matter of numbering up [6]; a modular approach inherent in ZEF's design philosophy.

H_2-Combustor as a Foundation for Further Studies

With many advantages in ZEF's case that speak for this method, a small-scale combustion process to eliminate trace impurities seems viable. Realising a device for deliberate hydrogen ignition in the AEC leads to various areas for possible further research, particularly in relation to its safe implementation, and is in line with the thesis objectives (Section 1.3.1). Process assessment, therefore, is vital and means estimating under which conditions a combustion can be controlled and not cause thermal runaway, leading to an unwanted explosion [49, 51].

Furthermore, strategies to handle impurity mixtures outside of hydrogen's flammability range need to also be considered. With an array of information on the combustion steps involved in H_2-O_2 systems, detailing elementary reactions and explosion mechanisms, these conditions can be theoretically simulated and determined [55]. A hydrogen igniter was, therefore, pursued and these aspects formed the basis for further investigation.

3

Theoretical Framework and Methodology

The following chapter describes the conceptual foundations and methods applied in this thesis work to fulfill objectives one and three (Subsection 1.3.1). The first part of this chapter initially defines basic aspects of alkaline water electrolysis (AWE) (Section 3.1), introduces main drivers for crossover in AWE in the context of crossover research performed in prior studies (Section 3.2), and reports the model approach and parameters implemented in this work (Section 3.3). Next, section 3.4 delves into the framework employed in studying the combustion of an H_2-O_2 system at ZEF's conditions, providing brief background theory and an overview on the solution procedures.

3.1. Basics of Alkaline Water Electrolysis

The following section serves to build context for the reader and covers fundamental aspects of AWE that aid in understanding ZEF's design and phenomena related to gas crossover. For more information on the general design, functionality and theory of AWE, please refer to the following sources: [10, 35–37].

AWE is operated in an alkaline medium, which in ZEF's system is a 30 wt% potassium hydroxide electrolyte, to promote the ion conductivity of the main charge carriers OH^-. These hydroxide ions are formed at the cathode through the reduction of water to hydrogen and are consumed at the anode to form oxygen and water. A membrane is generally applied between the cathodic and anodic half-cells [36, 37]. Its function is two-fold: as a salt-bridge, it allows hydroxide anions to pass through and maintain the cell's overall electrical neutrality; as a separator, it prevents each gas product from mixing [12, 37]. The system is represented by the following reactions and standard electrode potentials that need to be overcome through a minimum theoretical applied electrical work to initiate the reactions [24, 35]:

$$Cathode: \quad 2\,H_2O + 2\,e^- \longrightarrow H_2 + 2\,OH^- \qquad E^0 = -0.83\ V \tag{3.1a}$$

$$Anode: \quad 2\,OH^- \longrightarrow 0.5\,O_2 + H_2O + 2\,e^- \qquad E^0 = +0.40\ V \tag{3.1b}$$

$$Overall: \quad H_2O \longrightarrow H_2 + 0.5\,O_2 \qquad E^0 = -1.23\ V \tag{3.1c}$$

Zero Gap Design

Within the AEC, ZEF has adopted a zero gap MEA design, which involves pressing the porous nickel electrodes onto the membrane itself, thereby reducing the inter-electrode gap to the thickness of the separator. As a result, the hydroxide ions travel a shorter distance and are not hindered by gaseous products as the ions exit from the opposite electrode face from where the bubbles emerge. Therefore, a zero gap design decreases the resistance contributions from the electrolyte and related gas bubble formation that charge carriers in traditional cell designs experience (Fig. 3.1) [10, 37].

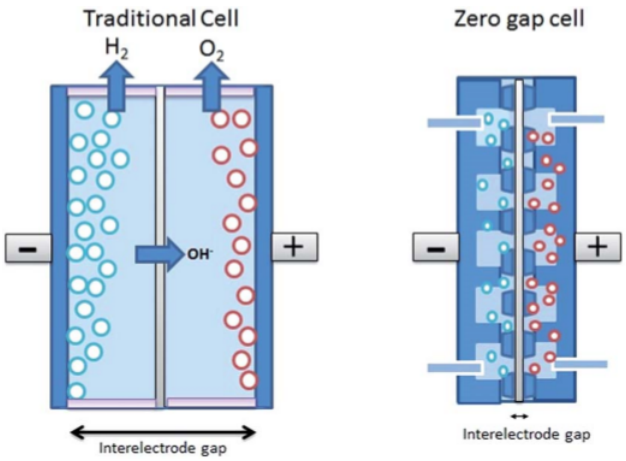

Figure 3.1: Difference in cell designs showcasing the reduction in the interelectrode gap from a traditional cell (left) to a zero-gap cell (right). Reproduced from Phillips et al. [10].

Bipolar Configuration

Furthermore, ZEF assembles or *stacks* each of the zero gap MEAs in a bipolar configuration to further reduce ohmic losses and achieve a more compact stack design [10, 35]. Such a configuration powers the stack via two end plates that are in direct connection with a DC power supply (Fig. 3.2).

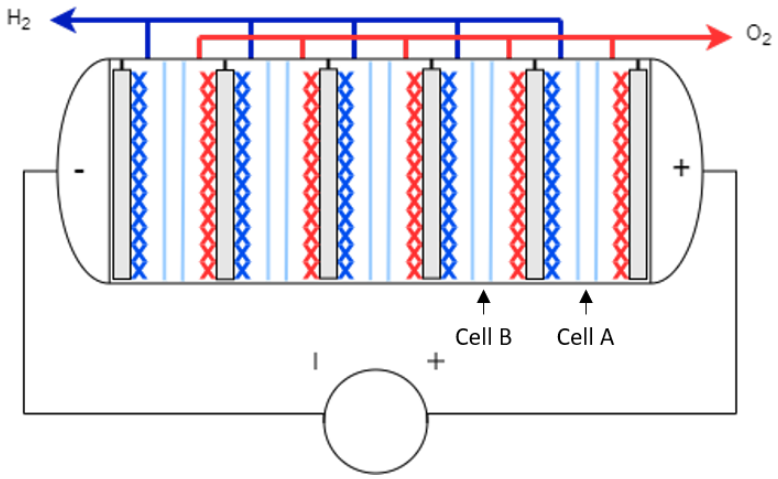

Figure 3.2: Schematic illustrating how a traditional bipolar configuration setup works within an alkaline electrolysis stack. Grey blocks - end and bipolar plates; light blue - membrane separator; blue crosses - cathode; red crosses - anode.

Across the stack, cells are segregated and isolated by bipolar plates, and remain solely electrically connected through the constant voltage drop across the electrolyte. These plates are accordingly named as the electrical connection enables both half-reactions, the lower potential cathodic (Eqn. 3.1a) and higher potential anodic reactions (Eqn. 3.1b), to simultaneously take place on each side of the plate's face. This is explained in detail through Fig. 3.2, moving from the right side of the stack to the left. To maintain the voltage drop across the stack established by the DC power supply, each individual bipolar plate experiences an effective voltage relative to its neighbouring plate. In cell A, a lower voltage is induced at the cathode (blue crosses) on the first bipolar plate relative to the end plate. This same bipolar plate, however, demonstrates a higher voltage relative to the adjacent bipolar plate in cell B and acts as the anode (red crosses). The trend continues towards the negative end plate.

By this method, cells are connected in series, implying that the voltage across the whole stack is cumulative. Based on the theoretical potential given in Eqn. 3.1c, this equates to being $1.23 \times n$ V, where n is the number of cells in the stack [10, 35, 36]. In practice though, the voltage per cell is generally larger due to ohmic losses and kinetic barriers that need to be overcome [35]. In this manner, ZEF is able to reach target electrolysis output by implementing 20 full cells, with each four-mm wide anodic and cathodic half-cells, inside the span of a 3.4 L volume.

Electrolyte Cycling Strategy

Due to the difference in stoichiometry between the half-cell reactions (Eqns. 3.1a, 3.1b), there is a net consumption of water, causing a difference in electrolyte concentrations between the anodic and cathodic half-cells, referred to as the anolyte and catholyte, respectively. To equalise this imbalance, the electrolyte flows that emerge from the stack are generally mixed and additional water is included as needed [24, 57]. This is typically known as a *mixed* electrolyte cycling strategy in literature when referring to flow management of AES. Opposite to this is a *separate* cycling strategy, whereby the emerging hydrogen and oxygen streams are replenished independently from one another - reasons for this are discussed in section 3.2.1.

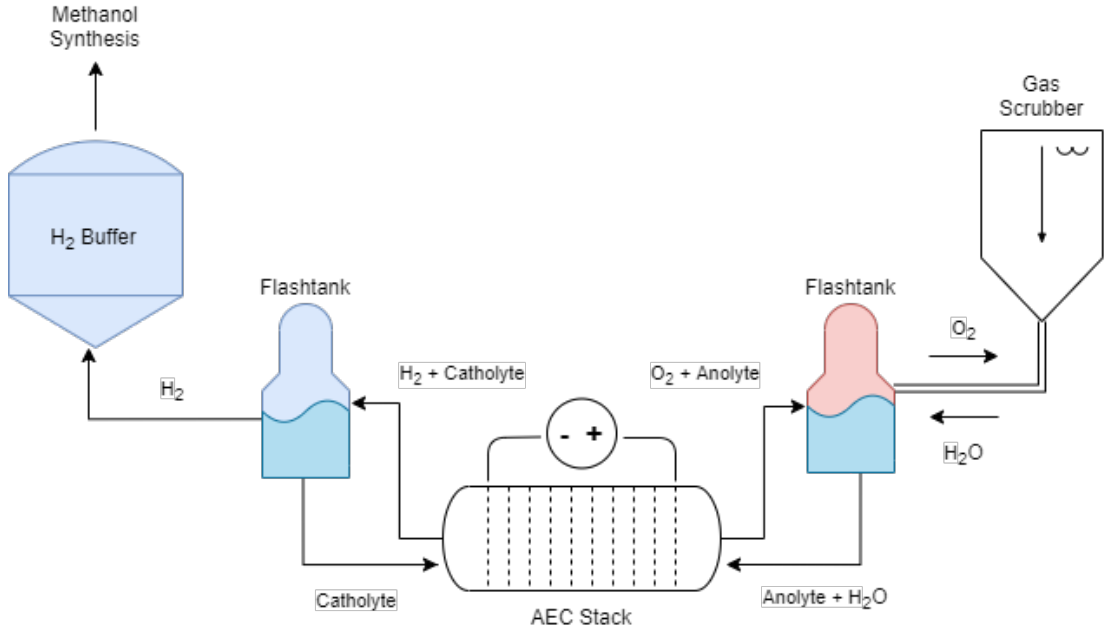

Figure 3.3: A simplified process scheme of AEC, showing the species flows and components.

AEC Cycling Strategy

In ZEF's AEC, no forced mixing is applied as no pump is utilised in the process (Fig. 3.3). Instead return feeds from each flashtank flow into a shared conduit or line at the base of the stack design that subsequently fills each half cell. By monitoring the liquid levels in each flashtank, ZEF is not only able to control the electrolyte concentrations, adding new water as necessary from the gas scrubber, but can also more readily balance the pressures within the stack.

To account for the difference in pressure build up rates due to the stoichiometry of the reaction (Eqn. 3.1c), the flashtanks are installed at staggered heights from the stack, with the oxygen flashtank (red) sitting higher. The elevation gain and rise in static pressure is used to offset the faster pressure rise in the hydrogen flashtank. These levelled adjustments, therefore, help minimise the differential pressures across the membrane separator. For this small-scale application, this method has preliminarily shown to give a higher degree of accuracy and response time in control when compared to industrial standard pressure control valves.

3.2. Crossover in Alkaline Water Electrolysis

As mentioned in subsection 3.1, a membrane separator is vital in the operation of AWE. Generally, a porous Zirfon™ Perl UTP 500 membrane separator by AGFA is employed as the industry standard [58], and has been adopted for the AEC as well. Despite its ability to be impenetrable to gaseous products (as reported by Zirfon™) [24], AWE remains susceptible to dissolved gas species crossover via various modes of mass transfer. The same properties that allow the membrane to be highly conductive and selective towards OH^- ions also make it prone to crossover driven by dissolved gas species [12, 24, 57]. The following subsection presents these varying crossover mechanisms. Depending on the operating conditions, the extent of crossover can become more severe. This is discussed in more detail, exemplified through different experimental results.

3.2.1. Mechanisms of Crossover

The modes of crossover broadly involve the mass transport of dissolved gas species and can be divided into the following categories [57]:

1. Diffusion due to a concentration gradient,
2. Pressure-driven permeation,
3. Ion-transport induced drag, known as electro-osmotic drag, and
4. Electrolyte mixing necessary for concentration equalisation.

The first three modes concern mass transport across the membrane between the two half-cells and is inherent in the nature of an electrolyser's mixed-phase flow, while the last mode occurs ex-situ to the electrolyser stack and is attributed to process design and management [12, 57].

1. Diffusion

Diffusion is driven by a concentration difference in the dissolved gas species of each half-cell and occurs through the KOH-filled pores of the membrane separator [12]. Diffusional crossover appears to be the most common mode of mass transport and has been emphasized in various works [12, 21, 24, 57]. Diffusion was, therefore, considered in this work and was

further explored in subsection 3.3.2. This phenomenon is described by Fick's law [12, 59] and relates the molar flux to the change in concentration with respect to space:

$$N_i^{fick} = D\frac{\mathrm{d}c}{\mathrm{d}x} = \frac{D_{i,\mathrm{KOH}}^{sep}}{d_{sep}} \times (c_i^{cat} - c_i^{an}) \tag{3.2}$$

where N_i^{fick} is the molar flux due to diffusional crossover in $\mathrm{mol\,m^{-2}\,s^{-1}}$, $D_{i,\mathrm{KOH}}^{sep}$ is the diffusion coefficient of the species i in potassium hydroxide within the membrane separator's pores in $\mathrm{m^2\,s^{-1}}$, d_{sep} is the membrane thickness in m, c_i^{cat} and c_i^{an} are the saturated electrolyte concentrations of species i at the membrane boundary in the cathodic and anodic chambers, respectively, in $\mathrm{mol\,m^{-3}}$. Fickian crossover is, therefore, promoted by a larger concentration difference between the half-cells or a smaller distance between the two boundaries, which in this case is the membrane separator thickness.

By this convention, the flux can either take on a positive or negative value depending on the species. In the context of hydrogen, a positive flux, represented by a higher concentration in the cathode, means that hydrogen crosses over from the cathodic chamber into the anodic chamber. In the context of oxygen, however, a negative flux, represented by a higher concentration in the anode, means that oxygen crosses into the cathodic chamber. To remain consistent, a negative diffusion coefficient was adopted in the case for oxygen ($-D_{\mathrm{O_2,KOH}}$) and utilised in subsection 3.3.2.

The diffusion coefficient used in Eqn. 3.2 is a modified parameter based on the diffusion coefficient of dissolved species in the electrolyte. The modification accounts for the effective change in the manner that each species diffuses within the membrane itself and depends on the membrane's porosity ϵ and tortuosity τ [12, 57]:

$$D_{i,\mathrm{KOH}}^{sep} = D_{i,\mathrm{KOH}} \times \frac{\epsilon}{\tau} \tag{3.3}$$

The membrane characteristics of a Zirfon™ membrane separator were adapted from literature for this study and are listed in subsection 4.2.1.

2. Differential Pressure Permeation

A difference in pressure between half-cells can force electrolyte to permeate across the membrane, and with it, the dissolved gas species contained within the electrolyte. Generally, this phenomenon is mathematically represented by Darcy's law [21, 57, 59]:

$$N_i^{darcy} = \frac{K_{sep}}{\eta} \times c_i^j \frac{(P^{cat} - P^{an})}{d_{sep}} \tag{3.4}$$

where N_i^{darcy} is the convective molar flux due to a differential pressure in $\mathrm{mol\,m^{-2}\,s^{-1}}$, K_{sep} is the hydraulic permeability related to the membrane in $\mathrm{m^2}$, η is the dynamic viscosity of the electrolyte in Pa s, c_i^j is the saturated electrolyte concentration of species i in the chamber j where it is produced (i.e. i = H_2, j = cathode or i = O_2, j = anode), $(P^{cat} - P^{an})$ represents the pressure difference between the half-cells in Pa, and d_{sep} is the membrane thickness in m.

Similar to the sign convention in Eqn. 3.2, a negative flux in the case of oxygen crossover, whereby the anodic cell pressure is larger than the cathodic cell pressure $((P^{cat} < P^{an})$, translates into the migration of oxygen species into the cathodic chamber. To account for this, a negative sign is incorporated for the ratio term of the hydraulic permeability and dynamic viscosity ($-\frac{K_{sep}}{\eta}$).

Typically, AWE pressures between the cathodic and anodic half-cells are maintained at the same level, making this type of transport phenomenon less common [12]. However, studies

conducted by Trinke et al. and Schalenbach et al. have argued that at higher pressures, this type of crossover flux may become significant [57, 58]. Their results stress the importance of pressure equalisation between half-cells for high pressure electrolysis operation. Thus, crossover due to a differential pressure has been considered in this study (subsection 3.3.2), and its effect as well as its assessed contribution to crossover from literature is further discussed in section 4.1.

3. Electro-osmotic Drag

The basis for this mode of mass transport relies on the movement of charge carriers across the membrane due to the effect of an electric field, thereby *dragging* the molecules of a polar, but electroneutral solvent with it (Fig. 3.4) [11]. Such is the case generally for parasitic water flows within membranes, and within the crossover context, the movement of OH^--ions is hypothesised to drag with it dissolved gas species [57, 59]. With a lack of studies on this mode of mass transport in the context of AWE though, electro-osmotic drag is yet to be validated or measured in its contribution towards gas crossover, but is speculated to contribute negligible amounts to overall impurities [57]. Therefore, it has been disregarded in the present work.

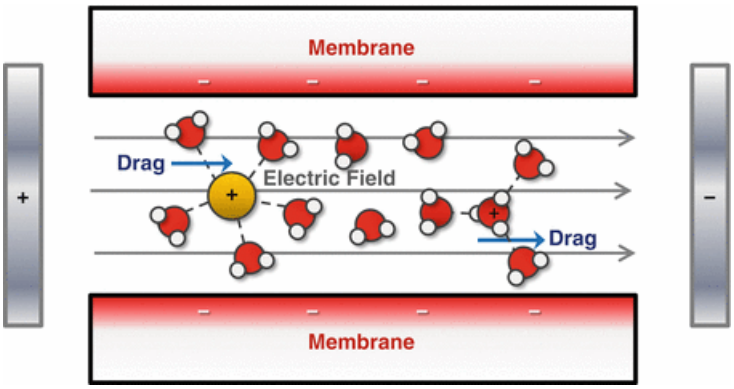

Figure 3.4: A depiction of the electro-osmotic drag effect inside the pore of a membrane, where different ions (indicated by their positive charge) are dragging solvent molecules across the membrane. Adapted from [11].

4. Mixed Electrolyte Cycling Strategy

In contrast to the previous three modes that are inherent to the functionality of electrolysis, this type of contribution towards crossover represents a source that can be addressed through process management. As mentioned in section 3.1, catholyte and anolyte streams emerging from the cell are blended together and replenished with fresh water as necessary to maintain equal electrolyte liquid levels and concentrations within each (half-)cell (Fig. 3.5). However, as each separate electrolyte stream carries a dissolved gas species within it, each cell becomes saturated through the mixing process with a *foreign* species that eventually degasses and contributes to impurities in product gas [12, 24, 57]. A mixed cycling strategy has been found to be the largest contributor to gas crossover [25, 57], and can be minimised by opting for longer periods of a separate cycling strategy with intermittent intervals of a mixed cycle.

The strategy adopted within ZEF's AEC does not strictly fall into either of these categories discussed in literature: the lack of a pump means mixing due to convection is substantially reduced, while the direct line of contact between anolyte and catholyte streams introduces the possibility of mixing. The assumption is that due to an absence of forced convection and smaller flow rates within these return lines (Fig. 3.3), convective mixing could be at a lower order of magnitude, potentially comparable to slower, diffusive mixing effects. Current

research within ZEF on the control and operation of the AEC stack is addressing this issue in more detail. For the purpose of this study, an effective separate cycling strategy was assumed.

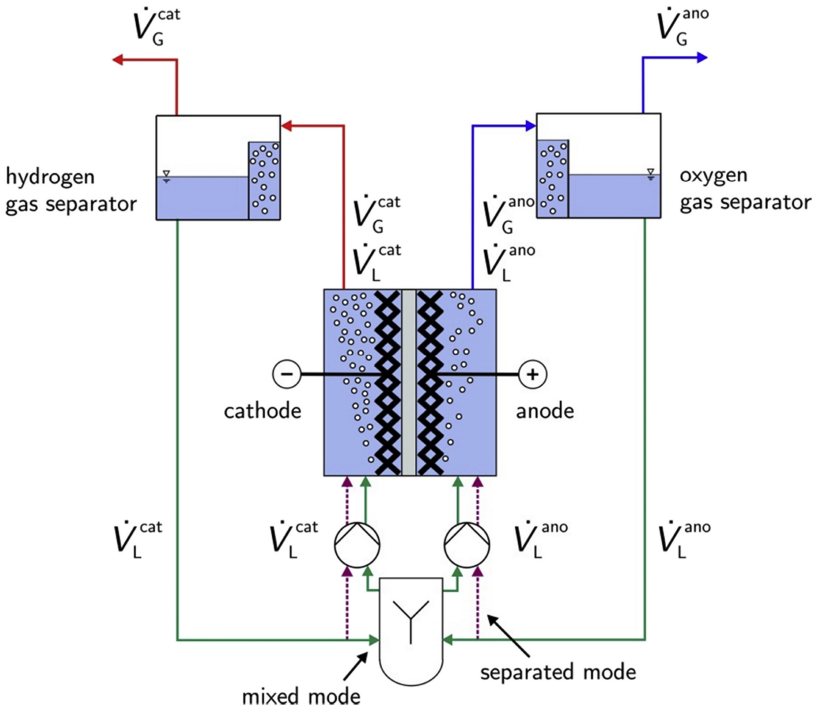

Figure 3.5: An example of a process scheme that includes mixed and separated cycling options, indicated by green return lines and dotted purple lines, respectively. Adapted from Haug et al.'s study [12].

3.2.2. Dissolved Gas Concentration Predictions

Fundamental to these modes of mass transport is estimating the amount of gas that is dissolved in the KOH solution. Two phenomena contribute to the saturated concentration build-up within the electrolyte: gas dissolution and supersaturation.

Gas Solubility Model

To predict the gas dissolution, the solubility of hydrogen and oxygen in a potassium hydroxide solution must be determined. However, prior work on this solubility data, particularly at the given concentrations and temperature ranges, are limited. Though the solubility of these species is generally low in the electrolyte, estimating equilibrium concentrations of the dissolved gas is important for proper modelling and assessment of gas crossover accumulation [12, 57]. To estimate these values, a combined solubility model was formed in Haug et al.'s works, and has been adopted for this thesis work as well [12, 24, 25]. Within the solubility framework, Henry's law predictions in pure water were modified through various empirical correlations from fitted data specific to potassium hydroxide, such as the Setchenov relation, to estimate dissolved gas equilibrium concentrations within the electrolyte [12, 24]. The details of this model can be found in Appendix A.2.

Supersaturation

Supersaturation is a condition that occurs in the boundary layer of the electrode and plays an important role in the formation of gaseous electrolysis products [60]. Generally, gas species such as oxygen and hydrogen are initially formed in a dissolved state at the electrode as a

precursor to its gaseous forms [12, 61]. These remain in an equilibrium with their gaseous counterparts that favours its dissolved state:

$$2\,H_{dis} \rightleftharpoons H_2(g) \tag{3.5}$$

For bubble growth to be initiated at the electrode's active sites (*nucleation sites*), a shift in the equilibrium must be established [12, 57]. This is achieved through supersaturation (Fig. 3.6), whereby the concentration of the electrolyte layer in the direct vicinity of the electrode becomes higher than values predicted by Henry's law [57, 60, 61], with studies showing a five- to 165-time higher concentration [24]. As described by Le Chatelier's principle, the system looks to re-equilibrate to build off the excess concentration, thus, shifting the equilibrium towards the formation of gaseous hydrogen:

$$2\,H_{dis} \rightleftharpoons H_2(g) \tag{3.6}$$

This signifies that the formation of bubbles depends on the mass transport of dissolved species to the nucleation sites that competes with the transport of the dissolved species to the bulk of the electrolyte [12, 57]. This aspect is of particular interest in a zero-gap design as it implies that dissolved species due to supersaturation may cross the membrane, thereby establishing a potentially larger diffusional crossover [24, 57]. Supersaturation and its effect on crossover has, therefore, been taken into considerations in this study (Section 3.3.3).

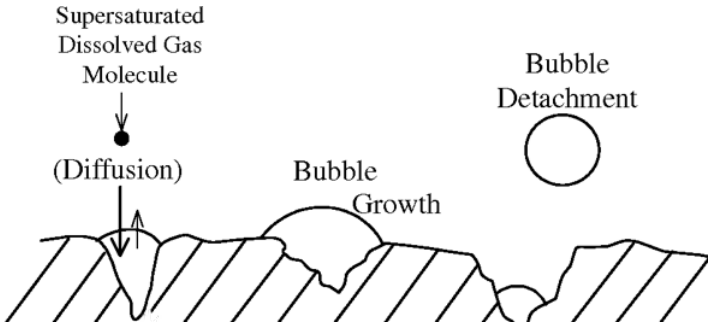

Figure 3.6: Sequence of bubble formation, growth and subsequent detachment under supersaturated conditions. Re-created from Scardina et al. [13].

3.3. Crossover Model Development

3.3.1. Current State of Crossover Modelling Research

Various studies have been conducted in understanding AES, focusing on a range of areas from improved electrode material design to modelling the output and performance of specific systems already deployed in the field. Studies towards crossover research in AWE, however, remain limited and have mostly only constituted a minor section of a larger research topic. This appears to be especially true for the mathematical modelling of crossover, where distinctly few unique approaches currently exist. Examples of these have been highlighted in the following works.

Empirical Correlation

Sánchez et al. considered a diffusion model to describe the hydrogen to oxygen (HTO) crossover within the context of an alkaline electrolyser model on Aspen, simulating both the stack and auxiliary components to assess overall performance. The diffusion model was an empirically fitted parametric correlation based on previous obtained crossover data and was a function of temperature, pressure and current density. Their work demonstrated that the HTO

diffusion model predicted the effects on gas purity to within 1% of experimental values, and reflected a proportional increase in gas impurities as temperature and pressure were scaled [62].

Parameterised Crossover Mechanisms

In Schalenbach et al.'s work, a basic gas crossover model to be implemented on Excel, OriginLab or MATLAB was developed within the wider context of a model to characterise key aspects and differences between PEM-based electrolysis and AWE at 6 bar and 80°C. The model considered two distinct and separate scenarios: one in which crossover was dominated by diffusion (Fick's law) and one in which crossover due to a differential pressure across the membrane dominated (Darcy's law). Similar to Sánchez et al., important parameters were experimentally determined for each mode of mass transport. Results showed that at an assumed 1% absolute pressure difference between the cathodic and anodic cells, gas purity was most affected by crossover due to differential cell pressure, implying the need for proper pressure balance and separators with smaller pore diameters [21].

Process Simulation Method

Haug et al.'s approach was based on a zero dimensional chemical process engineering method, in which a single electrolytic cell's anodic and cathodic chambers as well as auxiliary components were represented by a two-phase flow within two interconnected CSTR tanks. The model was developed to study the effects of gas purity, particularly in the low current density range, as a function of various system parameters, such as: current density, temperature, electrolyte flow rates and concentrations, as well as the type of electrolyte cycling strategy employed. Like aforementioned approaches, the model was validated through experimentally conducted work. Parameters, however, were fitted from relevant data sets found in previously conducted studies. Despite some model limits, the model successfully demonstrated the gas purity's dependence on various system parameters, the most evident of which is the effect of a mixed cycling strategy [12].

Foundation for Modelling in ZEF's Context

The three presented works represent a spectrum of varying model complexities and scopes (i.e. complete empirical parameterisation versus design equations of physical laws). Though gas crossover is (part of) the focus in each approach, the intention of each model differs slightly, against which the success of its implementation is measured. Furthermore, each model's accuracy is limited to the assumptions imposed upon it.

Taking these factors into consideration, an approach was developed to model gas crossover within ZEF's AEC, drawing upon aspects from each aforementioned study. While an extensive multi-scale model can be a powerful tool, it generally takes substantial effort and time to develop its architecture and implement. Therefore, similar to Schalenbach et al. [21], scenario building was adopted for crossover analysis in this work. This enabled the development of two specific models, namely to address crossover during in-operation conditions (Subsection 3.3.2) and during extended reactor downtime (Subsection 3.3.3), the latter of which is currently absent in literature and vital to ZEF's safety risk assessment in its autonomous, dynamic operational design. Furthermore, as the appeal of PtG technology grows in the context of a hydrogen economy, crossover modelling of dynamic systems may become an invaluable tool in future project evaluation.

3.3.2. In-Operation Model

Objective and Considerations

The objective of this approach was to mathematically model what effects crossover due to diffusion and pressure-driven cross permeation have on gas purity during in-operation mode

of ZEF's AEC at conditions of 80 °C and 50 bar. The principles utilised were an extension of Schalenbach et al.'s zero-dimensional approach [21].

The focus was specifically set on understanding the extent of crossover caused by a differential pressure between the cells at 50 bar. Previous studies have indicated its substantial contribution to the overall crossover at 6 bar operating pressure and at a 1% absolute pressure difference, the listed inaccuracy tolerance of the pressure controllers used in their work [21, 57]. Further studies by Schalenbach et al. remarked that this effect scales quadratically with increasing pressure, meaning at a 50 bar operating pressure, a 0.5 bar pressure difference can equate to a 2500 time larger crossover effect than at atmospheric pressure [58]. The adapted approach was extended to include inaccuracy tolerance levels of 1%, 0.5% and 0.1% pressure difference between the cells.

Equations

To estimate gas purities in each half-cell's outlet gas stream, the mathematical expressions for the concepts of anodic hydrogen content (AHC) and cathodic oxygen content (COC), both measured in mol%, mentioned in subsection 1.1.3 have been introduced:

$$AHC: \frac{N_{\mathrm{H_2}}^{cross}}{N_{\mathrm{H_2}}^{cross} + N_{\mathrm{O_2}}^{an}} \times 100\% \tag{3.7a}$$

$$COC: \frac{N_{\mathrm{O_2}}^{cross}}{N_{\mathrm{O_2}}^{cross} + N_{\mathrm{H_2}}^{cat}} \times 100\% \tag{3.7b}$$

where N_i^{cross} represents the molar crossover flux of species i as predicted either by Fick's law (Eqn. 3.2) or Darcy's law (Eqn. 3.4) in $\mathrm{mol\,m^{-2}\,s^{-1}}$. These quantities are normalised to and refer to the area of the membrane. N_i^j represents the molar production rate per area of species i at the electrode in half-cell j, measured in $\mathrm{mol\,m^{-2}\,s^{-1}}$, as predicted Faraday's law [12, 21]:

$$N_i^j = \frac{\nu_i^j \times J}{z \times F} \tag{3.8}$$

where ν_i^j is the stoichiometric coefficient for the electrolysis reaction (Eqn. 3.1c, $\nu_{\mathrm{H_2}}^{cat} = 1$, $\nu_{\mathrm{O_2}}^{an} = 0.5$), J is the current normalised to the electrode area (current density) measured in $\mathrm{A\,m^{-2}}$, z is the number of electrons exchanged in the reaction (Eqn. 3.1), and F is the Faraday constant equal to $96485\mathrm{C\,mol^{-1}}$.

Finally, with a lack of experimental data for parameters used in Eqns. 3.2 and 3.4, values were adopted from Schalenbach et al.'s work [21]. These pertain specifically to the membrane permeabilities for Fick- and Darcy-based crossover, which were more readily determined than diffusion coefficients or dynamic viscosities, for instance, combining multiple unknowns into a single, measurable quantity. In order for this quantity to be applicable, alternative forms of Eqns. 3.2 and 3.4 were selected, where partial pressures were used in place of saturation concentrations as listed in section 3.2. The reader is referred to Appendix A.1 for details.

Assumptions

The following assumptions were made:

- Isothermal and isobaric operation at 80 °C and 50 bar, respectively.
- No ex-situ mixing of electrolyte occurs, meaning a separate cycling strategy is adopted.

- The mode of mass transport is either dictated by diffusion or pressure-driven cross permeation individually, meaning N_i^{cross} is either predicted by Fick's law or Darcy's law. A combined contribution is not considered.
- For the case where diffusion crossover dominates, crossover does not accumulate in the opposite cell as it completely degasses and acts as an infinite sink. This means its term contribution in Eqn. 3.2 is negligible, e.g. for H_2 diffusion, $c_{H_2}^{cat} >> c_{H_2}^{an}$, therefore, $c_{H_2}^{an} \rightarrow 0$. This can be analogously derived for oxygen diffusion.
- If cross-permeation due to a pressure differential controls crossover, then it is assumed that $P^{cat} > P^{an}$ for hydrogen crossover and $P^{cat} < P^{an}$ for oxygen.
- The geometric area of the electrode is equal to the geometric area of the membrane to maintain consistency (Eqns. 3.7).

3.3.3. Reactor Downtime Model

Objective and Considerations

The objective of the reactor downtime (RD) model was to simulate to what extent crossover (a) accumulates in the AEC's components and, (b) poses a deflagration or detonation risk in the AEC's stored gas units during extended periods of reactor downtime (RD), such as during cloudy weather conditions or overnight.

A two dimensional, numerical analysis approach was used to develop a transient, diffusion model that considers the mass transport involved in the re-dissolution of stored gas into the electrolyte as well as in the crossover migration of dissolved species across the membrane. A supersaturation condition has also been considered in the direct vicinity of the electrode to understand the hypothesised increase in diffusional crossover [24, 57]. Lastly, the effect of cell geometry on gas crossover was studied by halving, doubling and tripling the cell width from ZEF's original 4 mm design.

Using physical dimensions of ZEF's AEC, three dimensional objects were projected onto two-dimensional space to represent real components in the form of a flexible mesh. Finally, as this model was intended to be a more extensive approach than the previous in-operation model, the parameterisation of thermodynamic fluid properties from Haug et al.'s work was more suitable [24], among which are diffusive properties and saturation concentrations, listed in subsection 4.2.1.

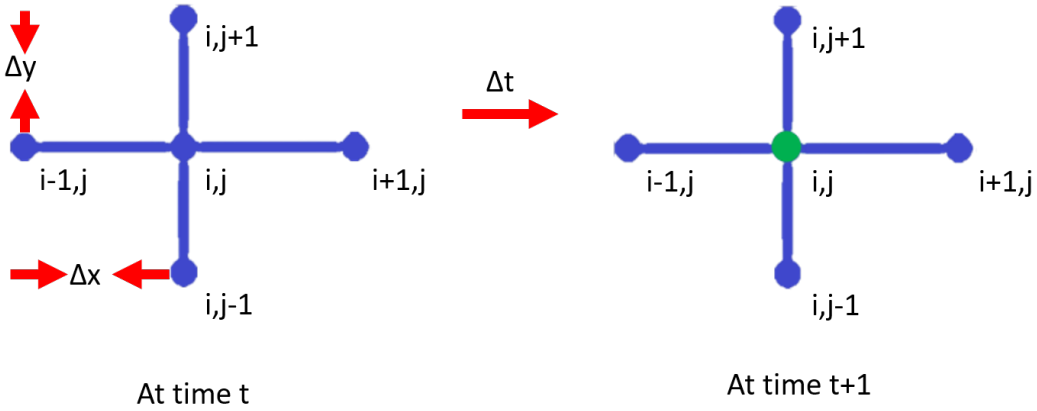

Figure 3.7: Graphical representation of FTCS scheme applied to point i,j (left). Its nodal value is updated and overwritten as time progresses t+1 (right, green).

Equations

To describe the transient diffusion system in a two dimensional domain, a finite difference method (FDM) based on a forward in time, central in space (FTCS) scheme was used to approximate Fick's second law of diffusion (Eqn. 3.9b), which relates the change in diffusion flux within the electrolyte (Eqn 3.9a) with respect to space to the change in its concentration with respect to time. Based on a Taylor series expansion, FDM utilising a FTCS scheme enabled the partial differential diffusion system to be spatially (Δx, Δy) and temporally (Δt) discretised on an m by n uniform grid or mesh (Eqn. 3.9c). By doing so, the partial differential equation is transformed from a continuous function into a series of definite or *discrete* portions in the form of elements or *nodes* of the mesh, upon which a concentration value c is assigned at a specific point in time t, $c_{i,j}^{t}$. The node at the next time step, $c_{i,j}^{t+1}$, can then be explicitly solved for (Eqn. 3.9d), iteratively updating each node's value for a total specified time interval [63]. As this process and equation is repeated over every node, it is typically referred to as a *stencil*.

$$N_{x,\mathrm{KOH}} = D\frac{\mathrm{d}c}{\mathrm{d}x} \tag{3.9a}$$

$$\frac{\partial c}{\partial t} = \frac{\partial N_{x,\mathrm{KOH}}}{\partial x} + \frac{\partial N_{y,\mathrm{KOH}}}{\partial y} = D\left(\frac{\partial^2 c}{\partial x^2} + \frac{\partial^2 c}{\partial y^2}\right) \tag{3.9b}$$

$$\frac{c_{i,j}^{t+1} - c_{i,j}^{t}}{\Delta t} = D\left(\frac{c_{i+1,j}^{t} - 2c_{i,j}^{t} + c_{i-1,j}^{t}}{\Delta x^2} + \frac{c_{i,j+1}^{t} - 2c_{i,j}^{t} + c_{i,j-1}^{t}}{\Delta y^2}\right) \tag{3.9c}$$

$$c_{i,j}^{t+1} = \alpha(c_{i+1,j}^{t} + c_{i-1,j}^{t}) + \beta(c_{i,j+1}^{t} + c_{i,j-1}^{t}) + (1 - 2\alpha - 2\beta)c_{i,j}^{t} \tag{3.9d}$$

where $\alpha = D\frac{\Delta t}{\Delta x^2}$ and $\beta = D\frac{\Delta t}{\Delta y^2}$, with i+1 and j+1 taken to mean a step across the column and up the row, respectively. This corresponds to a step in the x and y direction (Fig. 3.9), respectively, but goes against the m by n indexing of a matrix.

Applying an FTCS scheme enables a relatively high degree of accuracy, minimises the truncation error (associated with disregarding higher order terms in a Taylor series expansion) and computer-related rounding inaccuracies, while also reducing computational time due to its explicit form [63, 64]. Mesh resolution, i.e. the choice of step size for Δx and Δy, is key to the accuracy and validity of the model, but is just as important for time discretisation as FTCS is only conditionally stable under the following condition [63, 64]:

$$\Delta t \leq \frac{\Delta x^2 \Delta y^2}{2D(\Delta x^2 + \Delta y^2)} \tag{3.10}$$

which limits the size of the time step. Therefore, appropriately sizing the mesh means balancing the trade-off between model accuracy of a high resolution grid, shorter computation time and stable convergence of a solution.

Finally, to account for supersaturation and analyse its effects on diffusional crossover, a supersaturation factor was applied to the nodes closest to the MEA boundary for oxygen and hydrogen, whereby the concentration predicted by Henry's law was simply multiplied by the supersaturation factor as performed by Haug et al. [24].

Assumptions

The following assumptions were made:

- The modeled AEC components include: a single electrolytic cell that comprises of an anodic and cathodic chamber, two pipes that each connect each half-cell to the oxygen and hydrogen flashtanks, and the hydrogen buffer.
- Under the assumption that a separated cycling strategy is valid, return and equalisation lines are neglected (Fig. 3.3).
- In-operation crossover does not accumulate within the cell, meaning upon shutdown (t = 0), adjacent half-cells are assumed to have no concentration of crossed over gas.
- Mass transport due to convection is neglected at all times t as it is assumed to stop immediately upon shutdown. With a lack of generation, no further bubbles will be formed at the electrodes to induce further convection and it is assumed that the majority of the bubbles will have degassed after an initial short period.
- Isothermal and isobaric operation at 80 °C and 50 bar, respectively, are once again assumed. This is important as certain thermodynamic parameters adopted from Haug et al. are only valid at this specific temperature, given that they were empirically fitted from literature data sets [12]. A lack of a thermal gradient means these properties are constant throughout the entire system.
- Any mass transfer resistances imposed by the hindrance of the electrodes' surface related to the membrane crossover are neglected, i.e. the MEA comprises effectively of only a membrane.
- Due to the thickness of the membrane (in the order of 5×10^{-4} m), flux across the membrane is assumed to be described by its x-directional component, whereas its y-directional component is assumed to be negligible.
- Within all elements of the computational domain, mass is conserved. Following this principle, the flux across and out of the cathodic chamber is assumed to be equal to the flux into and across the anodic chamber in the case of hydrogen crossover. This is assumed to also be valid for the reverse direction in the case of oxygen crossover.

$$|N_i^{fick}|\Big|_{x=cat} = |N_i^{fick}|\Big|_{x=an} \tag{3.11}$$

- Saturation concentration variable c (in mol m^{-3}) corresponds to $c_{H_2}^{cat}$, $c_{H_2}^{an}$ when hydrogen crossover is modeled, and corresponds to $c_{O_2}^{cat}$, $c_{O_2}^{an}$ when oxygen crossover is considered. The same applies for diffusion coefficients D as $D_{H_2,KOH}$ and $D_{O_2,KOH}$ (in $m^2\,s^{-1}$).
- The variable t represents the elapsed time after the AEC has been shutdown and is given in s.

Initial and Boundary Conditions

In addition to initial conditions that provide a starting value for each node at t=0, boundary conditions need to be defined to not only more accurately represent physical conditions that reflect real system behaviour, but to also allow proper implementation of FDM.

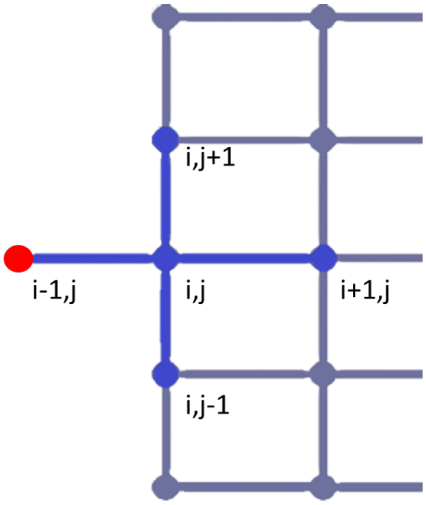

Figure 3.8: FTCS stencil applied to a mesh boundary. Imaginary node: point i-1,j (red) lies outside of the boundary.

At system boundaries, information on certain points of the stencil (Eqn. 3.9d) will appear to be missing as they extend beyond the mesh limits (Fig. 3.8). Through the discretisation of an assumed boundary condition, e.g. a source, sink or constant concentration value, this imaginary point can be replaced [64]. For the RD model, the following initial and boundary conditions were implemented and are illustrated in Fig. 3.9:

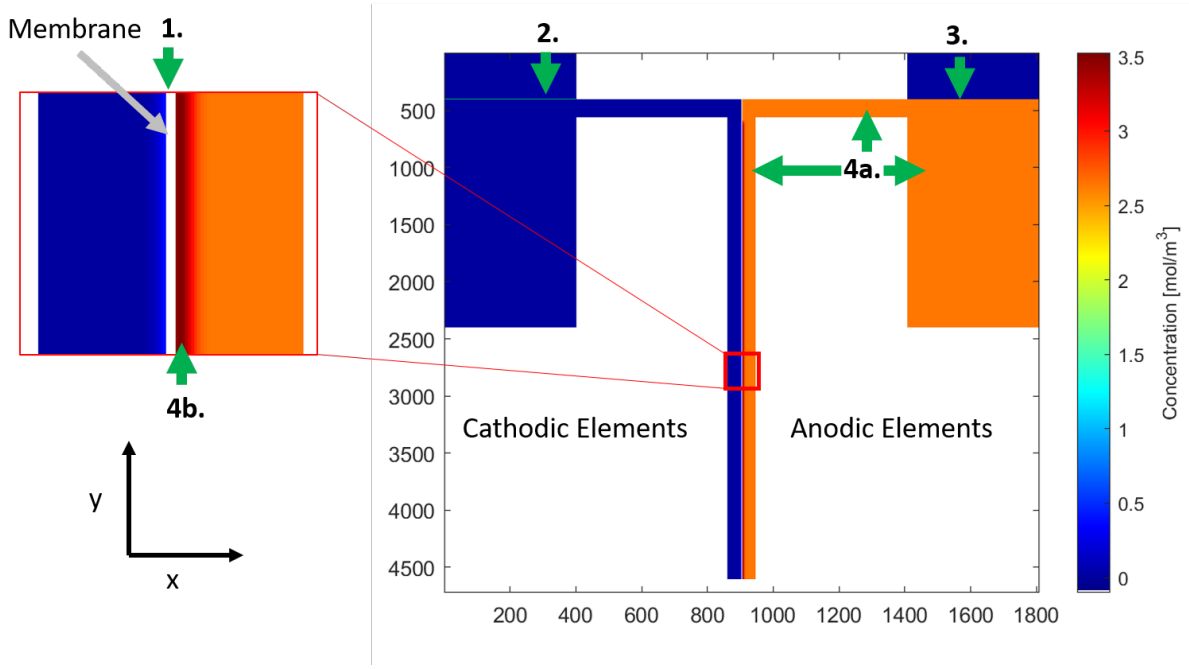

Figure 3.9: Computational domain of AEC components, excluding the H_2 buffer, illustrating the near-instantaneous profile of oxygen crossover concentrations after shutdown. Conditions follow numbering of in-text description.

1. To implement diffusional membrane crossover, a Neumann flux boundary is applied that sets the flux of dissolved species away from the nodes at the membrane boundary equal to the flux across the membrane (see Eqn. 3.12a). Based on previous assumptions, only the x-directional flux is considered here. The relationship describes the transition of the migration of dissolved species from the electrolyte phase at the membrane boundary into the membrane phase within its pores. It is exemplified for oxygen crossover in the anodic chamber (similar to the case depicted in Fig. 3.8) as follows :

$$N_{\mathrm{O}_2,KOH}\Big|_{x=an/mem} = N_{\mathrm{O}_2}^{fick}\Big|_{mem} \tag{3.12a}$$

$$D_{\mathrm{O}_2,\mathrm{KOH}}\frac{c_{i+1,j}^{t} - c_{i-1,j}^{t}}{2\Delta x} = \frac{-D_{\mathrm{O}_2,\mathrm{KOH}}^{mem}}{d_{sep}}(c_{O2,KOH}^{cat/mem} - c_{O2,KOH}^{an/mem}) \tag{3.12b}$$

$$c_{i-1,j}^{t} = \frac{2\Delta x D_{\mathrm{O}_2,\mathrm{KOH}}^{mem}}{D_{\mathrm{O}_2,\mathrm{KOH}} d_{sep}}(c_{O2,KOH}^{cat/mem} - c_{O2,KOH}^{an/mem}) + c_{i+1,j}^{t} \tag{3.12c}$$

where $c_{O2,KOH}^{an/mem} = c_{i,j}^{t}$ and $c_{O2,KOH}^{cat/mem}$ is the corresponding node at the membrane boundary in the cathode that is at the same y-coordinate. A first order centered difference approximation is applied in Eqn. 3.12b to estimate the spatial derivative of Eqn. 3.9a. By explicitly solving for $c_{i-1,j}^{t}$ in Eqn. 3.12c, an expression for the imaginary node can be implemented when applying the stencil to membrane boundary nodes. In this manner, the concentration gradient across the membrane changes over time and links the two half-cells by the concentration values of the nodes on each side of the cell membrane boundary.

2. The electrolyte level, and thus, the gas-liquid interface within the flashtank is assumed to be situated at the height of where the pipe enters. At this boundary, an instantaneous degassing phenomenon is assumed for crossed over species. The FDM stencil is applied to the nodes representing the electrolyte top layer and the dissolved crossover species accumulates. Simultaneously, the adjacent nodes in the gas phase take on this concentration value, i.e. the crossover species degases, and after each time step, the nodes in the liquid phase at this boundary revert back to a value of zero:

$$c(x, y = gas/interface, t = t) = c(x, y = \mathrm{KOH}/interface, t = t) \tag{3.13a}$$

$$c(x, y = \mathrm{KOH}/interface, t = t + 1) = 0 \tag{3.13b}$$

3. Contrary to the previous condition, when the gas-liquid interface in the flashtank acts as a source, i.e. when the stored gas re-dissolves into the electrolyte, a Dirichlet boundary is assumed, whereby the electrolyte top layer takes on the value of the species saturation concentration as predicted by the modified Henry's law, fixed for all time steps t (Appendix A.2):

$$c(x, y = \mathrm{KOH}/interface, t) = c_i^{j,sat} \tag{3.14}$$

where i, j correspondingly represent hydrogen on the cathodic side in the hydrogen flashtank ($i = \mathrm{H}_2, j = cat$) or oxygen on the anodic side in the oxygen flashtank ($i = \mathrm{O}_2, j = an$).

4. (a) At time step t=0, the electrolyte contained within the chamber, pipe and flashtank is assumed to be saturated with dissolved gas species as predicted by the modified Henry's law. (b) Additionally, the nodes at the membrane boundary are assumed to be initially supersaturated, where concentrations have been scaled by a saturation factor (X^{sat}):

$$c(x, y, t = 0) = c_i^{j,sat} \tag{3.15a}$$

$$c(x = j/mem, y, t = 0) = X^{sat} \times c_i^{j,sat} \tag{3.15b}$$

where i, j correspondingly represent hydrogen in the cathodic chamber ($i = \mathrm{H}_2, j = cat$) or oxygen in the anodic chamber ($i = \mathrm{O}_2, j = an$).

5. For all time steps t, a discretised no-flux Neumann boundary is applied to the walls of each component to signify an impermeable boundary where no concentration gradient exists, i.e. the flux equals zero:

$$N_{x,KOH}\Big|_{x=wall,t} = N_{y,KOH}\Big|_{y=wall,t} = 0 \tag{3.16}$$

For a detailed breakdown on how this model was implemented, the reader is referred to Appendix A.2.

3.4. Cantera Simulation Software

In order to perform combustion modelling, the Cantera's Python interface was used (Version 2.4.0), which is an open-source platform that facilitates the computation of thermodynamics, kinetics and transport phenomena, and is widely used in combustion calculations [18, 65].

3.4.1. Mechanistic Input Files

To run Cantera simulations, an input file is required that describes information on thermodynamic, transport and reaction kinetic data of the desired species to model [18]. This is commonly referred to as the chemical mechanism and has been widely developed for the combustion of hydrogen across a wide range of conditions [15–17, 19]. The mechanisms adopted in this thesis are reflected in Table 3.1. Additionally, the hydrogen-oxygen reaction mechanism within Cantera's software library ('h2o2.cti') was applied. This mechanism is based on a GRI-3.0 mechanism where the carbon chemistry has been made redundant and only contains argon gas in addition to the hydrogen-oxygen relevant species [18].

3.4.2. Chemical Equilibrium Calculations

Based on thermodynamic properties, the final flame temperature and its corresponding chemical composition can be calculated. These depend on the initial temperature and pressure as well as the starting fuel-oxidiser gas composition [66]. In combustion systems, inlet compositions are typically expressed through their *equivalence ratio* ϕ. It is defined as (Eqn. 3.17):

$$\phi = \frac{(\frac{x_{fuel}}{x_{ox}})}{\frac{x_{fuel,stoich}}{x_{ox,stoich}})} \tag{3.17}$$

where ϕ is equivalence ratio, x_{fuel} and x_{ox} are the actual fuel and oxidiser mole fractions, respectively, and $x_{fuel,stoich}$ and $x_{ox,stoich}$ are the stoichiometric fuel and oxidiser mole fractions [66].

Table 3.1: Chemical mechanisms applied in this framework, illustrating the range across which they are valid as well as the number of reactions and species they consider.

Mechanism	Validity			Number of Species | Reactions
	P [atm]	T [K]	ϕ	
Li et al.	0.30 - 87.00	298.00 - 3000.00	0.25 - 5.00	13 | 25
Ó Conaire et al.	0.05 - 87.00	298.00 - 2700.00	0.20 - 6.00	10 | 40
Burke et al.	0.30 - 87.00	298.00 - 3000.00	0.25 - 5.00	11 | 26

To characterise the combustion process in this study, adiabatic flame temperatures (AFT) and equilibrium compositions ($x_{i,eq}$) are calculated. This is performed on Cantera by applying the *equilibrate()* function, and is based on a method similar to the Gibbs free energy minimisation method typically applied [18, 66]. Here, the enthalpy and the pressure are fixed as the gas is set to an equilibrium state. The solution procedure is presented in Fig. 3.10:

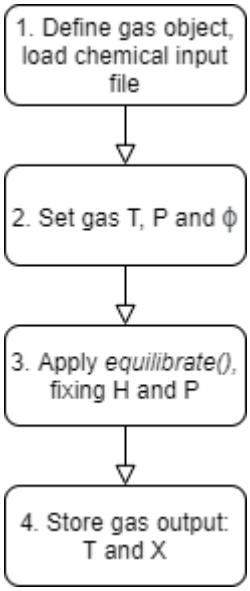

Figure 3.10: Schematic procedure of setting a gas mixture to a chemical equilibrium state in Cantera. *T* - temperature, *H* - enthalpy, *P* - pressure, ϕ - equivalence ratio, *X* - gas mole fraction.

3.4.3. One Dimensional Laminar Premixed Flat Flames

The laminar flame speed is defined as the velocity at which a laminar flame propagates into an inactive mixture of unburnt species and contains information about an igniting mixtures' heat release [66, 67]. Alternatively, the laminar flame speed gives an indication of a flame front's reactivity and diffusivity [19, 66]. Based on the correlation derived from Zeldovich's model of thermal flame propagation, the laminar flame speed is mathematically expressed as [66]:

$$S_l = \sqrt{\frac{\alpha}{\tau_c}} \tag{3.18}$$

where S_l is the laminar flame speed in $\mathrm{m\,s^{-1}}$, α is the diffusivity across the flame front (where mass and thermal diffusivity are assumed to be equal) $\mathrm{m^2\,s^{-1}}$, τ is the characteristic time of reaction in s, equal to the reciprocal of the first-order reaction rate constant $\frac{1}{k}$ that describes a simplified, one-step combustion reaction [66].

To calculate the laminar flame speed in the Cantera environment, the *FreeFlame()* function is applied [18]. Its solution procedure is depicted in Fig. 3.12 It assumes the following:

- A one dimensional, freely-propagating flame is treated.
- Adiabatic conditions.
- The flame front is fixed in a co-ordinate system and the gases move relative to it, illustrated in Fig. 3.11.

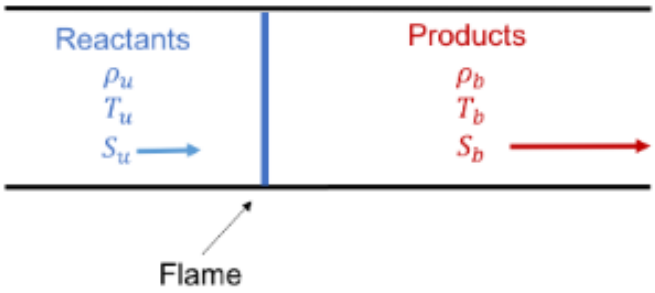

Figure 3.11: Overview of the fixed-flame co-ordinate system applied in the solution of Cantera's *FreeFlame()* function. ρ - density, T - temperature, S - velocity; subscripts: *u* - entering, unburnt mixture, *b* exiting, burnt mixture.

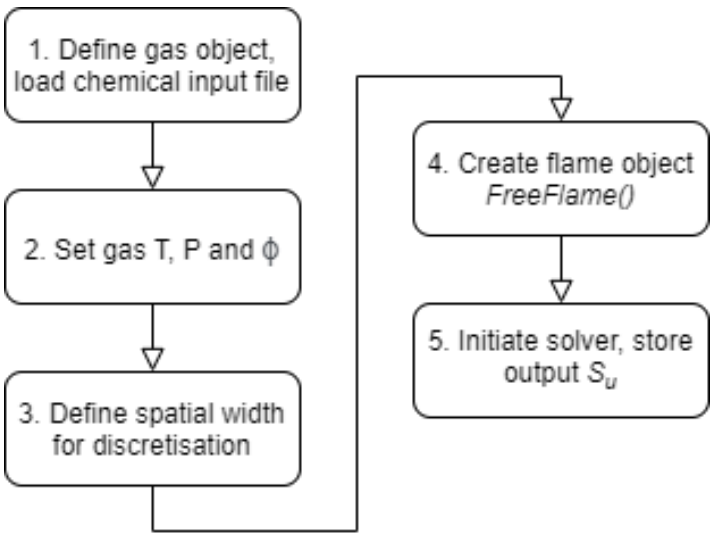

Figure 3.12: Schematic solution procedure in implementing Cantera's *FreeFlame()* function to solve for the laminar flame speed, equivalent to the speed of the unburnt entering mixture *Su*.

4

Results on Prediction of Crossover Accumulation

This chapter presents the outcomes of the developed crossover models that were described in Section 3.3. Section 4.1 goes into the results of the in-operation model, while Section 4.2 presents the results of the reactor downtime model.

4.1. In-Operation Model

For details on mode validation, the reader is referred to Appendix A.1.

4.1.1. Comparison of Crossover Modes

The conditions were set to match ZEF's operational parameters at 50 bar, 80 °C and the use of a standard 463 µm thick Zirfon™ Perl separator [58]. For comparison purposes, the COC (Eqn. 3.7b) was converted to hydrogen mole fractions to illustrate its relation to the UEL tolerance level through:

$$100\% - \left(\frac{N_{O_2}^{cross}}{N_{O_2}^{cross} + N_{H_2}^{cat}} \times 100\%\right) \tag{4.1}$$

Hydrogen crossover due to Fickian diffusion and Darcian permeation is presented in Fig. 4.1. The trends reflected match those determined in literature for both phenomena: decreasing the current density resulted in an increase in the amount of gas impurities. This is due to a decline in oxygen production as the current density decreases. With less product gas to dilute crossed over gas, AHC rises [25, 57]. The reverse is true for oxygen crossover and hydrogen production, but to a smaller degree (Fig. 4.2).

The data shows that crossover due to cross-permeation contributes to higher impurities than diffusional crossover. Analysis shows that by adopting a 1% pressure difference between cathodic and anodic chambers from literature [21], a 50-fold increase in the AHC is predicted between cross-permeation crossover and diffusional crossover. This ratio is maintained between 2.50 and 1.00 A cm^{-2}, but drops as the current density decreases due to a growth in diffusional crossover impurities.

Furthermore, the rate of change of AHC to current density for each mode of mass transport was investigated, graphically indicated by the slope of each curve. The ratio of their rates (cross-permeation to diffusion), that the AHC changes faster for Darcian than it does for Fickian crossover, further highlighting the contrast in the magnitudes of crossover fluxes.

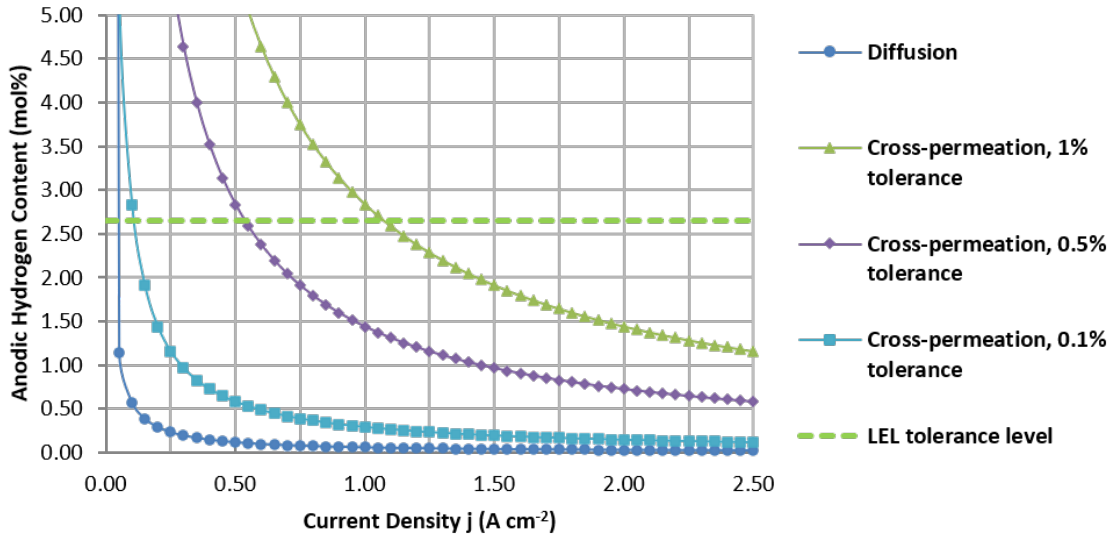

Figure 4.1: Plot of hydrogen crossover, in the form of the anodic hydrogen content (AHC), as a function of current density. LEL tolerance represents 50% of the lower explosion limit as stipulated by Schroeder and Holtappels [14].

Similar observations were made for the oxygen crossover as well (Fig. 4.2): cross-permeation contributes to a larger decrease in gas purity than diffusional crossover, with a roughly 50-fold larger contribution, and its rate of change in gas impurities rises faster than it does for diffusion. Oxygen crossover, however, is lower in absolute terms when compared to the hydrogen crossover, regardless of mass transport mode. This has been documented in literature and can be traced to its larger molecule size, its related smaller diffusion coefficient, as well as due to the difference in stoichiometry between the two evolving gases [12, 21, 24].

4.1.2. Effect of Cell Pressure Difference

General Observations

Additionally, as a further expansion upon Schalenbach et al.'s work [21], varying degrees of pressure difference extents between half-cells were investigated, with the differential pressure ranging from 1% to 0.5% and 0.1% of absolute system pressure. In particular, a focus was set on its effect relative to the LEL and UEL tolerance levels of gas mixtures, which are set at $0.5 \times LEL$ and $UEL + 0.5 \times (100\% - UEL)$, respectively, and are practised safety margins enforced in industry to avoid a flammable mixture.

Generally, a lower pressure imbalance tolerance level leads to a lower amount of gas crossover due to pressure effects. In both cases, maintaining a differential pressure smaller than 0.1% of the absolute system pressure lowers the impurity percentage by a factor of ca. 10, as expected due to the linearity in the relationship.

Impurity Levels Relative to LEL & UEL

Within the context of hydrogen crossover, the largest tolerance level of 1%, which was adapted from Schalenbach et al.'s study, showed that at a current density of 1.05 A cm^{-2}, the amount of impurities predicted is sufficient grounds for a reactor shutdown and purge cycle (Fig. 4.1), as is common practice in industry [24]. By minimising this differential pressure to 0.1%, H_2 crossover levels pose a safety risk when the current density approaches 0.15 A cm^{-2}. In the case of oxygen crossover, dangerous levels of impurities (the UEL tolerance level) are

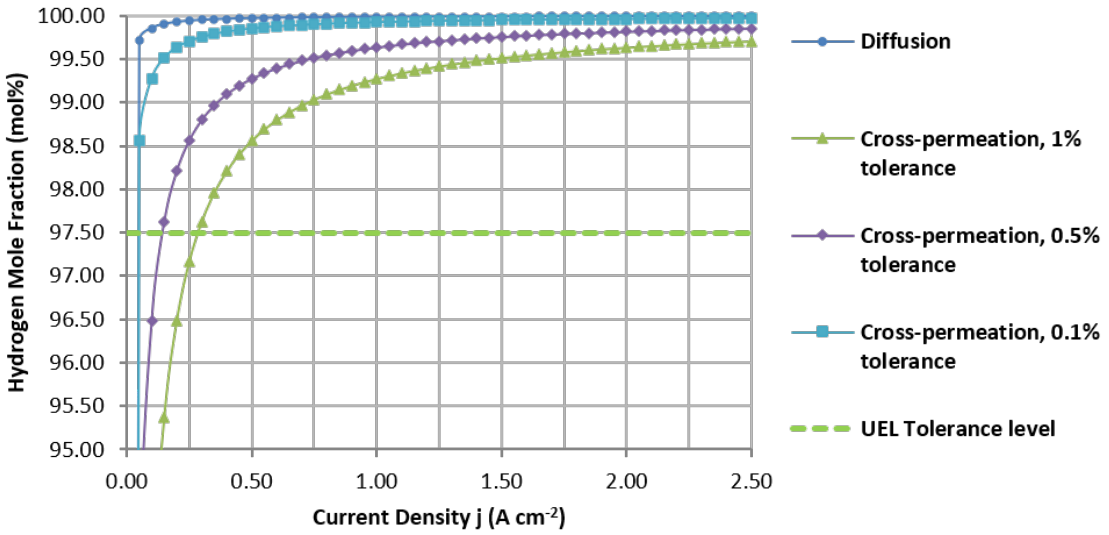

Figure 4.2: Plot of oxygen crossover as a function of current density, expressed as H_2 mole fraction to illustrate concentration values relative to 50% of the UEL or upper explosion limit as stipulated by Schroeder and Holtappels [14].

reached at 0.3 and 0.05 A cm^{-2} for inaccuracy tolerances of 1% and 0.1%, respectively (Fig. 4.2). This highlights that due to the larger spread of dangerous current density values in the AHC, minimising differential pressure across the half-cells has a greater impact on reducing hydrogen crossover than it does for oxygen crossover.

As the deployment of high pressure electrolysis systems gains in appeal for industrial energy storage applications, coupled with the fact that standard industrial systems aim to typically run at current densities of around 1.00 A cm^{-2}, it becomes imperative for more research to be conducted on this matter to characterise large-scale systems and to further validate the extent of this effect.

4.1.3. Implications for ZEF

Preliminary Safety Assessment: Hydrogen Crossover

In the context of ZEF's system, the target current density during operation lies at 0.33 A cm^{-2}, well within the dangerous operating point for hydrogen crossover (Fig. 4.1). However, as the oxygen flash tank is consistently purged during operation (see Subsections 1.2.1, 1.3.1), an accumulation of trace hydrogen to unsafe levels is unlikely. Moving forward within this project though, validating this effect as well as the planned pressure balance control scheme (Section 3.1) will be necessary for proper practical safety assessment.

Preliminary Safety Assessment: Oxygen Crossover

Oxygen crossover, on the other hand, poses a likelier failure point. Though the current density operational window for safe levels is larger in oxygen crossover (Fig. 4.2), ZEF's set point places the AEC operation at risk according to predicted values at a 1% inaccuracy tolerance, and may be put at further risk through dynamic operation, even if the tolerance is halved. In contrast, diffusion only poses a safety hazard at current densities below 0.05 A cm^{-2} and implies that during operation at a wide range of current densities, crossover due to diffusion does not pose a concern for safety.

Comparable levels of safety are also achieved for cross-permeation if the pressure imbal-

ance tolerance level is maintained at 0.1%., with only minor deviations below 0.50 A cm^{-2}. For both cases though, the data underlines the notion that during intermittent periods of less available solar energy output (i.e. temporary bad weather conditions), the AEC must not run at current densities lower than say 0.05 A cm^{-2} as the behaviour of the impurity content tends to 100% as the current density becomes smaller than this value.

Model Outcome

Simply turning off the AEC may stop the supersaturation condition (Subsection 3.2.2), but saturation concentrations will continue to drive crossover by diffusion. Furthermore, with no current running, gas production may be halted, but a pressure imbalance will still exist unless addressed, sustaining crossover due to permeation. Therefore, it can be conclusively drawn that, regardless of the pressure inaccuracy tolerance level assumed, a need arises to address both pressure balancing within the AEC and oxygen impurity removal for low current regimes and during shutdown procedures, highlighting the hydrogen buffer as a likely failure point.

Further system characterisation and validation of this phenomenon is recommended. Additionally, understanding how pressure effects diminish within the cell after shutdown and at what time-scales will be important in devising appropriate control schemes. This may also aid in understanding when the gas scavenger (Subsection 1.3.3) should be launched, answering questions about its operation frequency and duration.

4.2. Reactor Downtime Model

In line with the defined scope and the objectives of this thesis as stipulated in subsection 1.3.1, the following subsections are discussed in the context of oxygen crossover within the AEC. The reader is referred to Appendix A.2 for data and a brief overview on hydrogen crossover. Furthermore, for details on model verification, the reader is referred to Appendix A.2

4.2.1. RD Model Initialisation

Parameter Summary and Mesh Definition

The build-up of trace oxygen has been modeled for the case of a single electrolytic cell system analogous to ZEF's AEC. Concentration distribution profiles were observed at each hourly interval, in addition to the 30-second-mark and 30-minute-mark profiles. Furthermore, data on oxygen flux and total crossover moles accumulated were collected at each interval. A uniform mesh was generated based on the following information (Tables 4.1 & 4.2).

Table 4.1: Part 1: Summary of system and computational mesh parameters implemented in RD model crossover analysis of AEC components.

Parameter	Description	Value	Unit
Δx	Spatial step size, x-direction	5.00×10^{-5}	m
Δy	Spatial step size, y-direction	5.00×10^{-5}	m
Δt	Temporal step size	3.60×10^{-1}	s
P_{sys}	System pressure	50.00	bar
T_{sys}	System temperature	80.00	°C
w_{KOH}	Mass percent of KOH in electrolyte	32.00	%

Table 4.2: Part 2: Summary of system and computational mesh parameters implemented in RD model crossover analysis of AEC components.

Parameter	Description	Value	Unit
$c^{an}_{O_2,sat}$	Saturated concentration of O_2 [12]	2.63	mol/m^3
$c^{an}_{O_2,supersat}$	Supersaturated concentration of O_2 [25]	13.15	mol/m^3
$D_{O_2,KOH}$	Diffusion coefficient of O_2 in KOH [12, 24]	1.71×10^{-9}	m^2 s^{-1}
d_{sep}	Separator thickness [12, 57, 58]	$(4.63 \pm 0.50) \times 10^{-6}$	m
ϵ	Separator porosity [12, 25]	0.50	-
τ	Separator tortuosity [12, 25]	3.14	-

Implications of Membrane Boundary Assumption

By applying the Neumann boundary (Subsection 3.3.3) to describe membrane crossover, a flux was not imposed, but rather defined by the concentration gradient across the membrane that changes over time and depends on the the concentration values of the nodes on each side of the cell membrane boundary, linking the two half-cells.

To implement this boundary condition, it was assumed that due to the membrane thickness, there are no strong, parallel forces within the membrane. Hence, the flux across the membrane was assumed to be solely dependent on the x-component as the y-component was negligibly small. This means the model effectively pieces together a 2D + 1D + 2D domain when moving across the electrolytic cell. Therefore, flux is conserved across the chambers in two dimensions and across the membrane in one dimension.

4.2.2. Observations in Crossover Concentration Profiles

Immediately After Shutdown

The initial oxygen diffusion process is localised to the anodic membrane boundary. Here, the difference in concentrations between the two chambers drives the transport of oxygen across the membrane and into the cathodic chamber. Additionally, due to the supersaturation condition in the vicinity of the membrane, a concentration gradient is also established across the anodic chamber that forces oxygen from membrane boundary to bulk anolyte. Both phenomenon are depicted in Fig. 4.3.

Furthermore, the simulation results show that 30 seconds after shutdown, the supersaturation concentration spike has already been reduced by more than 70%, from 13.15 to 3.50 mol m^{-3}. In this time frame, diffusion is not observed in any other component. This is because the anolyte in the flash tank, the pipe and the majority of the anodic chamber is initially saturated with dissolved oxygen at the same concentration. Without a gradient present, diffusion does not take place.

One Hour After Shutdown

Through the continued diffusional spread, the initial concentration spike caused by the supersaturation condition has completely diminished after one hour, with no local, residual concentration maximum observed in the anodic chamber. The concentration is shown to decrease in the negative x-direction when moving from anodic to cathodic chamber wall and signifies that diffusion is predominantly taking place across the width of each chamber (Fig. 4.4). This gradient continues to drive crossover and oxygen continues to gradually penetrate further into

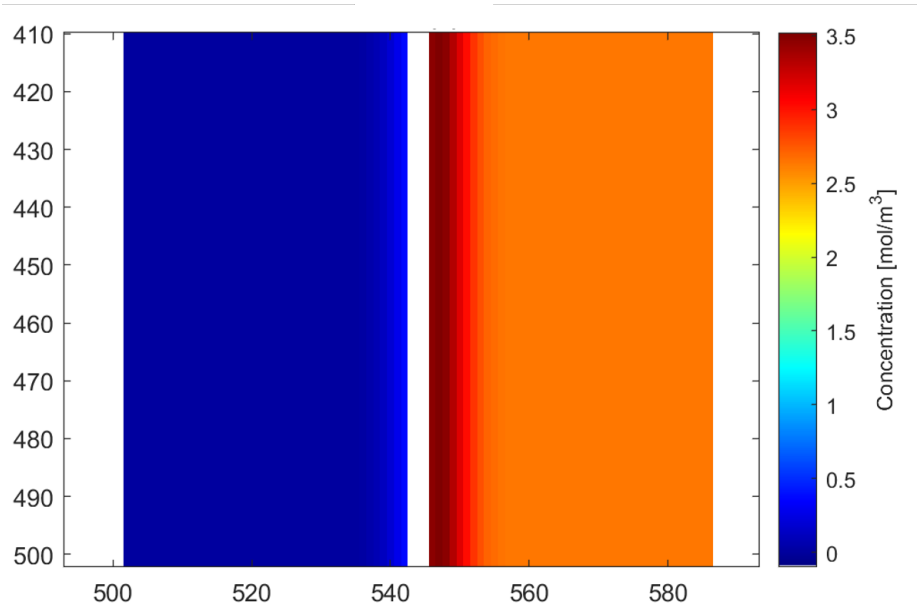

Figure 4.3: Oxygen concentration distribution 30 seconds after shutdown in the AEC cathodic (left) and anodic (right) chambers. X- and y-axes show the relative positions in the coordinates of the computational domain.

the anodic chamber as time passes. Furthermore, initial diffusional effects are observed in each respective channel at the top of the chamber.

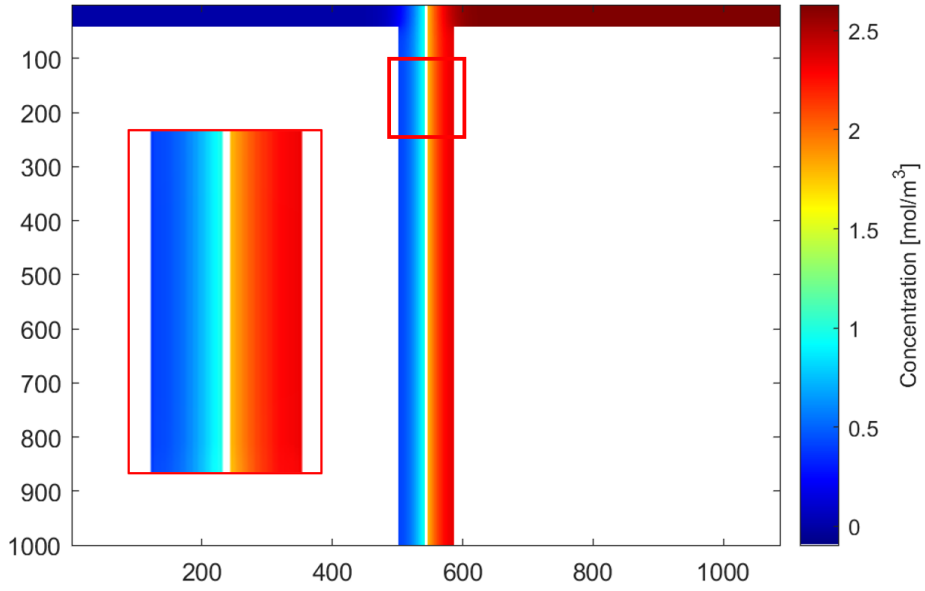

Figure 4.4: Oxygen concentration distribution 1 hour after shutdown in the AEC cathodic (left) and anodic (right) chambers and connecting pipes.

Eight Hours After Shutdown

After eight hours, an equilibrium between each half-cell is achieved as illustrated in Fig. 4.5. Concentrations are equal in each chamber and as a result, there is no gradient to further drive crossover, reducing the flux to zero. Diffusion is still present at each chamber outlet

with indications of diffusive mixing present in the y-direction. The extent of the spread in the channel has also clearly progressed from initial observations at the one hour mark. The penetration of oxygen into the channel leading to the hydrogen storage tank is mirrored by the depletion of oxygen in the channel leading to the oxygen flash tank.

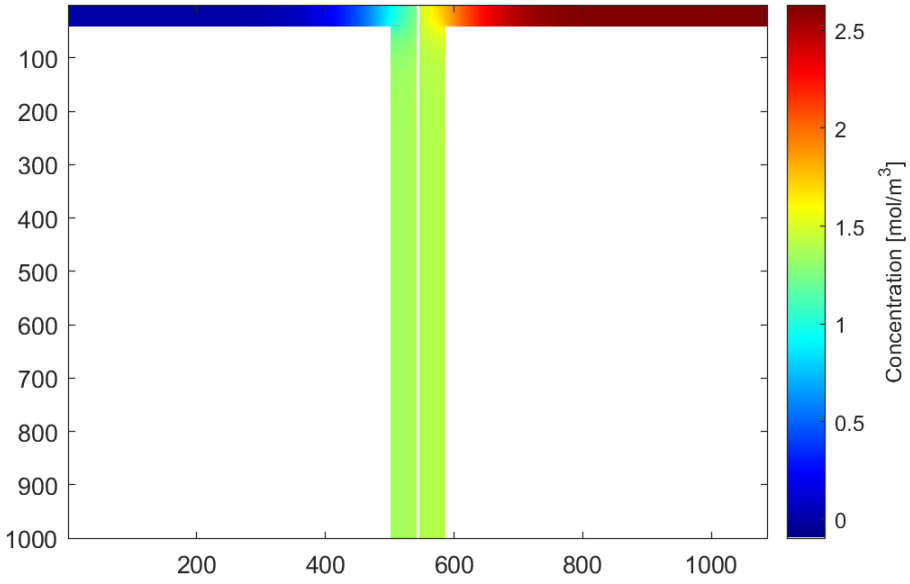

Figure 4.5: Oxygen concentration distribution 8 hour after shutdown in the AEC cathodic (left), anodic (right) chambers and connecting pipes.

4.2.3. Concentration Profile Analysis

Fourier Number for Mass Transfer

Similar to the non-dimensionalisation of the unsteady-state diffusion solution in a semi-infinite slab or plate, the initial diffusion process within the AEC can be characterised by a non-dimensional time parameter, upon which the dimensionless concentration development depends. This dimensionless time is commonly referred to as the Fourier number in both heat and mass transfer, and generally simplifies the solution analysis [68]. It is defined in this system specifically as [69]:

$$Fo_M = \frac{D_{O_2,\mathrm{KOH}} \times t}{(L)^2} \tag{4.2}$$

where Fo_M is the dimensionless Fourier number for mass transfer, $D_{O_2,\mathrm{KOH}}$ is the diffusion coefficient of oxygen in KOH given in $m^2\,s^{-1}$, t represents the characteristic time observed in the system given in s, and L is the length across which diffusion is studied given in m. The Fourier number can be understood as a measure of the system's ability to diffusive a species over a specified distance, i.e. whether enough time has been observed for significant diffusion to have occurred. Therefore, based on its magnitude, a statement can be made about the system's limiting behaviour [68].

Chamber Diffusion Phases

To characterise the system, horizontal cross-section concentration profiles of the two chambers were analysed and serve as the foundation for the following discussion (Fig. 4.6).

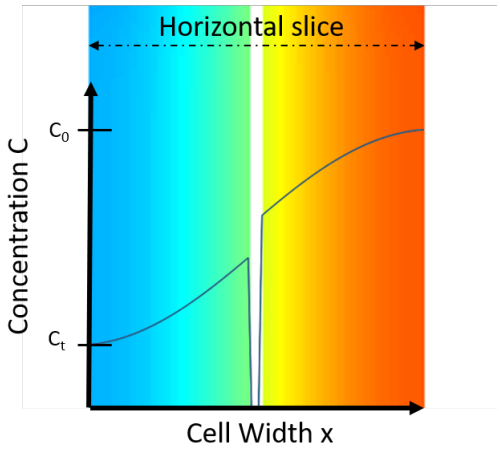

Figure 4.6: An overlay of a concentration versus chamber position plot onto a concentration distribution profile. The plot corresponds to a horizontal slice of the cell, where C_0 and C_t represent the initial concentration and concentration at time t, respectively.

In the initial phase, the AEC is characterised by a low Fourier number (10^{-1} to 10^{-2}) and thus, behaves similarly to the case of a semi-infinite plate (Fig. 4.7). Oxygen crosses over and penetrates into the cathodic chamber, propagating freely or unbounded as if the chamber were infinitely thick. The concentration across the anodic chamber remains largely unaffected (particularly close to the anodic wall), but experiences a flux of oxygen from membrane boundary to bulk anolyte, indicated by the local maximum at $t = 30$s as the pulse of the supersaturation concentration decays.

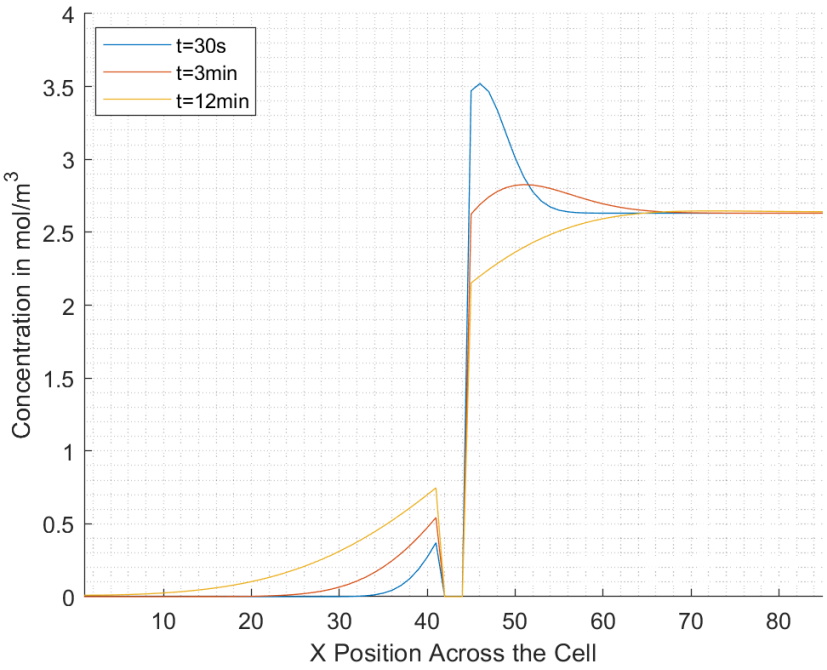

Figure 4.7: Horizontal cross-sectional concentration profile at the middle of the cell immediately after shutdown. The gap between the vertical lines represents the position of the membrane.

As time progresses, oxygen penetrates further into the cathodic chamber and the Fourier number grows. However, at a certain point in time, a transition occurs caused by the effects of the cathodic chamber wall. With the diffusional spread limited by the wall, oxygen begins to accumulate in the cathodic chamber. Additionally, unlike in the case of a semi-infinite plate where a constant source of species is assumed, the concentration at the anodic wall begins to decrease through continued depletion as reflected at $t = 1$h in Fig. 4.8. Both factors reduce the gradient across the membrane and the flux begins to slow down. In this final phase, the system is no longer characterised by the Fourier number. This process continues until an equilibrium is established between the two cells at $t = 8$h (Figs. 4.5 & 4.8).

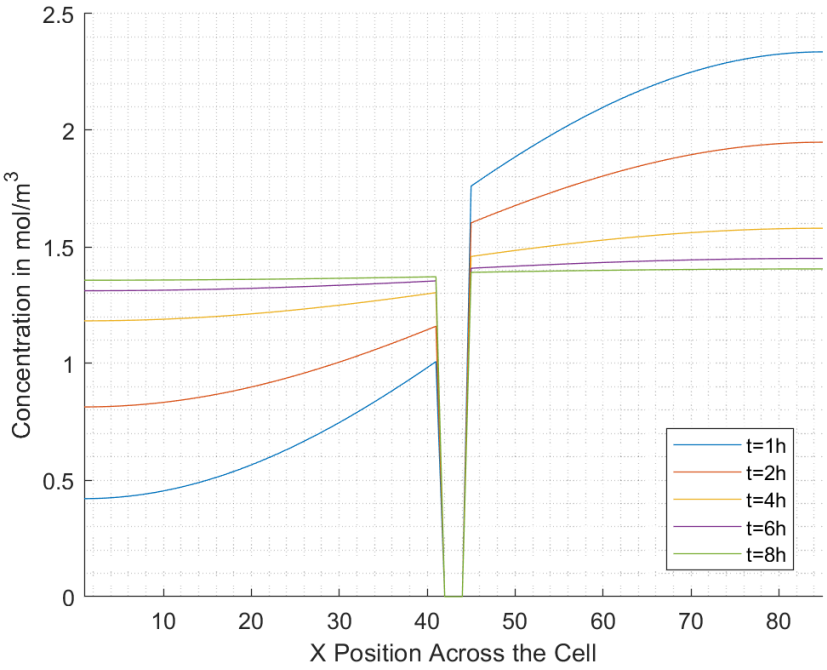

Figure 4.8: Horizontal cross-sectional concentration profile at the middle of the cell after shutdown.

Diffusion Effects Near Chamber Outlet

This transition to the latter stage is not detected to the same degree for diffusion near the top of the chamber. A higher Fourier number ($> 10^0$) characterises the top portion of the system as the effects of the opposing wall (i.e. the cathodic chamber wall) are not experienced and oxygen diffuses into the channel towards the H_2 storage tank. This effect propagates to the surrounding nodes in the vicinity of the chamber outlet through y-directional diffusion. Lower cathodic wall concentrations are, therefore, recorded over time near the top of the half-cell.

As a result, a transition to steady state is observed, where the concentration profile across the chambers resembles that of a general limiting diffusion case across a thin membrane (10^1) [68]. As Fig. 4.9 shows, the profile after $t = 2$h becomes progressively linear and has not reached equilibrium at $t = 8$h . The maintenance of this steady state diffusion relies on the replenishment of *fresh* O_2 from within the channel that leads to the O_2 flash tank to the membrane boundary zone. As the cross-sectional area of the channels is much smaller than that of the MEA, the amount of O_2 transported is reduced. The outlet, therefore, represents a bottleneck to diffusion of O_2 to the H_2 storage tank. The bottleneck is reinforced by the y-directional mixing from chamber to channel, thereby reducing the gradient across the membrane.

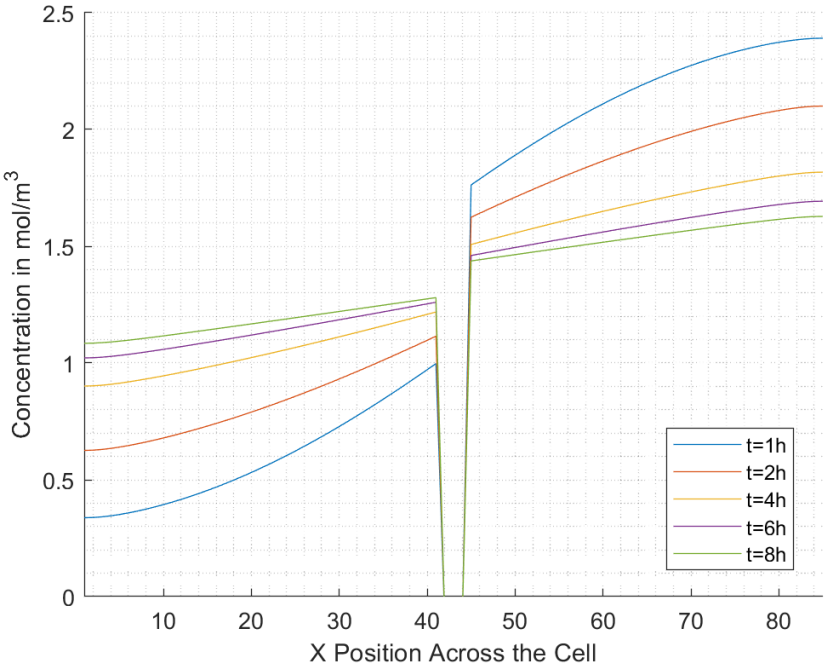

Figure 4.9: Horizontal cross-sectional concentration profile close to the top of the cell after shutdown.

Effect of Crossover Boundary

As a result of the membrane boundary assumption, oxygen is transferred from the anodic chamber at the same rate across the total height of the membrane, which forms a homogeneous concentration layer at the cathodic membrane boundary and is observed to uniformly spread across the chamber over time. This is because the layer acts as an effective array source of oxygen and establishes a stronger gradient or driving force in the x-direction rather than the y-direction.

After close to an hour and a half after shutdown, concentrations examined at equal distances from the membrane in the cathodic chamber showed the same concentration value of 0.865 mol m^{-3} (Fig. 4.10). However, examination of concentrations at the same distance from the membrane closer to the chamber outlet at the top of the cell shows a lower value of 0.762 mol m^{-3}. This is a result of the aforementioned diffusion effects where due to the absence of the opposing wall, the oxygen diffuses further and the concentration diminishes because of the effective dilution.

4.2.4. Effect of Cell Width on Crossover

The effect of the cell geometry, specifically the width of the each half-cell's chamber, has to be investigated under the same conditions as a variable in the effect on crossover accumulation. From its original 4 mm width, the half-cell chambers were (equally) changed to 2 mm, 8 mm, 10 mm and 12 mm. The spatial discretisation in the x-direction was adjusted appropriately to maintain a resolution of $\Delta x = 0.05$ mm (Appendix A). Furthermore, data was analysed over an eight-hour shutdown period as concentration profile studies had previously shown the eight-hour mark to be the point at which crossover had reached a zero flux value. Data on the oxygen crossover flux across the membrane and the total amount of oxygen accumulation were collected at aforementioned time intervals. Results are depicted in Fig. 4.11 and Fig. 4.12, respectively.

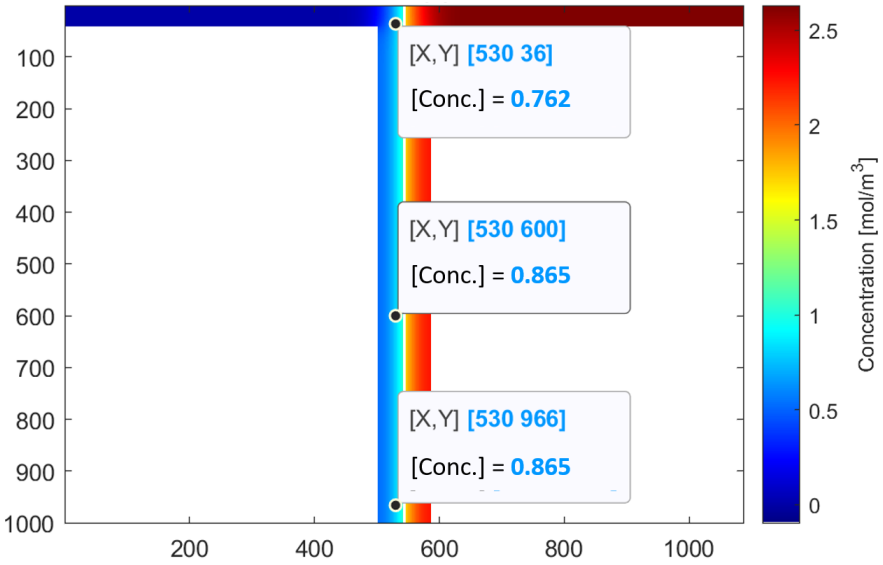

Figure 4.10: Concentration values of three distinct points are illustrated at equivalent widths, but varying heights of the chamber 1.25 hours after shutdown.

Trends in Oxygen Flux Observations

The model data in Fig. 4.11 shows that each cell reaches a common maximum flux point 30s after shutdown of about 1.41 µmol m^{-2} s. As time passes, each flux is observed to decrease from this maximum, and diminishes at different rates: the trend observed reflects that the smaller the chamber, the faster the flux diminishes. This is most evident for the two relatively smaller chambers, whose trends show a clear divergence after 30 minutes and one hour for the 2 and 4 mm wide chambers, respectively.

For larger chamber widths, the difference is not as distinct and branches out more gradually after the four to five hour mark. Furthermore, after eight hours, the flux in the larger chambers persists, exhibiting values between 0.12 and 0.19 µmol m^{-2} s, while for the smaller chambers, the flux has reduced or tends to zero, having reached negligibly small flux values after three and seven hours in the 2 and 4 mm wide chambers, respectively.

Trends in Total O_2 Crossover Accumulation

The data illustrated in Fig. 4.12 pertains to the total molar amount of oxygen that has crossed over at varying half-cell widths as a function of the shutdown time. The trend shows that total oxygen crossover accumulation after eight hours increases with increasing cell width. The rate of change of moles accumulated mirrors the rate of change observed in the oxygen flux results: accumulation development is initially equivalent across all widths until a clear divergence is observed at the 30 minute and one hour mark for a chamber width of 2 and 4 mm, respectively.

With a decrease in the flux after these points in time, oxygen crossover accumulates more slowly, as indicated by the decrease in the slope of each data set. For 2 mm wide chambers, accumulation appears to plateau at 21 µmol, while for 4 mm wide chambers ca. 1.9 times as much oxygen is accumulated after eight hours at 40 µmol, with its slope tending towards zero. The discrepancy for the larger chamber widths is once again less noticeable. Though the slopes of data sets for 8, 10 and 12 mm decrease after the two hour mark, a near-linear trend is observed for oxygen accumulation up until eight hours after AEC shutdown. Furthermore, the final moles accumulated for these larger widths are comparable and range from 60 to 65 µmol.

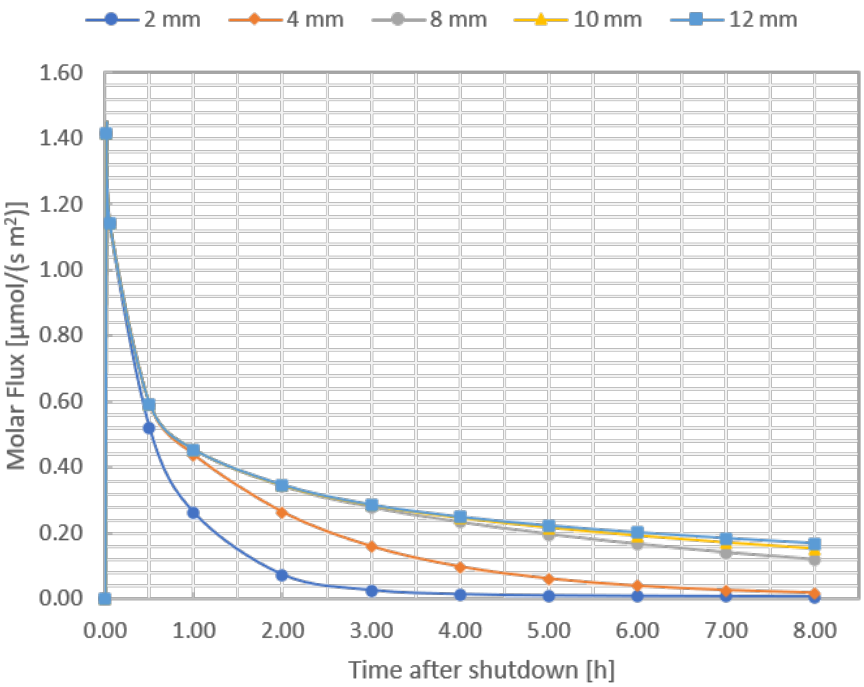

Figure 4.11: Average molar flux of oxygen across the membrane as a function of shutdown time and half-cell chamber width.

Outcome of Oxygen Crossover Data

Under the assumption that no amount of crossover gas exists in the cathodic cell upon shutdown, the maximum obtainable concentration difference is immediately established between the half-cells, and therefore, the largest driving force. This is determined both by the supersaturation condition and the adjacent saturated electrolyte conditions. Regardless of chamber width, this initial condition remains the same and is observed as the maximum flux value after 30 seconds. Through the simultaneous accumulation and depletion within the cathodic and anodic half-cells, respectively, the concentration gradient across the membrane diminishes over time, as demonstrated in the concentration profile analysis. The reduction in molar membrane flux as time progresses follows this reduction in the concentration gradient (Fig. 4.11).

Differences Between Cell Widths

The immediate diffusion process after shutdown occurs mainly at the membrane boundary. As this is the starting point for each cell width, the initial flux and crossover accumulation remain the same in each case as illustrated by the initial trends in Figs. 4.11 and 4.12, respectively. As time progresses, a noticeable change is observed in the slope of the plots at the half hour mark in Fig. 4.11. It indicates the change from the initial phase where oxygen diffuses freely as if in a semi-infinite medium to a transition diffusion behaviour where the influence of the opposing wall in the cathodic chamber begins to take effect.

For the smaller chamber widths, the gradient of the concentration profile is reduced, the flux diminishes to a value of zero, and the accumulation due to crossover slows down and begins to plateau (Fig. 4.12). This effect sets in almost instantly in the case of the 2 mm chamber, but appears more gradual in the case of the mm chamber. The larger chambers, in contrast, show minor susceptibility to these effects in eight hours. Relative to their sizes, more time is needed before the effects of the opposing wall are felt and decrease the concentration

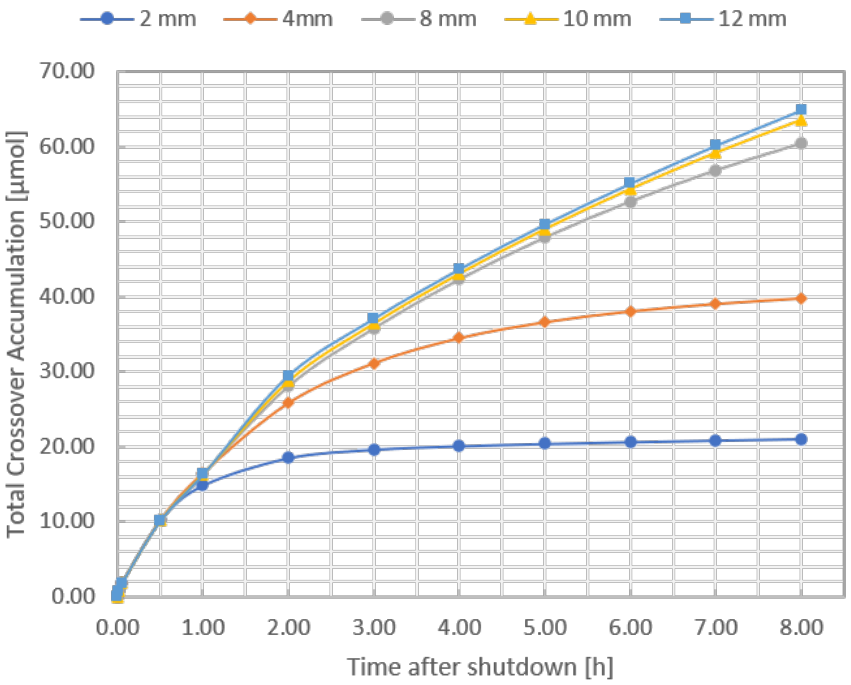

Figure 4.12: Total oxygen crossover accumulation as a function of shutdown time and half-cell chamber width.

at the anodic chamber wall.

Apparent Critical Width

Crossover data suggests the existence of a critical width as shown by the small differences between the data sets for 8, 10 and 12 mm wide chambers. Beyond 8 mm, no substantial increase in the molar flux or accumulation is observed when compared to the surge in crossover accumulation noted in changing the chamber width from 4 to 8 mm (Fig. 4.12). However, were these data sets to be extrapolated to longer shutdown times, more distinct separation between these larger chamber widths would be expected, with the largest chamber (12 mm) demonstrating the longest sustained flux and most moles accumulated. Therefore, the notion of a critical width is false.

4.2.5. Evaluation of Crossover Levels

Extent of Contamination

It has been demonstrated that after an eight hour shutdown period of the AEC, oxygen crossover does not reach the hydrogen buffer or the hydrogen flash tank. This also holds true after a 12 hour shutdown period. The model shows that crossover is mainly effected by the conditions between the half-cells as opposed to any phenomena that occurs in the flash tanks, e.g. oxygen gas re-dissolving into the electrolyte, and that diffusion from the chamber through the pipes represents a bottleneck for oxygen contamination.

Preliminarily, it can be concluded that the AEC is safe during down periods. However, the electrolyte in adjacent cathodic chambers remains saturated with dissolved oxygen after this down period. Upon startup of the AEC, convective mixing through the formation of bubbles is re-introduced into the system, which can promote this oxygen content to be transported and degas, thereby contaminating the hydrogen buffer.

Potential Impact on Buffer Hydrogen Purity

To estimate to what extent this effect poses a safety hazard upon startup, the crossover gas after eight hours for a single was assumed to completely degas. This amount was also scaled to match the amount of cells in the AEC by multiplying the single cell concentration amounts by 20. Crossover contamination may not scale linearly as assumed, especially as certain cells may be more or less influenced by chamber outlets that are in close proximity to the flash tanks, but this estimate provides a worst-case scenario based on crossover modelling data. The results are listed below in Table 4.3.

Table 4.3: Oxygen crossover contamination levels in the hydrogen buffer, shown in mole percent. Values reflect expected crossover levels after eight hours for each chamber width in cases for single cell predictions and ZEF equivalent stack predictions.

Chamber Width	**Buffer Hydrogen Purity**	
	Single Cell	ZEF Stack
[mm]	[mol%]	
2.00	99.998	99.958
4.00	99.996	99.921
8.00	99.994	99.880
10.00	99.994	99.874
12.00	99.994	99.871

Safety Hazard of Crossover Levels

For the case of ZEF's current design, a 4 mm wide chamber causes a negligibly small contamination through crossover for both single cell and full AEC stack solutions. The same can be concluded in the case of a 12 mm wide chamber, in which the impurity level is the highest, yet remains more than a factor of 35 times smaller than the upper explosion limit of hydrogen-oxygen mixtures at the given conditions [14]. Fundamentally, this means that based on the estimates provided in this crossover model, trace oxygen contamination that accumulates due to overnight crossover does not pose a severe safety hazard to the integrity and operation of the AEC.

ZEF Scavenger Necessity

Given the fluctuating conditions of the micro-plant though, the deployment of a gas scavenger within ZEF's system remains necessary. Depending on the daily rate of hydrogen consumption of the MS reactor, an accumulation of trace oxygen within the buffer to dangerous levels can still be feasible on a monthly timescale.

Assuming impurity increases 0.079% (4 mm results, Table 4.3) in the buffer after each night and half of this trace oxygen is consumed in the MS reactor during operation, after about two months the upper explosion limit tolerance level as stipulated by industry shutdown protocols is reached [24]. While generous assumptions were made, this estimate highlights the dangers of a prolonged and unanticipated oxygen accumulation as well as the need for a fail-safe in an autonomous system such as ZEF's micro-plant.

Furthermore, as discussed in the results under in-operation conditions (Section 4.1.3), the dynamic behaviour of the AEC can lead to further accumulation of oxygen, particularly

at lower current densities. Therefore, a low to moderate safety risk cannot be strictly ruled out and encourages the development of appropriate safety schemes to address flammability contingencies through the use of a gas scavenger. Overall, the preliminary results of crossover modelling, indicate that the gas scavenger should be operated upon start-up and shutdown of the AEC as well as at low current density or stand-by conditions, e.g. bad weather conditions.

Local Accumulation Analysis

The possibility of local accumulation zones within the flash tank and buffer has to be investigated to avoid the formation of hotspots that may lead to thermal runaway. Using the output of the FDM model implemented in the main AEC components, initial concentration conditions were specified and represented in two forms: (a) as a point source, representing an immediate degassing process of oxygen located at the pipe inlet of the flash tank (Fig. 4.13); (b) as an array source, analogous to a saturated electrolyte that degases at the gas-liquid interface within the flash tank.

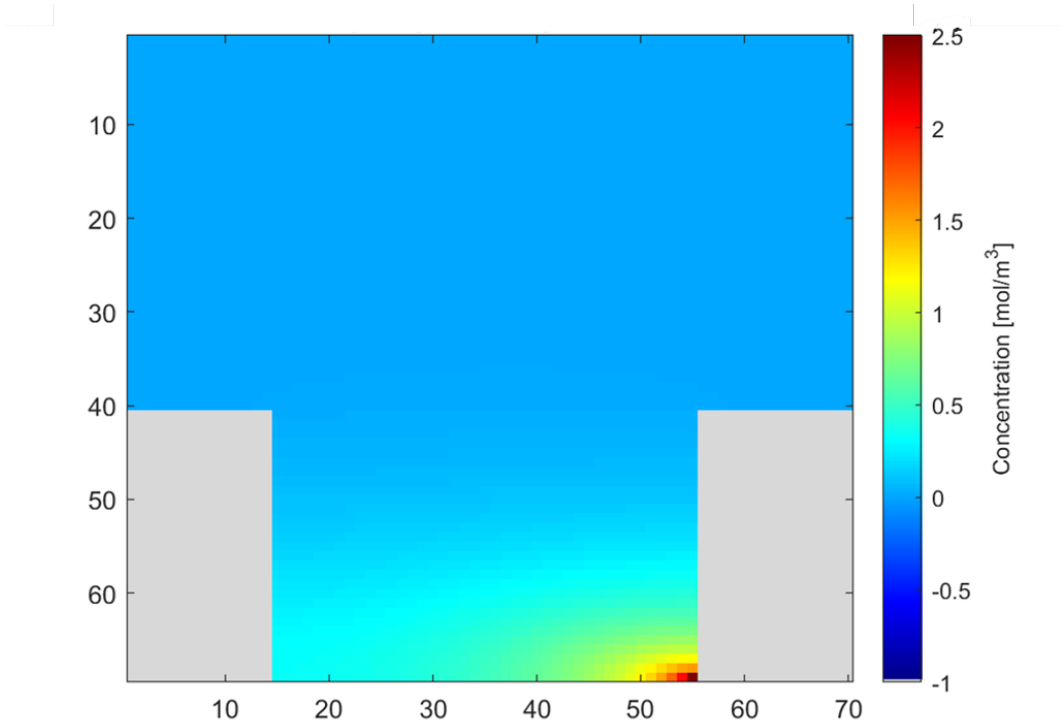

Figure 4.13: Gaseous oxygen concentration profile within the hydrogen buffer and upper portion of the hydrogen flash tank six minutes after initiation.

To simplify the analysis, the hydrogen buffer and flash tank are assumed to be directly integrated in the computational domain as shown in Fig. 4.13 (compare to Fig. 3.3). To implement FDM, discretisation was based on the dimensions and quantities listed in Table 4.4.

Outcome of Oxygen Contamination

The point source contamination was modeled as a continuous presence of a small domain with a concentration of 2.5 mol m^3 that was localised to a single node. At this node, the oxygen is assumed to degas from the liquid electrolyte, and was chosen to represent a worst-case scenario. It was demonstrated that six hours after the introduction of the contaminant to the storage elements, a near-homogeneous mixture was observed as depicted in Fig. 4.14.

Table 4.4: Dimensions and quantities used in the FDM-based analysis of the hydrogen buffer.

Parameter	Description	Value	Unit
Δx	Spatial step size, x-direction	1.00×10^{-4}	m
Δy	Spatial step size, y-direction	1.00×10^{-4}	m
Δt	Temporal step size	1.20×10^{-3}	s
D_{O_2,H_2}	Binary diffusion coefficient (Hirschfelder) [69]	2.16×10^{-6}	$m\,s^{-2}$

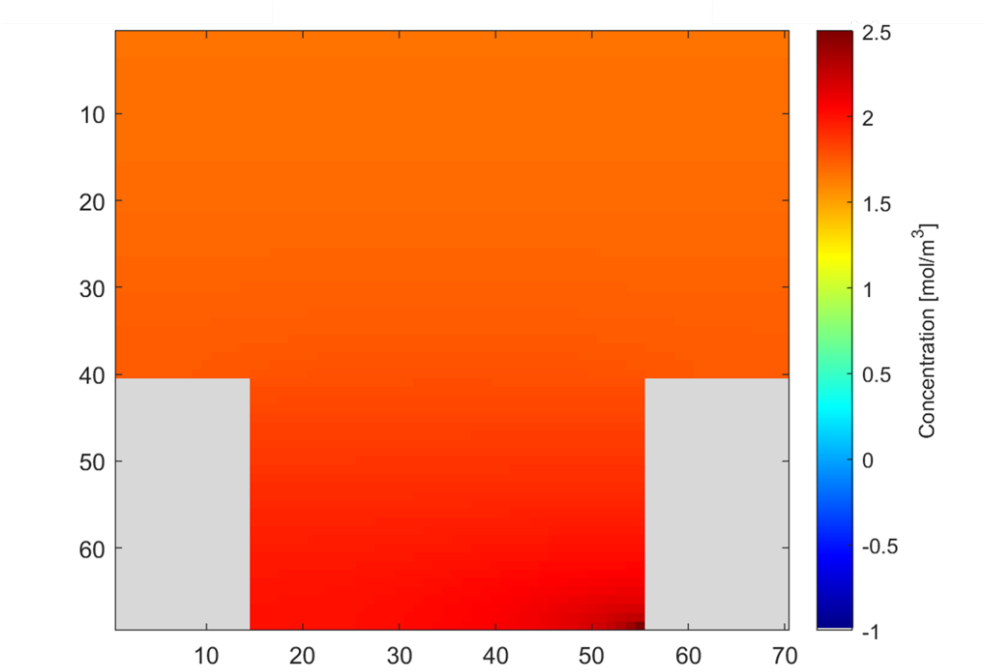

Figure 4.14: Gaseous oxygen concentration profile within the hydrogen buffer and upper portion of the hydrogen flash tank six hours after initiation.

The results indicate that based on diffusive effects, there is complete mixing of trace oxygen contaminants within the stored hydrogen gas. Even at concentrations of 0.5 $mol\,m^{-3}$ for both point and array source cases, (near-) homogeneity was observed after five and three hours, respectively. This means, regardless of initial concentration, due to oxygen's large diffusion coefficient, no local accumulation zones are formed. Convective effects are predicted to expedite this mixing process and shorten the time after which a homogeneous mixture is reached.

Gas Scavenger Placement

The data further implies that a gas scavenger should be implemented between, but ex-situ to the flash tank and the buffer in order to manageably prevent crossover contamination (Fig. 4.15). In this manner, electrolyte-product-gas separation is not impeded, crossover does not homogenise within the buffer and the gas can be channeled through the micro-scavenger device, thereby tailoring it to process smaller volumes and reducing the deflagration risk within the buffer itself.

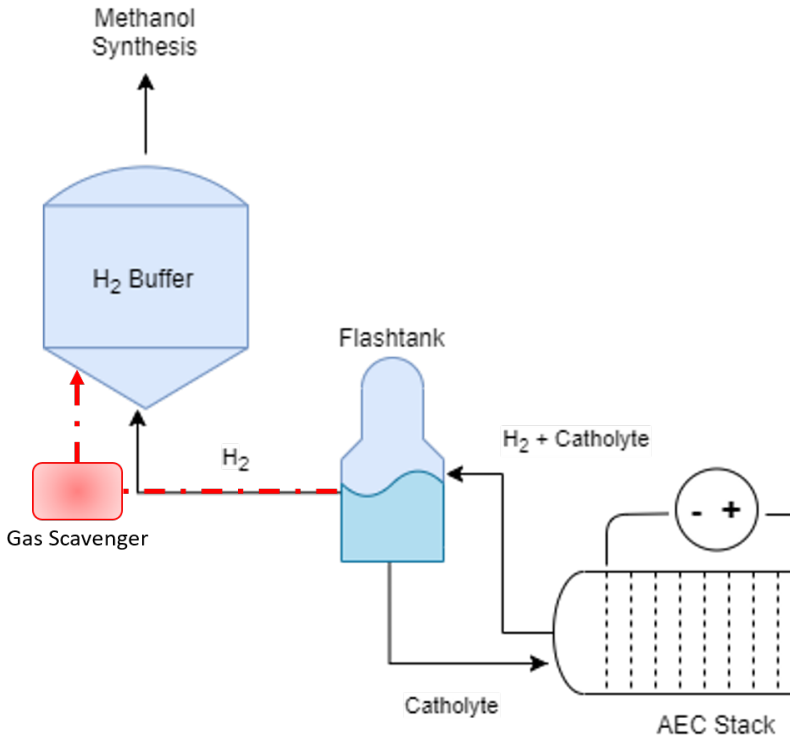

Figure 4.15: Current process scheme of the hydrogen auxiliary components in the AEC with the proposed location at which the gas scavenger should be placed (red). Hydrogen would

The Impact of Component Sizing in the AEC

Finally, the relative sizing of the the stack, the buffer, the cell width and its related crossover predictions has to be investigated for its impact on gas purity levels. The investigation was driven by the idea that the cell width could be an important design parameter in limiting crossover, and that the purity could be predicted by normalising cell crossover effects and stack volume to the buffer volume. Starting from the definition for mole percent and applying the ideal gas law, the following correlation was established:

$$x_{\mathrm{H_2},buffer} = ([\frac{c_{cross,\mathrm{O_2}}\, V_{stack}^{eff}}{V_{buffer}} \times R \times \frac{T_{sys}}{P_{sys}}] + 1)^{-1} \times 100\% \tag{4.3}$$

where $x_{\mathrm{H_2},buffer}$ is the predicted hydrogen purity in the buffer given in %, V_{buffer} is the volume of the buffer given in m^3, R is the universal gas constant at 8.314 $J\,mol^{-1}\,K^{-1}$, T_{sys} is the system temperature in K, and P_{sys} is the system pressure in Pa. In order to obtain Eqn. 4.3, two further quantities have been correlated in this study, which together define the total amount of moles predicted to accumulate due to crossover:

- $c_{cross,\mathrm{O_2}}$ represents the crossover concentration in $mol\,m^{-3}$, i.e. the amount of moles that have crossed over and accumulated normalised to the volume of the chamber: $c_{cross,\mathrm{O_2}} = \frac{n_{cross,\mathrm{O2}}}{V_{cham}}$. Within the framework of this study, eight hour values were used (Table 4.5). This definition was implemented to explicitly add the dimensionality of width to the crossover data.

Table 4.5: Crossover concentrations as a function of chamber width. Data is based on eight hour overnight crossover simulations.

Chamber Width [mm]	Crossover Concentration [mol/m^3]
2.00	1.58
4.00	1.50
8.00	1.14
10.00	0.96
12.00	0.81

- V_{stack}^{eff} describes the effective stack volume that contributes to the crossover. This is taken to mean the total volume of all anodic cells in the context of oxygen crossover and, therefore, typically represents half of the actual stack volume. It can be calculated based on the total number of (half-) cells and the volume of the chamber in m^3: $V_{stack}^{eff} = V_{cham} \times N_{cells}$. This relationship shows that equivalent stack volumes can be achieved through small chamber volumes, but a higher number of cells or inversely, a larger chamber volume, but a lower number of cells (Fig. 4.16).

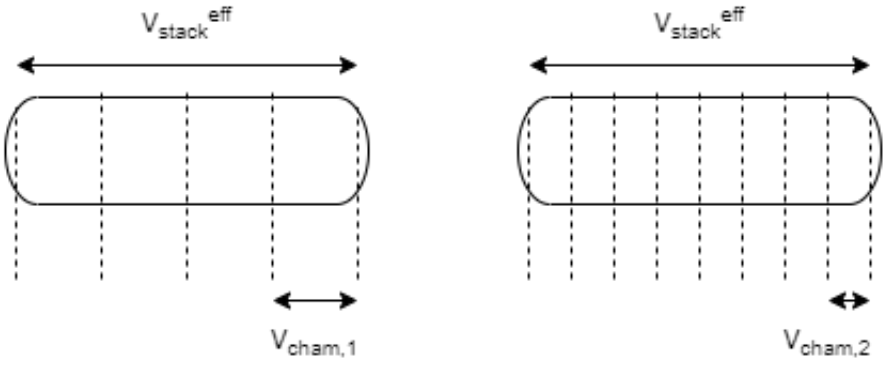

Figure 4.16: An example of the difference in chamber sizing ($V_{cham,1}, V_{cham,2}$) and accompanying number of cells to achieve equivalent effective stack volumes.

Relative Sizing as a Tool

The ratio of $\frac{c_{cross,O_2} V_{stack}^{eff}}{V_{buffer}}$ in Eqn. 4.3 effectively represents the relative sizing of the components within the AEC. Each term was isolated and assessed on how it can be altered to achieve higher gas purity within the hydrogen buffer.

Firstly, the volume of the buffer itself was considered. Based on Eqn. 4.3, it can be concluded that expanding the buffer's size has a positive impact on the purity level. An increase in the buffer's capacity means more hydrogen can be held within its volume, which dilutes the amount of crossover gas.

Secondly, the effective stack volume was considered. Here, the increase in V_{stack}^{eff} was interpreted to mean an increase in the number of cells within the AEC stack. A higher number

of cells translates into a larger volume of crossover gas, which has a negative impact on the purity level. Therefore, opting for smaller stack volumes is favourable in avoiding the risk of a flammable mixture.

Finally, the width of the cell chamber was considered, which is explicitly expressed in the crossover concentration and effective stack volume (c_{cross,O_2} & V_{stack}^{eff}) terms. However, the effect of chamber width cancels itself out through the multiplication of the two terms, i.e. if the width is doubled, the effective stack is doubled and the crossover concentration is halved, negating its effect.

Alternatively, the implicit effect of chamber width on the crossover amount was considered. From previous sections, it was shown that total oxygen crossover accumulation increases with increasing cell width. The cumulative effect scales as $n_{cross,O_2} \times N_{cells}$, which ultimately has a negative impact on the hydrogen purity in the buffer. Therefore, smaller chamber widths should be adopted to limit the amount of crossover.

Wider Implications of Design Equation

While c_{cross,O_2} and V_{stack}^{eff} can be linked and simplified to the total moles accumulated through crossover, keeping crossover concentration as a separate quantity provides a platform for comparison across multiple studies. AWE studies are commonly performed on single cell setups. In future, such a quantity that normalises equilibrium crossover values to its cell volume can facilitate measuring the performance and crossover susceptibility of single cell results from separate studies.

Furthermore, Eqn. 4.3 provides a simple method in assessing how single cell crossover data impacts safety levels if the system were scaled up, or conversely, can be applied to appropriately size buffer or stack components based on desired operation temperatures and pressures.

5

Results on First Study of Explosion Mitigation via Controlled Combustion

In the following chapter, an initial study on the controlled combustion of a hydrogen-oxygen system is presented in the context of ZEF's AEC conditions. Section 5.1 describes the results of the analysis, in which various combustion parameters are investigated as a function of inlet gas stoichiometry. Additionally, the effects of varying pressure and temperature conditions on combustion are presented.

5.1. Study of A Premixed Laminar Hydrogen Flame

5.1.1. Considerations in the Ignition of Trace Oxygen

The primary goal of the gas scavenger is to mitigate the accumulation of trace oxygen to dangerous levels within the buffer through a deliberate, controlled ignition. It has been proposed to achieve this ignition by treating the outlet gas stream of the hydrogen flash tank before it enters the buffer (Fig. 4.15).

The ex-situ placement of the gas scavenger allows its size to be tailored to handle specific and smaller volumes that enable desired burn conditions. This is particularly important for both the safety and success of the H_2-O_2 ignition process within the compact design of the AEC. Given the small amount of oxygen crossover (based ZEF's full 20-stack: 7.95×10^{-4} mol, $\phi = 629$), the H_2-O_2 mixture lies outside the flammability limit (Section 4.2.5). It must, therefore, be determined under which conditions the mixture will ignite. Developing strategies to bring this mixture to ignition in a safe and controlled manner is key in design and operation considerations of the scavenger. These strategies should address when and how frequent the scavenger is switched on (briefly addressed in Chapter 4), as well as how stoichiometry is controlled to maximise the likelihood of ignition.

5.1.2. Hydrogen-Oxygen Combustion Stoichiometry

A premixed laminar H_2-O_2 combustion was investigated to characterise the effect that reaction stoichiometry has on the chemical reaction equilibrium at inlet conditions of 50 bar and 350 K. By varying the equivalence ratio from 0.5 to 3.5 in increments of 0.025, combustion parameters such as the adiabatic flame temperature (AFT) of the product gas and its equilibrium compositions ($x_{i,eq}$) were determined. Additionally, through one-dimensional reacting

flow simulations of a premixed laminar flat hydrogen flame, laminar flame speeds (S_l) were calculated as a function of the equivalence ratio.

Adiabatic Flame Temperature

The AFT has to be investigated to evaluate the expected maximum temperature range that is achieved in an H_2-O_2 combustion, and can be used to assess material design choices of the scavenger components. Calculations were performed using Cantera's *equilibrate* function (Subsection 3.4.2) [18], whereby the enthalpy and pressure were fixed. The computation was validated by ensuring that the forward and reverse rates of progress of all reversible reactions were equal, i.e. the net rate of progress were zero, indicating that an equilibrium had been established [18]. AFT calculations were also validated against literature values for hydrogen-oxygen combustion at $T = 298$K and $P = 1bar$ (Appendix B.1). Results are depicted in Fig. 5.1.

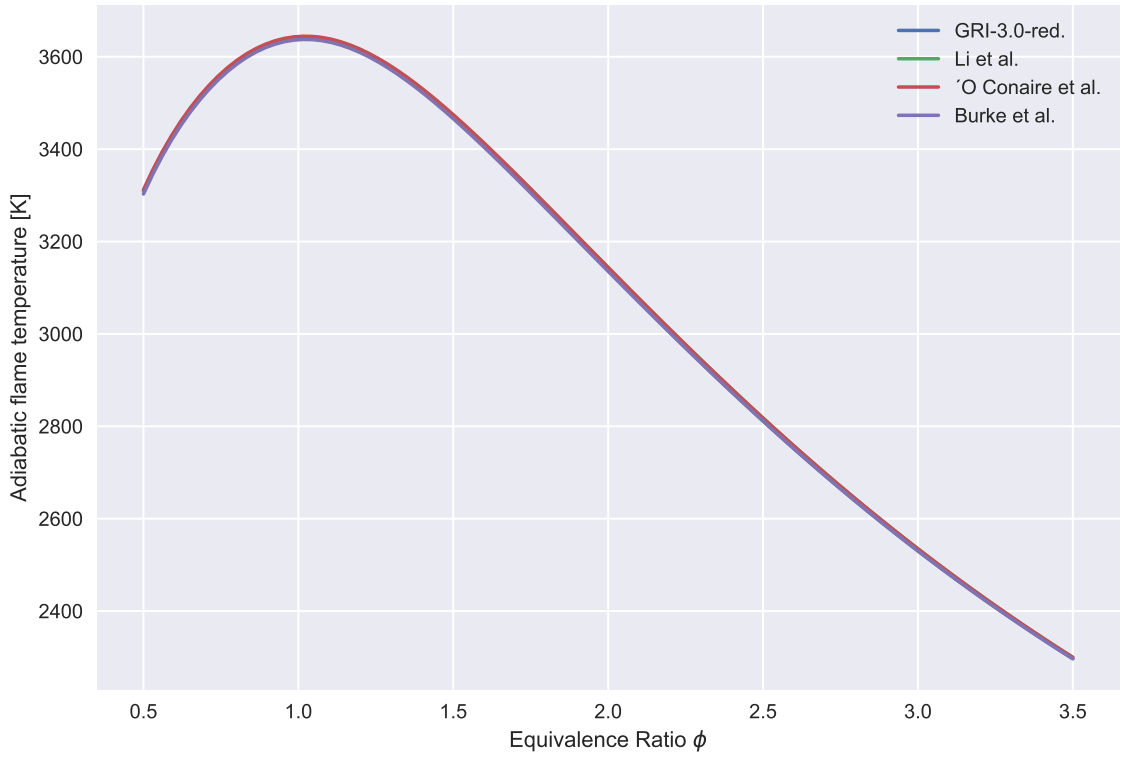

Figure 5.1: Adiabatic flame temperature of the product gases as a function of the equivalence ratio ϕ. Calculations were performed using the mechanisms listed in the legend [15–18]. Initial inlet conditions: 50 bar and 350 K.

The maximum AFT is 3641K at an equivalence ratio of $\phi = 1.03$, which is over 500K more than the AFT commonly reported in literature for $T = 298$K and $P = 1$bar [66, 70]. A shift of the maximum AFT to marginally richer fuel mixtures is a good indication that the simulation and theory for premixed laminar flames are in agreement. This is commonly associated in AFT calculations to the endothermic dissociation of gas products that occurs around stoichiometric equivalence ratios, thereby reducing the heat released [71].

As the equivalence ratio grows and the fuel mixture becomes more rich, the combustion process is incomplete with less oxygen present and the flame temperature decreases. Below stoichiometric conditions, a decrease in the flame temperature is also observed. At leaner

mixtures, only part of the oxygen is reduced, resulting in lower amounts of heat being released, and therefore, a lower flame temperature.

Equilibrium Compositions

Equilibrium compositions were calculated in the same manner as the AFT (Section 3.4.2). The purpose of investigating the outlet gas compositions at varying inlet H_2-O_2 mixtures is two-fold: (a) to determine at which equivalence ratio the outlet oxygen mole fraction is minimised, and (b) to assess to what extent radicals, in particular H, O and OH, appear in the outlet stream. While these radicals are generally short-lived as they recombine to form stable species (particularly at surfaces of the container wall), the accumulation of radicals may lead to unwanted ignition downstream [19, 66, 70]. Furthermore, equilibrium composition calculations at $T = 298$K and $P = 1$bar were also performed and validated against literature values [66]. Outlet composition results are depicted in Fig. 5.2.

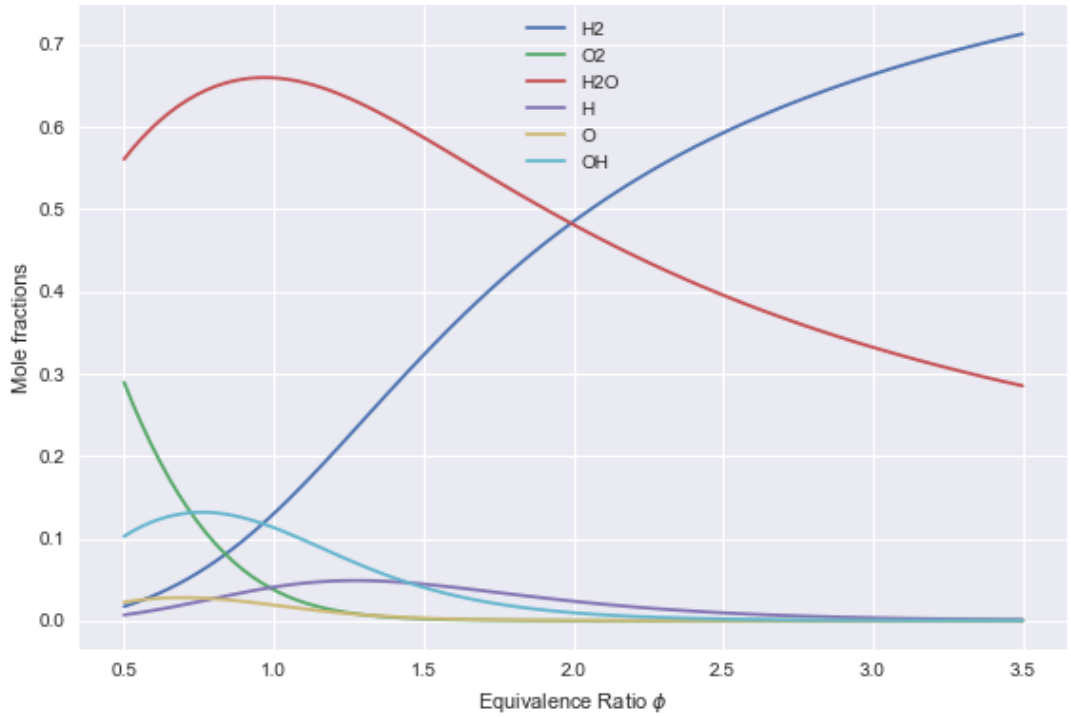

Figure 5.2: Outlet gas stream equilibrium compositions as a function of equivalence ratio ϕ. Calculations are based on the mechanism proposed in Li et al.'s work [15].

The point at which the oxygen mole fraction becomes negligibly small occurs at $\phi = 1.30 - 1.40$. Within this equivalence ratio range, OH and H radicals are present in low amounts relative to other species at $x_{\mathrm{OH},eq} = x_{\mathrm{H},eq} = 0.05 - 0.08$. Here, the mole fraction of water in the product stream is passed its maximum (at $x_{\mathrm{H_2O},eq} = 0.67$) and has begun to decrease. This may partially hint at the aforementioned dissociation (initially after stoichiometry), but can also be attributed to the growing fraction of hydrogen as combustion decreases, which is mirrored in the decrease of the AFT as well (Fig. 5.1).

Laminar Flame Speed

Finally, laminar flame speeds S_l were studied at AEC conditions and modeled as freely-propagating, premixed flat flames with Cantera's *FreeFlame* function under a mixed-average transport model (Section 3.4.3) [18]. Results are depicted in Fig. 5.3. Furthermore, validation was performed

by re-creating literature data found for laminar flame speeds of an H_2-air mixtures at $T = 300$K and $P = 1$bar, and was shown to be in good agreement (Appendix B.1) [65, 66].

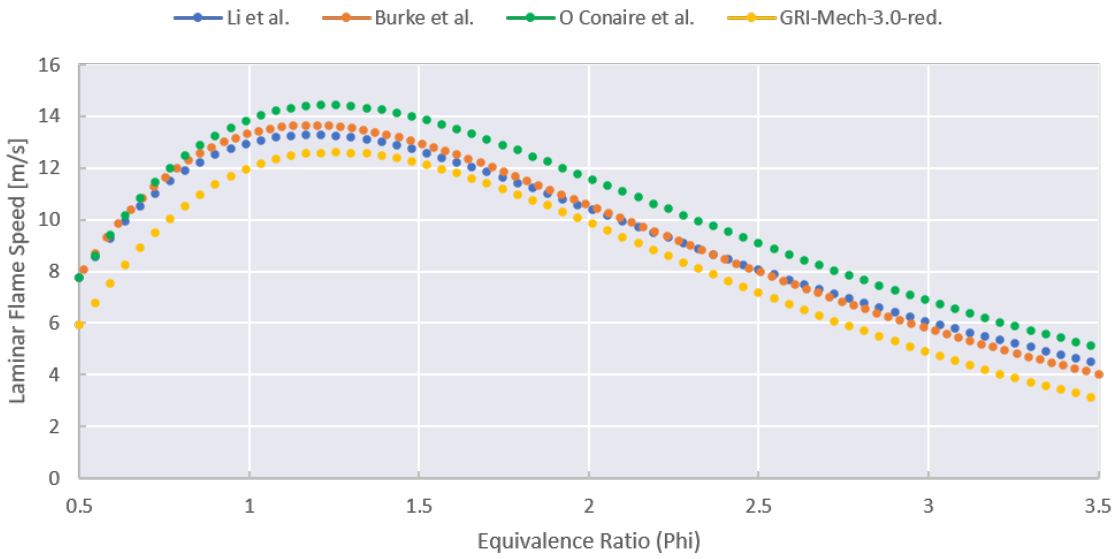

Figure 5.3: Laminar flame speed as a function of equivalence ratio ϕ. Mechanisms [15–18] were applied. Initial inlet conditions: 50 bar and 350 K.

In general, the laminar flame speed is proportional to the (square root of the) thermal diffusivity (Eqn. 3.18), and is thus, dependent on the temperature and its effect on the density across the flame front [66]. It, therefore, follows a similar profile as that of the AFT, steadily increasing towards stoichiometry from leaner mixtures before decreasing at richer fuel regimes, reflected in Fig. 5.3. An average maximum laminar flame speed of 13.50 (± 0.76) m s^{-1} was calculated at an equivalence ratio of $\phi = 1.20$, which follows the same maximum shift towards richer fuel mixtures observed in AFT [71]. However, their peaks do not align, indicating a minor discrepancy between the AFT and laminar flame speed calculations.

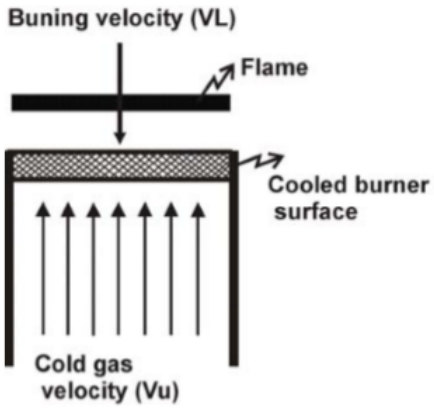

Figure 5.4: Illustration of a flat flame blowing off from the cooled burner surface, where the laminar flame speed v_l is lower than the unburnt gas velocity v_u [19].

5.1.3. Discussion on Scavenger Control Schemes

Target Ignition Conditions

The AFT can be regarded as a measure of a combustion system's reactivity and its maximum represents the point at which the most heat is liberated [66, 67]. Additionally, the laminar flame speed characterises the stability of a flame within the combustion system and its maximum generally coincides with that of the AFT. It determines whether a flame front propagates into the unburnt gas mixture or blows off (Fig. 5.4), which may eventually lead it to extinguish [19, 66]. Therefore, to achieve the best conditions for an ideal combustion result, operating at or close to this maximum (or due to the discrepancy in this case, these maxima) can increase the likelihood of a successful ignition and flame development, summarised in Table 5.1.

Table 5.1: Modeled conditions for a max

	Equivalence Ratio ϕ	Value	Unit
Maximum AFT	1.03	3641	K
Maximum S_l	1.20	13.50	$m\,s^{-1}$

Lastly, fuel mixtures at $\phi = 1.30-1.40$ have also shown to minimise the oxygen outlet mole fraction to negligibly small amounts, further encouraging the notion of operating at slightly richer fuel regimes. Thus, an overall range of equivalence ratios is established and can guide the development of both design strategies for flow management and design features for the scavenger.

Initial Design Considerations

While an in-depth design of a gas scavenger is beyond the scope of this thesis work, the results of the flame study indicate the need for proper material choices and thermal management. Due to the extreme flame temperatures reached, materials are required to show good stability across a large temperature range and should demonstrate suitable resistance to thermal stress to extend the scavenger lifetime.

In addition, design strategies for proper heat exchange need to be considered to ensure the safety of the micro-plant. By reducing the overall temperature, chain propagating reactions initiated by radicals (such as the ones in the product stream) are halted, thereby minimising the risk of unwanted downstream ignition [19]. Moreover, thermal management must specifically address quenching the propagating flame to avoid a subsequent deflagration or detonation within the buffer or AEC stack lines. Flame quenching can be achieved either through a flame arrestor or through the use of a sufficiently long channel, whereby the flame loses heat through its exchange with the walls (Fig. 5.5, tube quenching) [20, 67].

5.1.4. Pressure and Temperature Dependence of Laminar Flame Speed

The effects of inlet pressure and temperature on laminar flame speeds have to be investigated to further validate the flame speed study at AEC conditions as literature data on pure oxygen hydrogen combustion for direct comparison was scarce. Calculations were performed for both H_2-O_2 as well as H_2-air systems.

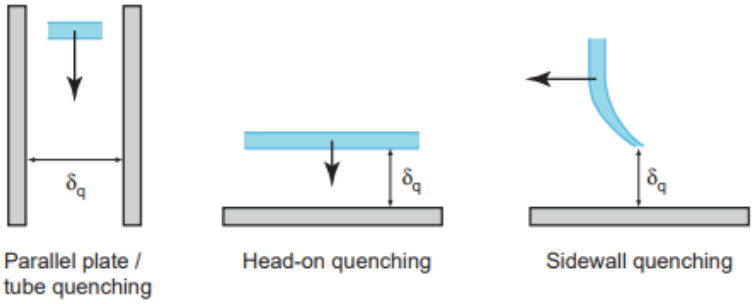

Figure 5.5: Cold wall quenching examples described in three different scenarios [20].

As not all mechanisms included data on nitrogen species, a diluted gas mixture was used in place of air by incorporating argon gas when necessary. This was done in particular for the hydrogen-oxygen reaction mechanism within Cantera's software library ('h2o2.cti') [18]. Data shown in subsequent sections is obtained using the Li et al. chemical mechanism (Figs. 5.6, 5.7, 5.8, 5.9) [15].

Temperature Normalisation

The effects of temperature were studied relative to standard conditions. This means the laminar flame speed S_l at inlet temperature T was normalised to the laminar flame speed S_l^0 at $T^0 = 300$K. Throughout, the pressure was maintained at $P = 1$bar, while the temperature was varied from 300 to 800 K. Results are depicted for H_2-air and H_2-O_2 in Fig. 5.6 and Fig. 5.7, respectively.

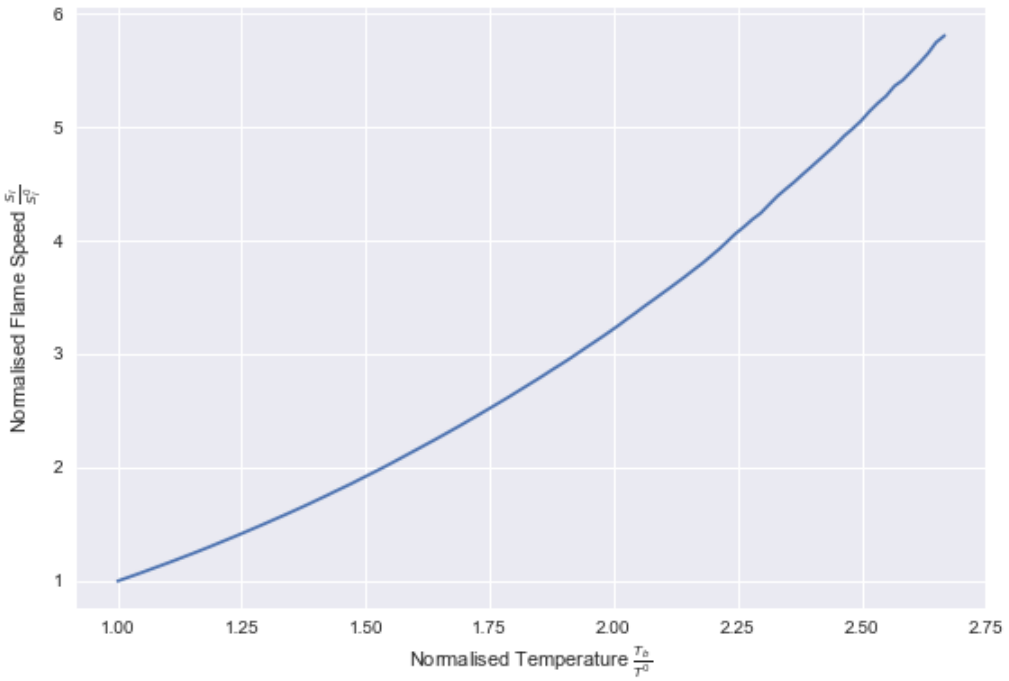

Figure 5.6: Profile of the laminar flame speed as a function of temperature, normalised to their values at ambient condition, for an H_2-air mixture. $P = 1$bar, $\phi = 1.0$; Mechanism: Li et al. [15].

With increasing inlet temperature, the laminar flame speed is observed to increase more rapidly than linearly, reaching over five times its value as it approaches $T = 800$K. Referring to literature studies on the temperature dependence of laminar flame speeds, the observed trend shows good agreement [66]. An increase in the inlet temperature accelerates the reaction rates of the system, thereby raising the (adiabatic) flame temperature. As the laminar flame speed is a function of and proportional to the flame temperature, an increase in its value is observed [19, 66, 70].

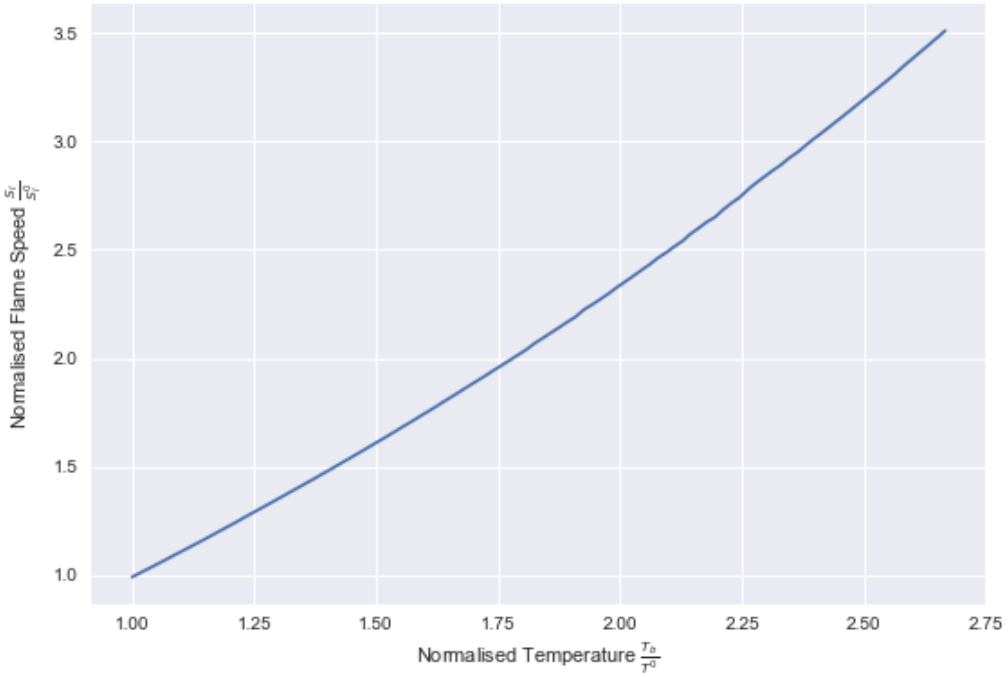

Figure 5.7: Profile of the laminar flame speed as a function of temperature, normalised to values at their ambient condition, for an H_2-O_2 mixture. $P = 1$bar, $\phi = 1.0$; Mechanism: Li et al. [15].

Similar to the data plotted for H_2-air, an increase in the flame speed is observed at increasing inlet temperatures in H_2-O_2 mixtures. With the absence of nitrogen, the plot is closer to linear and the flame speed reaches a lower maximum at 3.5 times its standard value.

Pressure Normalisation

In addition to temperature, the effects of varying pressure on the laminar flame speed were studied relative to standard conditions. Once again, laminar flame speeds S_l at inlet pressures P_{in} were normalised to the laminar flame speed S_l^0 at $P^0 = 1$bar. Throughout, the inlet temperature was maintained at $T = 300$K, while the pressure was varied from 0.1 to 10 bar in increments of 0.1 bar, and then from 10 to 100 bar in increments of 1 bar. As before, the study was conducted for H_2-air and H_2-O_2, and is depicted in Fig. 5.8 and Fig. 5.9, respectively.

At pressures below $P_{in} = 1$bar, a flame speed below unity is observed, indicating that the corresponding flame speeds are lower than at standard conditions. This is also observed for pressures greater than $P_{in} = 1$bar. With increasing pressure, the laminar flame speed decreases exponentially and results in a value lower than 20% of its standard value at $P_{in} = 100$bar.

This observation is in agreement with literature data [15, 17, 65]. The simulation data suggests that the pressure suppresses the flame speed, and may be traced to its effect on

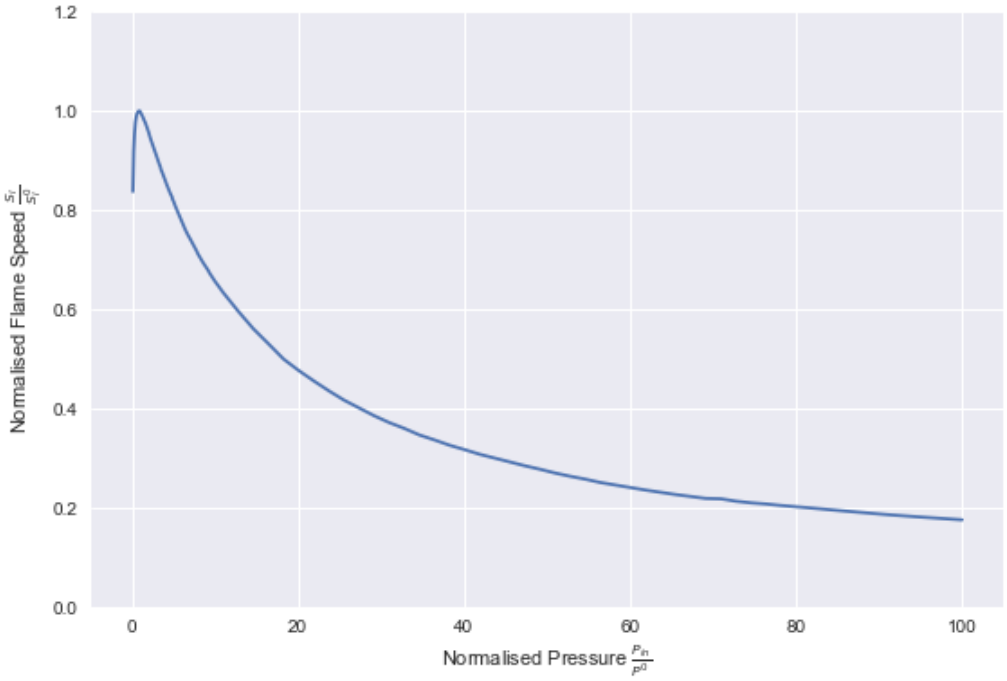

Figure 5.8: Profile of the laminar flame speed as a function of pressure, normalised to their values atambient condition, for an H_2-air mixture. $T = 300$K, $\phi = 1.0$; Mechanism: Li et al. [15].

the density. As the pressure increases, the density increases, thereby effectively reducing the thermal diffusivity [69]. As the flame speed is proportional to (the square root of) the diffusivity in laminar premixed flames (Eqn 3.18), the result is a reduced laminar flame speed with increasing pressures [66].

For H_2-O_2 systems (Fig. 5.9, the initial decrease in the flame speed below unity for pressures lower than $P_{in} = 1$bar follows the same trend as its H_2-air counterpart. However, unlike in H_2-air systems, an increase in the pressure beyond 1 bar results in a larger flame speed, until it peaks at just below 1.2 times its standard value at a pressure around 10 bar. From this point onward, a larger pressure translates into a quasi-linearly decreasing laminar flame speed.

Based on its trend, the simulation data demonstrates the existence of a point at higher pressures, where the flame speed obtains the same value as at standard conditions, which is given here at 60 bar, and is observed to varying extents across each mechanism (Appendix B.1). In each case, a positive correlation between increasing pressure and laminar flame speeds exist for moderate pressure ranges (10-20 bar), resulting in a peak flame speed value above unity.

Outcome of Flame Speed Study

The results of pressure and temperature effects on H_2-air combustion systems reflected general trends as expected from theory and literature. With increasing inlet temperature, the laminar flame speed increases; with increasing inlet pressure, the laminar speed decreases. These effects were explained through the increase in reaction reactivity and decrease in the diffusivity, respectively.

Though temperature effects are smaller in the case of an H_2-O_2 mixture, the trend resembles that of an H_2-air system. Pressure effects, however, differ significantly. The difference

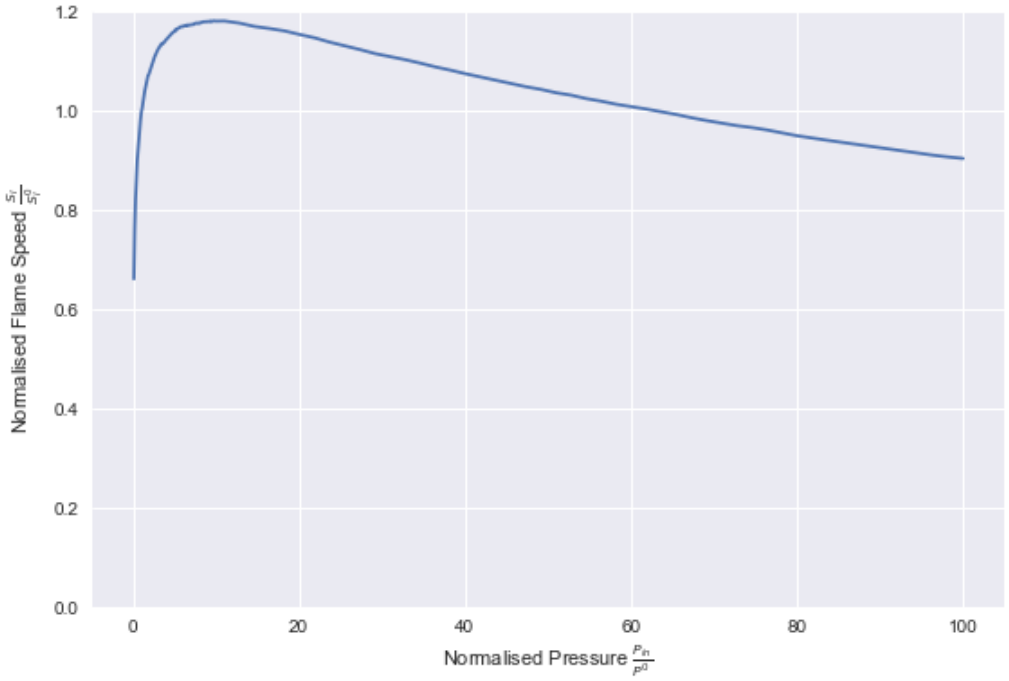

Figure 5.9: Profile of the laminar flame speed as a function of pressure, normalised to values at their ambient condition, for an H_2-O_2 mixture. $T = 300$K, $\phi = 1.0$; Mechanism: Li et al. [15].

points to an absence of the influence that three body reactions have in hydrogen-oxygen mechanisms without a third species present, i.e. nitrogen or argon [15, 17, 19]. Further analysis is necessary to characterise this phenomenon, in order to understand whether this abnormality is occurring on a chemical mechanistic level or software implementation level.

This finding does not necessarily make the results of the stoichiometry study performed on laminar flame speeds in Section 5.1.2 meaningless. The implementation of the model as well as the prediction accuracy of the mechanisms applied in the study were confirmed and validated against data found in literature [17, 65, 66]. Additionally, the general shape and trend of the flame speed (Fig. 5.3) matches that of the AFT profile as described in literature [66, 71]. Therefore, this may indicate that the conclusions drawn regarding optimal ignition conditions and equivalence ratios can still be assumed to be true, but the value of the laminar flame speed itself is inaccurate, requiring further analysis.

5.1.5. Ignition Delay Time Study

Finally, an ignition delay time (IDT) study was performed to investigate how long it would take an H_2-O_2 mixture at 50 bar and $\phi = 1.0$ to auto-ignite under a range of initial temperature conditions. The criterion of the IDT applied in this study was the time after which the formation of OH was observed [66]. The temperature range considered was between 700 and 2000 K, varied in increments of 50 K. Convergence of solutions below 700 K was not possible[1]. The model was validated against data in Karimkashi et al.'s work for H_2-air mixtures at 1, 4 and 16 bar (Appendix B.1). Results are plotted as the logarithm of the IDT versus the reciprocal of the reactor temperature and are depicted in Fig. 5.10.

[1]For IDT studies, an initial time guess is required for temporal discretisation. Despite setting it to the equivalent of 1 year, the solution did not converge.

According to theory [66], an exponential relationship should exist between the IDT and the reciprocal of the temperature and is, indeed, reflected in the linear slope obtained in the graph. This linearity is observed between a reactor temperature of 700 and 1300 K. In the span of this temperature change, the IDT shifts from 10^1 second regime to the microsecond regime. The exponential relationship, is interrupted at increasing temperatures between 1300 and 1500 K, indicated by the curve's shift from linear to rapid decay. However, linearity is once again established above 1500 K, but has a smaller slope than previously observed. This change in slope and brief divergence from its linear relationship possibly marks a transition phase. Further investigation in the form of a sensitivity analysis is required in order to properly characterise this observation.

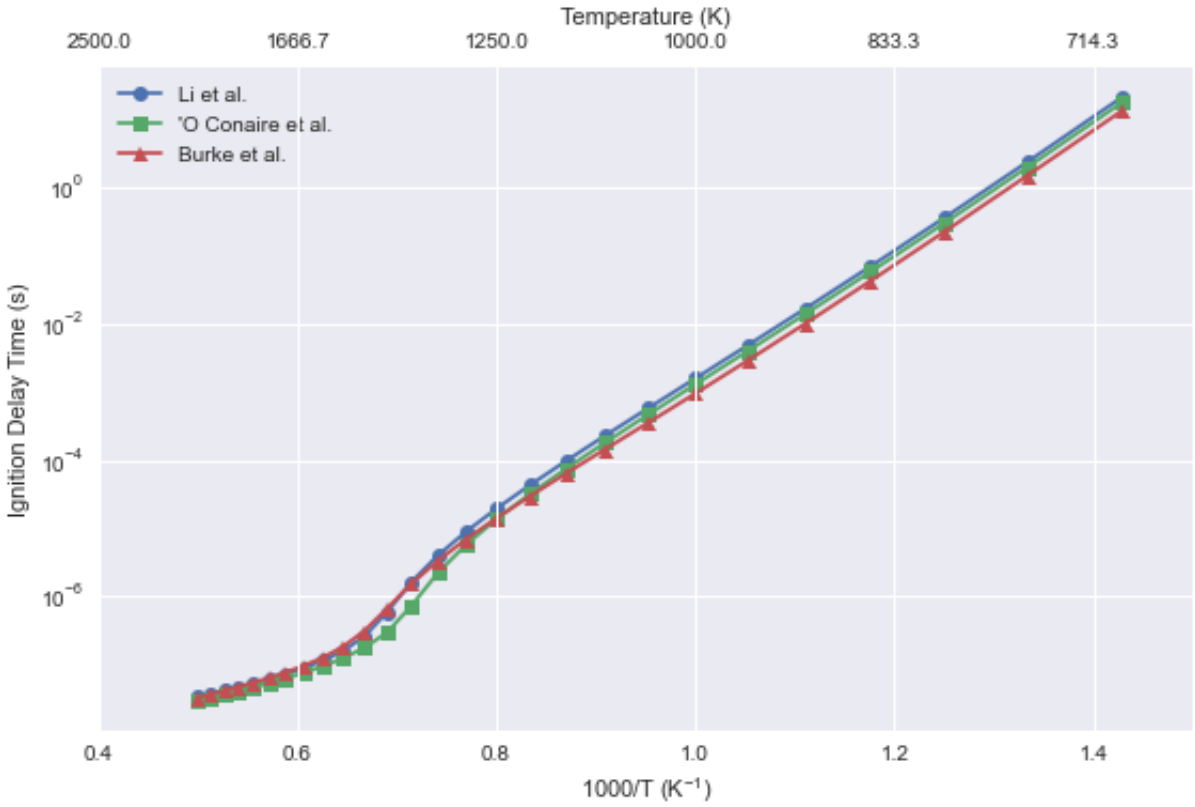

Figure 5.10: Ignition delay times plotted against temperature expressed as $1000/T$ in K. Mechanisms [15–17].

The IDT plays a vital role in the process of induced ignition phenomena, such as in spark ignition, as it initiates the flame propagation [66]. In the context of this work, IDT data can be applied to the ignition timing of the scavenger. Depending on the amount of crossover expected (overnight vs. lower current density or standby conditions), the scavenger may be deployed in a series of short ignition bursts, requiring an IDT in the milli- to microsecond range that corresponds to temperatures above 1000 K, or a single long ignition, where lower temperatures are acceptable. Additionally, understanding IDT helps ensure that ignition happens at the exact moment it is intended to be used, which is particularly important since it is not run continuously and only operated in specific situations.

6

Conclusions and Recommendations

The purpose of this thesis was to study the feasible development of a gas scavenger prototype that can remove trace oxygen contamination within ZEF's AEC system. Three distinct objectives were set at the start of this project to provide a framework for analysis (Subsection 1.3). The conclusions for each and recommendations for future work are presented in the following sections.

6.1. Process Technology Evaluation

A literature review was conducted on a wide range of technologies that exist in industry to either address hydrogen gas impurities or the build-up of flammable $H_2 - O_2$ mixtures. Based on ZEF's project boundaries, the following technologies were shortlisted: pressure swing adsorption (PSA), platinum-based catalytic recombination, palladium membrane technology, electrochemical hydrogen purification (EHP), and deliberate hydrogen ignition.

A subsequent study on the critical factors determining an option's feasibility was performed from a technical and economic viewpoint for its suitability in ZEF's system:

- The study revealed that PSA would strain the balance of power within the micro-plant due to its high energy consumption, using up to 29% of the eight hour solar energy output under continuous operation. While this drops to 10% when assuming a run time of two instead of eight hours, PSA was not considered a feasible option.
- Furthermore, the use of either a platinum catalyst or palladium membrane was shown to be outside of ZEF's target budget, constituting on average between 10 to 30% and 11 to 34% of the capital expense, respectively, at lower budget ranges (€100-300 per device).
- Though EHP showed to be promising for small-scale applications, it was ultimately discarded as (a) it required strict water management for predictable reliability of the membrane performance, (b) has typically employed a platinum catalyst for the inefficient hydrogen oxidation at the anode, and (c) has been prone to gas crossover as well.
- The potential for a micro-scale hydrogen igniter design (a *micro-combustor*) was conclusively chosen for its greater thermal control, improved process safety and design flexibility, taking advantage of the inherent combustion properties of hydrogen.

6.2. Crossover Prediction Modelling

Two primary situations were considered for crossover analysis: during AEC operation and during micro-plant downtime. In each case, quantitative methods were implemented to evaluate impurity levels and their safety implications with respect to LEL and UEL (tolerance) levels.

For in-operation conditions, a non-dimensional model approach was extended from literature and applied to analyse the effect of 50 bar pressure on crossover phenomena. For reactor downtime conditions, a literature gap was identified and led to the development of a transient, two dimensional diffusion model to quantify the potential risk of trace O_2 accumulation in the H_2 buffer overnight.

During operation, it is crucial to maintain a pressure balance at or below a 0.1% cell pressure difference. If this differential pressure is exceeded while operating at target AEC current density (0.33 $A\,cm^{-2}$), the system reaches dangerous impurity levels and can be exacerbated through dynamic operation. In this case, it is recommended to deploy the gas scavenger and purge the oxygen flash tank at shorter intervals. Additionally, below a current density of 0.05 $A\,cm^{-2}$, it is recommended to shut down the AEC as the impurity levels tend to 100%.

The research shows though that a gradient in pressure or concentration across the membrane will persist after shutdown and may require the use of the gas scavenger. Further work on system characterisation will, therefore, benefit devising appropriate control schemes for post-shutdown procedures as well as validate the extent of the cross-permeation in the AEC.

O_2 crossover was found not to reach the H_2 buffer overnight. Eight hours after shutdown, a concentration equilibrium is established and crossover accumulation is limited to the cell as the chamber outlet presents a bottleneck to the diffusion process. Additional geometry analysis of AEC components indicated that the amount and effect of crossover can be further limited by opting for thinner chambers, smaller stack volumes or larger buffer volumes.

Upon startup this O_2 accumulation is likely transported to the H_2 flash tank, where it degases. However, even assuming that all of the oxygen degases, it only represents a 0.079 mol % contamination relative to the hydrogen in the buffer. Overnight crossover, therefore, does not pose a severe safety hazard to the integrity and operation of the AEC.

A low to moderate safety risk posed by the build-up of trace oxygen on a monthly timescale cannot be ruled out though. Analysis of the buffer's volume showed that no local accumulation zones are formed in the degassing process as a homogeneous mixture is obtained within six hours. Therefore, in order to manageably mitigate the O_2 accumulation to dangerous levels, it is recommended to place the gas scavenger between the hydrogen flash tank and buffer, and to run the scavenger upon startup as well.

A short- and long-term study for experimental data collection on oxygen build-up is recommended for validation of this thesis work. Furthermore, it is proposed to extend the overnight crossover model to include effects of the AEC electrolyte cycling strategy, convective mass transport and non-isothermal heat effects to reflect real-world phenomena, particularly during startup and shutdown phases of the AEC. Additionally, opting for a different method to implement the model may benefit the computation time and address drawbacks of the FDM scheme. Applying a finite volume method would, for instance, address the mass conservation issues faced in this work [72].

6.3. Controlled Combustion Simulation

Based on the outcome of the process technology evaluation, the feasibility of a local combustion process was preliminarily explored. Using Cantera's Python interface, initial simulations were carried out to study premixed laminar flame parameters that characterise a controlled combustion process. Ignition has not been investigated in this study and is left for future work.

The primary goal of the scavenger is to remove the trace amounts of oxygen that emerge in the AEC hydrogen outlet stream due to crossover. This is intended to be achieved by oxidising the trace oxygen with part of the available hydrogen. However, due to the small amount of oxygen present based on crossover modelling results, the mixture is outside the flammability limit. Design strategies must consider how to induce an ignition in a safe and controlled manner. A small volume tailored to achieve ignition conditions based on the crossover amount is suggested. The scavenger would operate as a 'micro-combustor'.

Ideal ignition conditions were determined at an equivalence ratio range of $\phi = 1.03 - 1.40$. In this range, both the AFT as well as laminar flame speed are maximised, and the outlet mole fraction of oxygen is minimised. How these conditions can be established in the gas scavenger is a matter of further research and will be determined by the scavenger design, geometry as well as its ignition chamber volume.

A maximum theoretical flame temperature of 3641 K was calculated, stipulating the need for proper thermal management and material design. For safe operation of the gas scavenger within the AEC, it must be ensured that the evolving flame is quenched to avoid unwanted deflagration or detonation in up- or downstream processes that may compromise the integrity of the buffer or AEC stack. The combustion process, must, therefore be contained in a well-defined region of the AEC. Furthermore, a stable material must be chosen to withstand the large temperature changes and related thermal stress induced by ignition cycles to guarantee structural integrity and an extended lifetime of the scavenger. These details will be important in the design of the micro-combustor and is recommended for further study.

Finally, results on laminar flame speed and its dependence on temperature and pressure for a freely propagating flame have been presented. Despite model validation against literature results, an important observation revealed a mismatch between theory and simulation for the laminar flame speed of H_2-O2 mixtures. An increase in its value was observed at higher pressures, but should instead demonstrate a decreasing trend with increasing pressure. Further investigation is necessary to determine the cause.

A

Supplementary Data and Information on Gas Crossover Modelling

A.1. In-Operation Model

Parameterised Crossover Equations for In-Operation Model

The following equations have been adapted from Schalenbach et al.'s and from Trinke et al.'s work [21, 57]:

Alternative Form of Fick's Law

$$N_i^{fick} = \frac{D_i^{sep} \times S_i^{sep}}{d_{sep}} \times (P_i^{cat} - P_i^{an}) = \frac{\epsilon_i^{fick}}{d_{sep}} \times P_i^j \tag{A.1}$$

where N_i^{fick} is the molar flux due to diffusional crossover in $\mathrm{mol\,m^{-2}\,s^{-1}}$, D_i^{sep} is the diffusion coefficient of the species i in the separator in $\mathrm{m^2\,s^{-1}}$, S_i^{mem} is the solubility of species i in the separator in $\mathrm{mol\,m^{-3}\,Pa^{-1}}$,$d_{sep}$ is the separator thickness in m, P_i^{cat} and P_i^{an} are the partial pressures of species i in the cathodic and anodic chambers, respectively, in Pa. ϵ_i^{fick} is the separator-specific diffusivity of species i in $\mathrm{mol\,m^{-1}\,s^{-1}\,Pa^{-1}}$ and is used in place for the diffusion and solubility coefficient as it is more readily determined by characterising the separator [21]. The pressure difference is approximated as P_i^j, where i and j correspond to either H_2 on the cathode side or O_2 on the anode side. This is accepted under the assumption that $P_{H_2}^{cat} >> P_{O_2}^{an}$ in the case of hydrogen crossover, and vice versa for oxygen crossover.

Alternative Form of Darcy's Law

$$N_i^{darcy} = \frac{K_{sep}}{\eta} \times S_i^{sep} \times P_i^j \frac{(P^{cat} - P^{an})}{d_{sep}} = \epsilon_i^{darcy} \frac{(P^{sys} \times x_{\delta tol})}{d_{sep}} \tag{A.2}$$

where N_i^{darcy} is the convective molar flux due to a differential pressure in $\mathrm{mol\,m^{-2}\,s^{-1}}$, K_{sep} is the hydraulic permeability related to the separator in $\mathrm{m^2}$, η is the dynamic viscosity of the electrolyte in Pa s, P_i^j is the partial pressure of species i in the chamber j where it is produced (i.e. i = H_2, j = cathode or i = O_2, j = anode), $(P^{cat} - P^{an})$ represents the pressure difference between the half-cells in Pa, and d_{sep} is the separator thickness in m. Here, ϵ_i^{darcy} represents the separator-specific permeability in $\mathrm{mol\,m^{-1}\,s^{-1}\,Pa^{-1}}$ and is driven by the pressure difference. Additionally, the cell differential pressure is simplified as the applied system pressure multiplied by a factor $x_{\delta tol}$ in percent.

Zirfon™ Separator Characterisation

The following parameters were adopted from Schalenbach et al. [21]. These parameters correspond to the mass transfer characteristics of the membrane separator that are used in the equations above and were determined in previous studies by Schalenbach et al. [73, 74]:

Table A.1: Diffusivity and permeability coefficients for hydrogen and oxygen in a Zirfon™ Perl separator. Adapted from [21].

Parameter		Unit
$\epsilon_{H_2}^{fick}$	$(1.4 \pm 1.0) \times 10^{-12}$	$mol\,cm^{-1}\,s^{-1}\,bar^{-1}$
$\epsilon_{O_2}^{fick}$	$(0.7 \pm 0.6) \times 10^{-12}$	$mol\,cm^{-1}\,s^{-1}\,bar^{-1}$
$\epsilon_{H_2}^{darcy}$	$(1.4 \pm 1.0) \times 10^{-10} \times P_{H_2}^{cat}$	$mol\,cm^{-1}\,s^{-1}\,bar^{-1}$
$\epsilon_{O_2}^{darcy}$	$(0.7 \pm 0.5) \times 10^{-10} \times P_{O_2^{an}}$	$mol\,cm^{-1}\,s^{-1}\,bar^{-1}$

Model Validation Through Literature Data Recreation

Before adapting the approach for ZEF's conditions, the in-operation model was used to recreate the cross-over data sets for AHC under conditions of 6 bar, 80 °C and the use of a (theoretical) 57 µm thick Zirfon™ Perl separator as reported by Schalenbach et al. [21]. Following crossover mass transfer equations described by Fick's and Darcy's law and employing the parameters (ϵ_i^{fick}, ϵ_i^{darcy}) as determined in their study (Subsection A.1), the data for AHC was successfully re-created (Fig. A.1). It should be noted that for the purpose of comparison, tabulated values were not available, but were derived from the graphs available in literature [21].

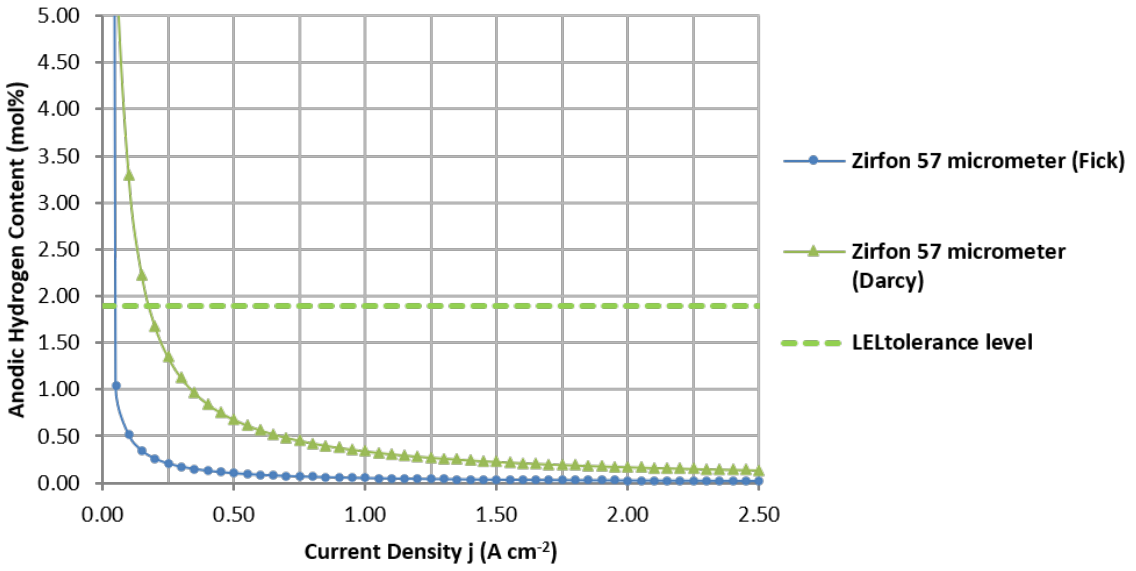

Figure A.1: Plot of recreated hydrogen crossover data as a function of current density from Schalenbach et. al's study [21], represented in the form of the anodic hydrogen content (AHC). LEL tolerance represents 50% of the lower explosion limit as stipulated by Schroeder and Holtappels [14].

A.2. Reactor Downtime Model

Gas Solubility Prediction

The first step involves applying Henry's law to estimate gas solubilities in pure water. Henry's law is a gas law that predicts the amount of gas soluble in a particular solvent at a given temperature and partial pressure when the involved gas is in equilibrium with the solvent [57]. Henry constants, given in its volatility form in units of atm or Pa, for O_2 and H_2 were first determined based on the following empirical equation [25]:

$$A(log\bar{H}_i)^2 + B(1/\bar{T})^2 + C(log\bar{H}_i)(1/\bar{T}) + D(log\bar{H}_i) + E(1/\bar{T}) - 1 = 0 \tag{A.3}$$

where $\bar{H}_i = H_i$ (in atm) $\times 10^{-4}$, and $1/\bar{T} = 1/T$ (in K^{-1}) $\times 10^3$. By specifying the temperature in its appropriate form, the Henry constants H_i can be solved for using coefficients A through D of each gas species [24, 25]:

Table A.2: Hydrogen- and oxygen-specific Henry coefficients in water. Valid for temperature range T = 273-353 K. Adapted from [24, 25].

Gas	A	B	C	D	E
H_2	-0.1233	-0.1366	0.02155	-0.2368	0.8249
O_2	-0.0005943	-0.1470	-0.05120	-0.1076	0.8447

Next, with the Henry constant calculated, gas concentrations in pure water can be estimated as follows [12, 25]:

$$c_{i,H_2O} = \frac{\rho_{H_2O}}{M_{H_2O}} \times \frac{(P_i - P_{H_2O})}{101325\text{Pa} \times H_i} \tag{A.4}$$

where c_{i,H_2O} is the equilibrium concentration of species i in water in mol m^{-3}, ρ_{H_2O} is the density of water in kg m^{-3}, M_{H_2O} is the molar mass of water in kg mol^{-1}, P_i and P_{H_2O} are the species partial pressure and water vapour pressure, respectively, in Pa, and H_i is the previously calculated, species-specific Henry constant in atm. A conversion factor from Pascal to atmospheres is included to match the units between the pressures and Henry constant.

In the final step in estimating gas solubilities in a potassium hydroxide solution, the Setchenov equation is applied [12, 25]:

$$log(\frac{c_{i,H_2O}}{c_{i,KOH}}) = K_i \times w_{KOH} \tag{A.5}$$

where c_{i,H_2O} is taken from the previous step (Eqn. A.4), $c_{i,KOH}$ is the equilibrium concentration of species i in potassium hydroxide in mol m^{-3} (the objective variable), K_i is the Setchenov constant specific to the dissolved gas species interaction with potassium hydroxide, and w_{KOH} is the mass fraction of potassium hydroxide in electrolyte solution given in %.

Table A.3: Setchenov constants for hydrogen and oxygen in potassium hydroxide. The constants are valid for a mass fraction range of 5.4 to 39.8 wt% of KOH and were determined at 75 °C. Adapted from [12, 25].

K_{H_2}	3.14
K_{O_2}	3.66

Diffusion Coefficient of Gas Species in Potassium Hydroxide

The following equations and coefficient data was adapted from Haug et al.'s work [12]:

$$D_{\mathrm{H_2,KOH}} = \sum_{n=0}^{2} D_{\mathrm{H_2,KOH},n} \times (w_{\mathrm{KOH}})^n \tag{A.6a}$$

$$D_{\mathrm{O_2,KOH}} = \sum_{n=0}^{3} D_{\mathrm{O_2,KOH},n} \times (w_{\mathrm{KOH}})^n \tag{A.6b}$$

Table A.4: Binary diffusion coefficients for hydrogen and oxygen in a potassium hydroxide electrolyte. The valid range of this relationship is 20-47 wt% for H_2 and 10-47 wt% for O_2, both at T = 80 °C. Adapted from [12].

	H_2	O_2
$D_{i,\mathrm{KOH},0}$	$1.149\,83 \times 10^{-8}$	$6.091\,67 \times 10^{-9}$
$D_{i,\mathrm{KOH},1}$	$-2.672\,73 \times 10^{-8}$	$-2.040\,451 \times 10^{-8}$
$D_{i,\mathrm{KOH},2}$	$2.345\,82 \times 10^{-8}$	$3.905\,84 \times 10^{-8}$
$D_{i,\mathrm{KOH},3}$	-	$-2.157\,85 \times 10^{-8}$

Model Solution Procedure

The model was developed in MATLAB™ and comprised of four different levels:

1. Thermodynamic Property Definition
2. Mesh Generation
3. FDM Execution
4. Data Processing and Plotting

1. Physical Property Definition

Using correlations from literature data sets [12], fluid and membrane material properties were defined based on inputs for applied system pressure and operating temperature. This included densities for KOH and H_2O, diffusion coefficients for oxygen and hydrogen in both water and within the membrane, membrane porosity and tortuosity, Henry's coefficient in its volatility form for oxygen and hydrogen as well as their respective Setchenov coefficients (Subsections A.2 & A.2).

2. Mesh Generation

AEC dimensions were imported. The mesh resolution was limited by the shortest dimension of the smallest component(s), meaning the total amount of nodes in the x and y direction were chosen to discretise these components with sufficient detail for model accuracy, thereby determining spatial step sizes Δx and Δy. These step sizes were then used to spatially discretise each component's dimensions. A matrix was subsequently generated based on the total sum of nodes in each direction and each component was *mapped* in relation to another within this two-dimensional space.

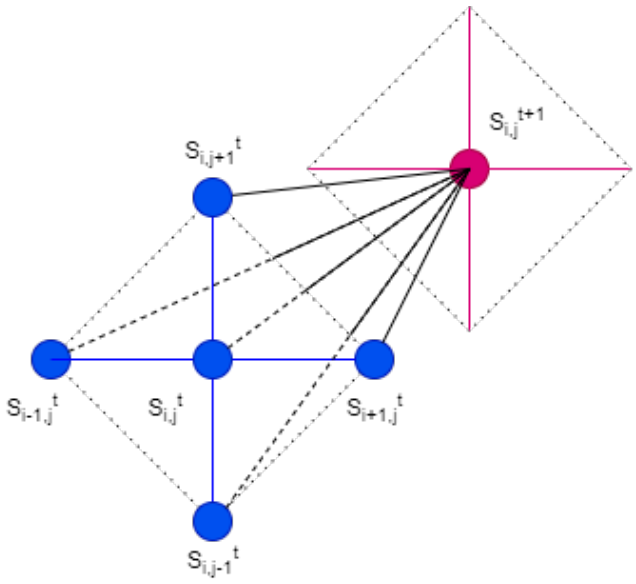

Figure A.2: General 3D matrix nodal representation of applying a forward in time, central in space (FTCS) FDM stencil as described in Eqn. 3.9d. Blue dots represent the matrix of time t, while the red dot represents the matrix of time t+1.

The desired species to model (H_2 or O_2) and the crossover time period, i.e. the time in which crossover occurs after the AEC is shut down, was then specified and discretised with an initial guess for Δt. Based off of the final Δx and Δy values and the corresponding diffusion coefficient, this initial guess was evaluated against the stability condition in Eqn. 3.10 and refined by halving the time step size until condition is met.

3. FDM Execution

To implement the FDM FTCS scheme, embedded for loops were used that applied the stencil (Eqn. 3.9d) element-wise to the mesh, accounting for boundary conditions. To account for the temporal development, a three-dimensional matrix was used to store concentration information within the two-dimensional space while using the third dimension as a way to represent concentration information across time,i.e. matrix $S(i,j,k)$ is equivalent to concentration values at time step t=k. This process is illustrated by Fig. A.2.

Due to the large amount of data that was created in the process, an m by n by two 3D matrix approach was adopted. This meant that only two subsequent time steps were considered at a time, with the latest time step's output ($t = t_1$, red dots in Fig. A.2) then updating or overwriting the data in the previous time step ($t = t_0$ becomes $t = t_2$). This process was repeated until all time steps were completed.

4. Data Processing and Plotting

At specified time steps, flux values, total anodic and cathodic chamber concentration values were recorded for further processing in Excel. Information on percent differences in starting and final mass were stored as well to ensure the mass conservation law. At a $> 5\%$ difference, the mesh was refined. Lastly, final concentration distribution plots were generated as displayed images based on data stored in the last 3D matrix.

Model Assessment and Modifications

Before the results can be evaluated, a model must undergo a process of verification and validation [64, 75]. Verification is accepted to mean the assessment of the whether a model

was implemented correctly, while validation's definition is adapted to represent how accurate, within a tolerable range, the results provide insights into the intended purpose of the study given a set of conditions. This can go as far as to mean how well a model reflects real-world behaviour [75].

Verifying Model Implementation

Previous iterations of applying FDM to a simple one-dimensional case were used to evaluate the model approach techniques chosen for the reactor downtime (RD) model. As a proof-of-concept, a basic 1D model was built to represent a tank or slab filled with KOH electrolyte that was infinitely long (Fig. A.3). A Dirichlet boundary was applied at one end to simulate a constant gas source. Results were displayed as an animation, with graphs being produced at every time step, to observe the development of concentration over time (up to 24h) and limiting mass transfer cases were examined by adjusting source and diffusion coefficient magnitude.

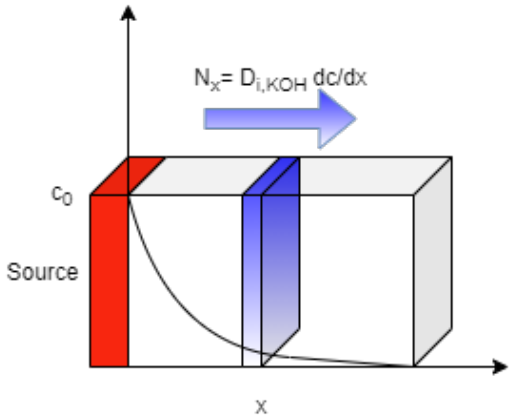

Figure A.3: Simplified schematic of 1D diffusion model in KOH tank with an overlay plot of concentration c versus position x at time t.

The monitored trends reflected behaviour as expected and predicted by Fick's law, and that the manner in which the FDM stencil (Eqn. 3.9d) was implemented in MATLAB works for the intended diffusion modelling.

Managing Node Information

As the fundamental principles of applying FDM to diffusion were confirmed, verifying the correct implementation of the RD model largely dealt with proper data management due to the larger mesh, and mesh sizing to ensure the stability and accuracy of the model were met. Regarding data management, with a 1100 by 1800 matrix being generated, storing temporal information in a 3D matrix that consisted of 8000 time steps, i.e. a 1100 by 1800 by 8000 3D matrix, was not feasible. By adopting an i by j by two 3D matrix approach, wherein data outputs are cycled to overwrite information from previous time steps (Subsection A.2), updating and processing data sets became more manageable and error tracing was facilitated through establishing a clearer overview of nodal information.

Justifying Mesh Sizing

In addition to guaranteeing solution convergence through the stability analysis (Eqn. 3.10), mesh sizing and its effect on mass conservation had to be investigated. The use of an FDM approach inherently leads to truncation errors through the neglect of higher order terms in the Taylor series expansion (Subsection 3.3.3), which can lead to expected differences when

considering total system mass conservation. Further grid refinement may reduce the errors associated with the discretisation in FDM, but does not eliminate it completely, which in the case of a second order scheme means reducing error by a factor of 4 if the step size (Δx, Δy) is halved [64, 76].

Therefore, by doubling the amount of nodes for the discretisation of the smallest component in the AEC computational domain, i.e. increasing its resolution (subsection A.2), the differences between the total system's initial and final mass was reduced to less than 5%, justifying the choice of step sizes for Δx and Δy. The error may also be associated with the re-dissolution of the stored gas, e.g. oxygen re-dissolving from the flash tank into the electrolyte, which acts as a system source whose contribution is initially not accounted for and adds mass to the system over time.

The grid spacing step sizes were also further refined until a grid independent solution was obtained, that is to say, until an incremental difference in the final simulated solutions between a finer and a previous, more coarse mesh was achieved. The point at which smaller step sizes for Δx and Δy gave a less than 3% more accurate result was seen as a minimal improvement at the cost of a substantial increase in computational time, and grid refinement was stopped.

Checking Literature Parameters

To ensure the fluid property correlations adapted from Haug et al. were being implemented correctly [24] (Section A.2), conditions from their work were adopted to compare tabulated values when possible, such as for the saturation concentration of hydrogen in the cathodic chamber and the diffusion coefficient of hydrogen in KOH-solution. Differences of less than 3% arose and are attributed to rounding errors, generally confirming that the parameter equations were properly adapted.

Stability Issues

Due to the large difference in diffusion coefficients of O_2 in H_2 and in KOH (Eqn. A.7), there was a large difference in the maximum time steps in the gas phase and in the liquid phase in satisfying Eqn. 3.10. Therefore, to save computing time, the gas phase side and the liquid phase side have been integrated with different time steps.

$$\frac{D_{O_2,H_2}}{D_{O_2,KOH}} \approxeq 1300 \tag{A.7}$$

Validation of Physical Representation

Model validation through real AEC data was not possible as experimental and modeling research on system characterisation, its control scheme and crossover data is being conducted but has not yet been completed. The model, however, reflects real diffusion processes, proven through a more fundamental 1D model as well as through trends observed in results, discussed in subsection 4.2.2.

Justifying Assumptions

Ensuring credible assumptions and conditions are applied can further support the validity of the model [75].

- **Neglect of convective effects**. Convection is largely driven by the formation and interaction of bubbles within the electrolyte. Though residual bubbles will remain in solution, the effect of these is negligibly small in comparison to conditions during operation and will diminish as time progresses.

- **Isothermal and isobaric conditions**. Fluctuations in temperature and pressure are expected overnight, but through proper insulation, flow management and gas containment, constant conditions can be maintained.
- **Single cell basis**. Though only a single cell has been considered, estimations can provide an initial quantification on the extent of crossover and a starting point for model refinement. Furthermore, while it may not scale linearly to 20 cells, these results can help ZEF gauge the implications on the system safety, especially if one cell shows to reach dangerous conditions.

Supplemental Data on Hydrogen Crossover

As was similarly presented in subsection 4.2.4, the overnight crossover flux (Fig. A.4) and total gas accumulation (Fig. A.5) were examined in the case of hydrogen.

Brief Overview on Hydrogen Crossover Trends

Hydrogen crossover reaches a five time larger maximum flux value across the membrane when compared to that of oxygen (Fig. A.4). Furthermore, after eight hours, the membrane hydrogen flux for all chambers has reached values that are clearly lower than the flux observed in oxygen crossover, ranging from zero to three $\mu mol\, m^{-2}\, s^{-1}$. Although a flux is sustained longer in wider chambers as seen in oxygen crossover, in the given eight hour time frame, an (near-) equilibrium state is reached for all chamber widths. These trends indicate a faster diffusion process of hydrogen, where the effects of the opposing wall (see Subsection 4.2.3) are felt sooner as a result. This observation may be traced to (a) its higher solubility in KOH ($C^{cat}_{H_2,sat} = 3.73 mol/m^3$) , which may cause a larger driving force due to the higher concentration gradient between the two chambers, and (b) to its smaller molecular size, which gives rise to its larger diffusion coefficient ($D_{H_2,KOH} = 5.38 \times 10^{-9} m^2\, s^{-1}$) (compare to Table 4.2).

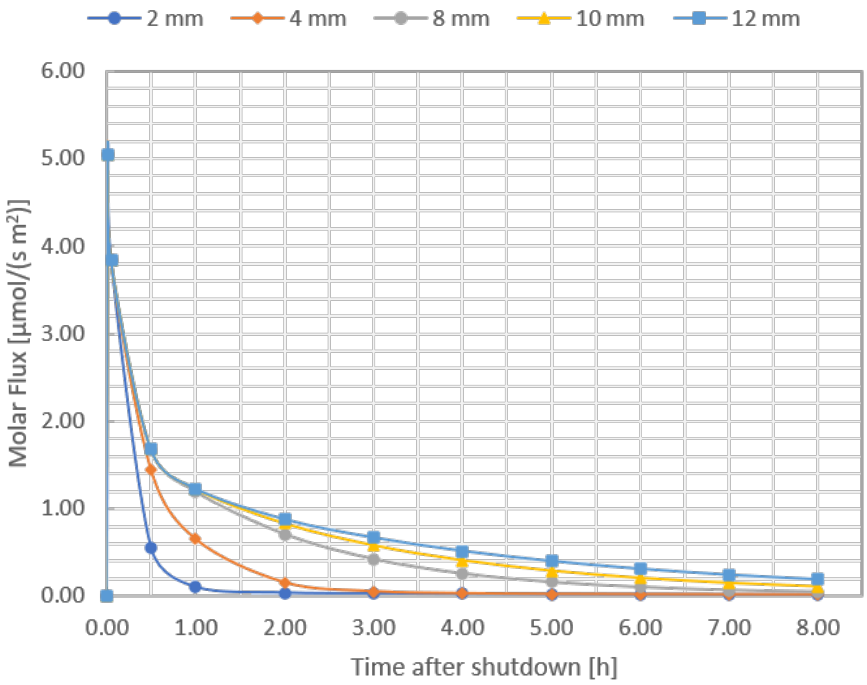

Figure A.4: Average molar flux of hydrogen across the membrane as a function of shutdown time and half-cell chamber width.

As a result, an overall larger accumulation of crossover gas is observed (Fig. A.5). At ZEF's design scale of 4 mm wide chambers, a more than 1.5 time larger accumulation of gas is observed in hydrogen than in oxygen, which plateaus around the three hour mark already. Furthermore, there is a more distinct separation of accumulation plots when compared to oxygen's accumulation profile across all chamber sizes. Generally, as is the case with oxygen crossover, the larger the chamber width, the larger the accumulated amount of hydrogen.

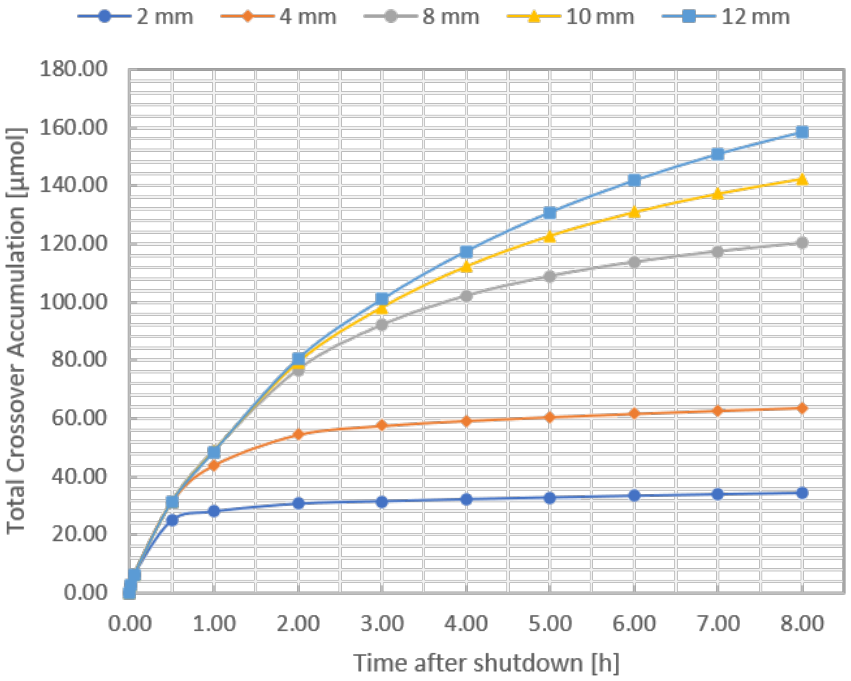

Figure A.5: Total hydrogen crossover accumulation as a function of shutdown time and half-cell chamber width.

Table A.5: Hydrogen crossover impurity levels in the oxygen flash tank, shown in mole percent. Values reflect expected crossover levels after eight hours for each chamber width in cases for single cell predictions and ZEF equivalent stack predictions.

Chamber Width	**Flash Tank H_2 Impurity**	
	Single Cell	ZEF Stack
[mm]	[mol%]	
2.00	0.011	0.214
4.00	0.020	0.396
8.00	0.037	0.744
10.00	0.044	0.880
12.00	0.049	0.978

Implications of Flash Tank Purity

Similar to oxygen crossover, hydrogen does not penetrate deep enough into the AEC components to contaminate the oxygen flash tank overnight, but simply accumulates in the chamber and outlet channel. Therefore, it was once again necessary to investigate what effect the accumulated hydrogen will have on the flash tank upon startup, assuming it were all to degas. Like in section 4.2.5, this was done for the case of both a single electrolytic cell and a full, 20-cell stack like ZEF's AEC. Results are depicted in Table A.5.

While higher impurity levels are observed here in the flash tank when compared to the oxygen contamination in the hydrogen buffer, dangerous levels are not reached, regardless of chamber size. Long-term accumulation within the oxygen flash tank is also unlikely as ZEF purges its volume contents continuously during operation. However, it is recommended to purge the flash tank upon start-up as well to further minimise the risk of an unforeseen build-up of trace hydrogen. Therefore, it can be concluded from first estimations on overnight crossover that trace hydrogen contamination represents a low safety risk in the AEC.

B

Supplementary Data and Derivations for Combustion Model

B.1. Data Validation and Recreation

Adiabatic Flame Temperature

Data for AFT at ambient conditions is depicted in Fig. B.1. Values at stoichiometry were compared to literature results in Warnatz et al.'s work [66].

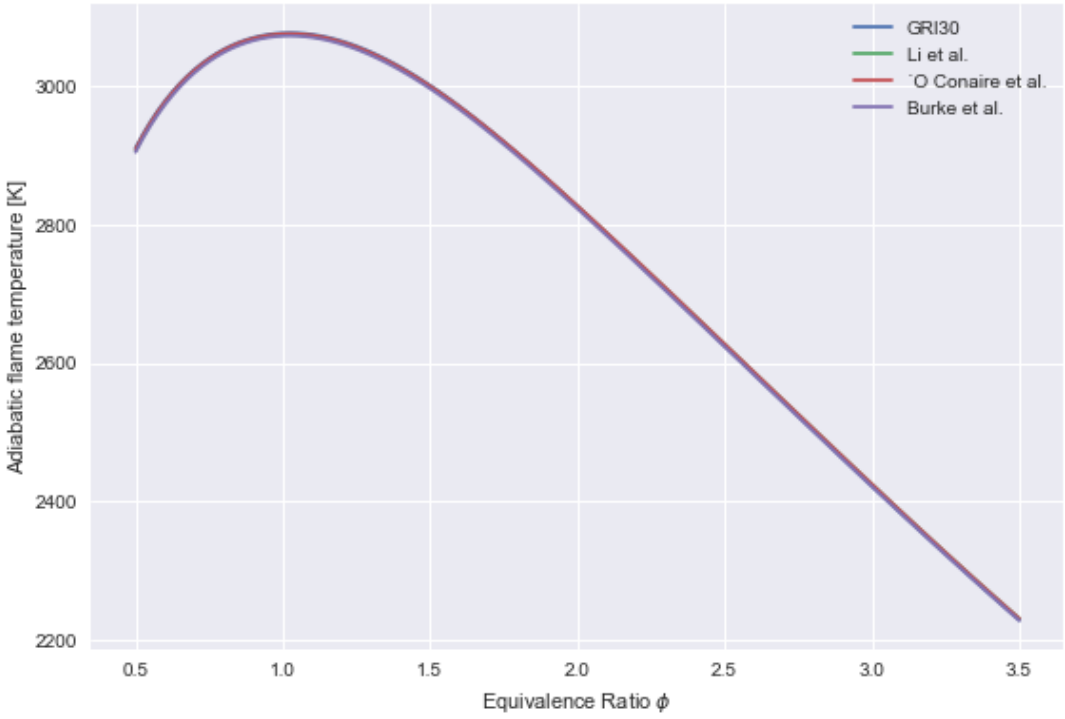

Figure B.1: Adiabatic flame temperature of the product gases as a function of the equivalence ratio ϕ. Mechanisms applied: [15–18]. Initial Inlet Conditions: 1 bar, 300 K.

Laminar Flame Speed

For a baseline reference, laminar flame speeds were examined at ambient conditions ($T = 298$K and $P = 1bar$) to compare and estimate the effects of an increase in temperature and pressure (Fig. B.2).

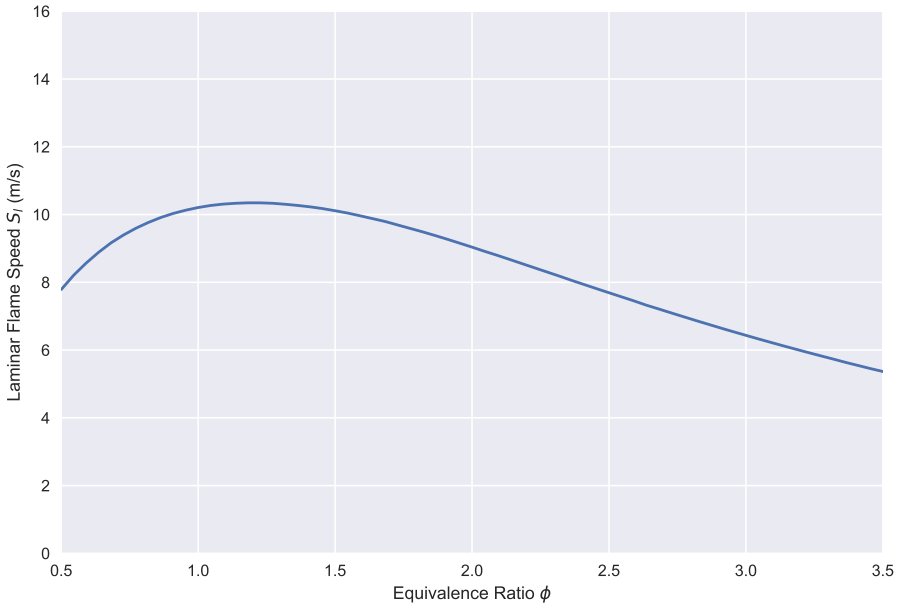

Figure B.2: Laminar flame speed as a function of equivalence ratio ϕ; based on Li et. al's mechanism [15]. Initial inlet conditions: 1 bar and 300 K.

Data recreated from Karimkashi et al.'s work (Fig. B.3) [65]:

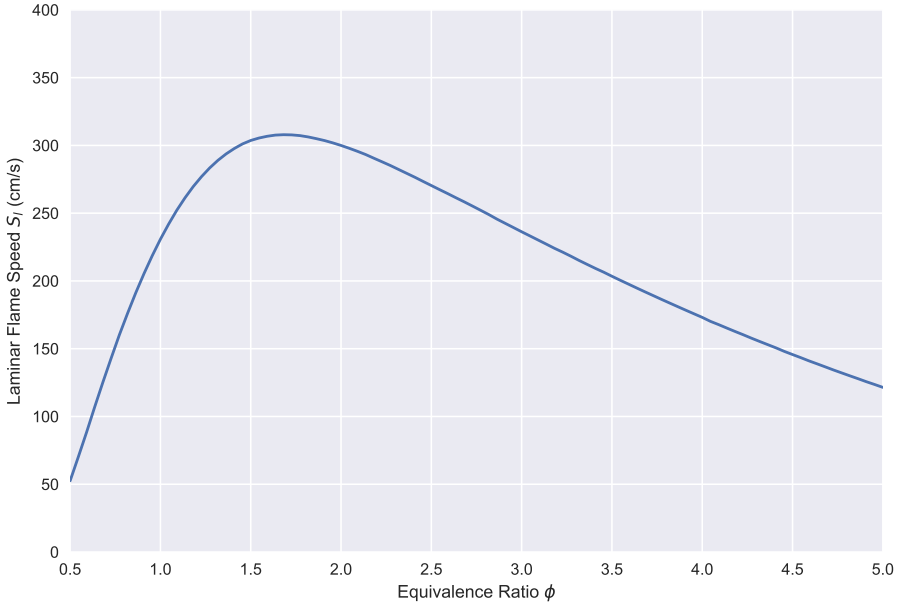

Figure B.3: Laminar flame speed versus the equivalence ratio for a H_2-air mixture. Li et al.'s mechanism was applied [15]. Initial Inlet Conditions: 1 bar, 300 K.

Data recreated from Warnatz et al.'s work (Fig. B.4) [66]:

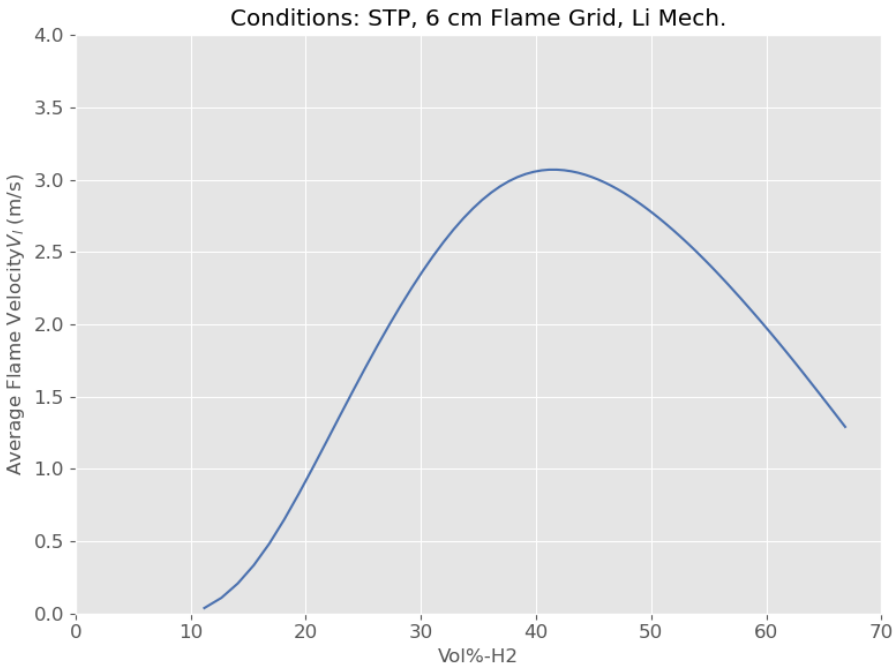

Figure B.4: Laminar flame speed of a H_2-air mixture as a function of the unburnt gas composition, expressed as the volume percent of hydrogen content $vol - \%H_2$; based on Li et. al's mechanism [15]. Initial inlet conditions: 1 bar and 298 K.

Data recreated for mass burning rate detailed in Burke et al.'s work (Fig. B.5) [17]:

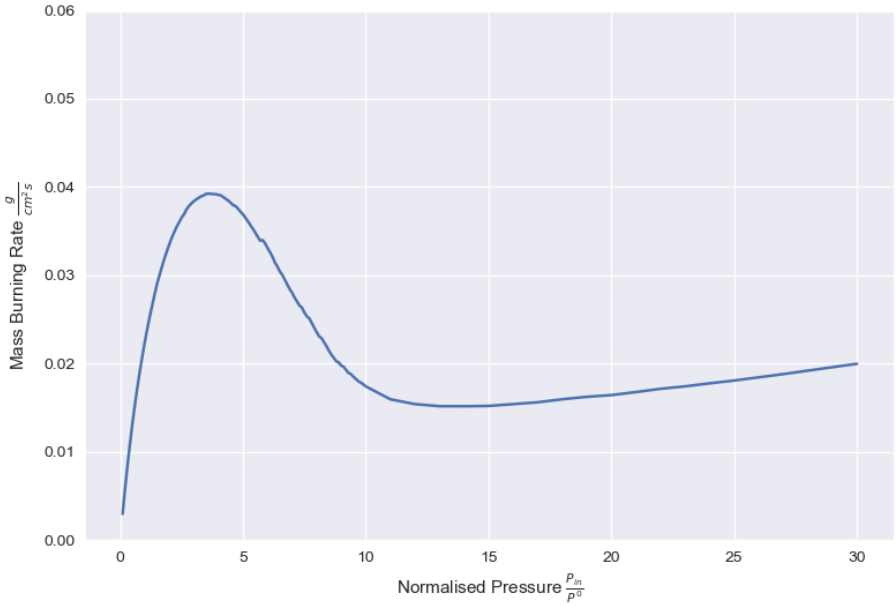

Figure B.5: Laminar mass burning rate pressure dependence for a H_2-O_2-He mixture. The equivalence ratio was set at $\phi = 0.3$ with the helium dilution adjusted to give an adiabatic flame temperature close to 1400K. Data was re-create from Burke et al.'s, applying the chemical mechanism from their work [17].

Ignition Delay Time

Data recreated from Karimkashi et al.'s work (Fig. B.6) [65].

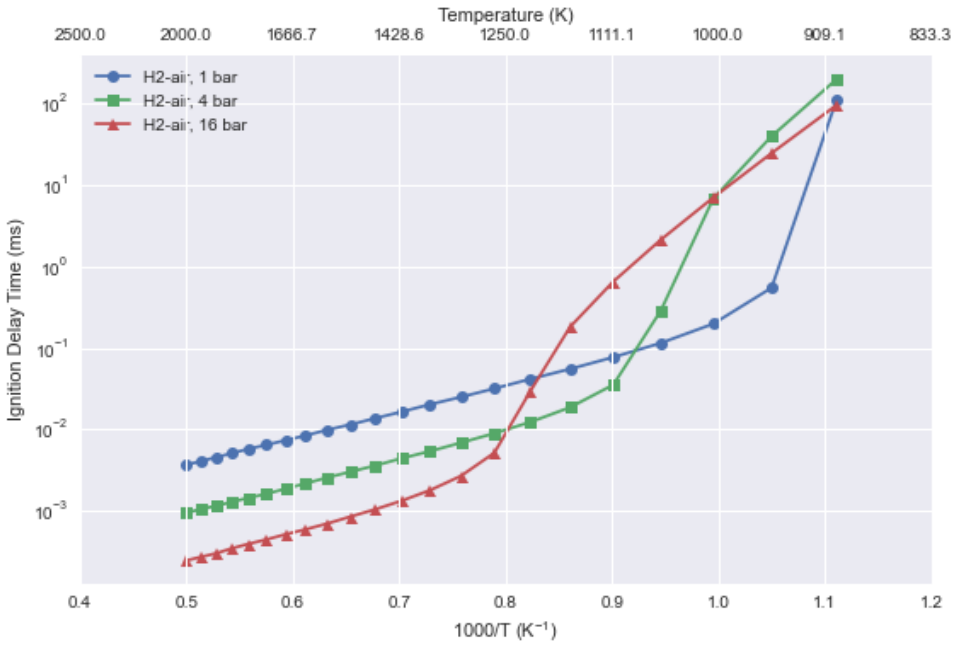

Figure B.6: H_2-air mixture at an equivalence ratio of $\phi = 0.5$ for pressures 1, 4 and 16 bar. Li et al.'s mechanism was applied [15].

Bibliography

[1] International Renewable Energy Agency, *Innovation Landscape For A Renewable-Powered Future: Solutions To Integrate Variable Renewables,* (2019).

[2] J. Benson, A. Celin, and A. Products, *Recovering Hydrogen-and Profits-from Hydrogen-Rich Offgas*, Tech. Rep. (Air Product).

[3] S. Yun and S. Ted Oyama, *Correlations in palladium membranes for hydrogen separation: A review,* Journal of Membrane Science **375**, 28 (2011).

[4] M. Trégaro, M. Rhandi, F. Druart, J. Deseure, and M. Chatenet, *Electrochemical hydrogen compression and purification versus competing technologies: Part II. Challenges in electrocatalysis,* Chinese Journal of Catalysis **41**, 770 (2020).

[5] *Design Safety Considerations for Water Cooled Small Modular Reactors Incorporating Lessons Learned from the Fukushima Daiichi Accident*, Tech. Rep. 1785 (Vienna, 2016).

[6] E. R. Delsman, *Microstructured Reactors for a Portable Hydrogen Production Unit*, Ph.D. thesis, Eindhoven University of Technology (2005).

[7] M. Nordio, F. Rizzi, G. Manzolini, M. Mulder, L. Raymakers, M. Van Sint Annaland, and F. Gallucci, *Experimental and modelling study of an electrochemical hydrogen compressor,* Chemical Engineering Journal **369**, 432 (2019).

[8] K. M. Inc., *Live palladium price,* (2015).

[9] P. C. Vesborg and T. F. Jaramillo, *Addressing the terawatt challenge: Scalability in the supply of chemical elements for renewable energy,* RSC Advances **2**, 7933 (2012).

[10] R. Phillips and C. W. Dunnill, *Zero gap alkaline electrolysis cell design for renewable energy storage as hydrogen gas,* RSC Advances **6**, 100643 (2016).

[11] D. Wiley and G. Fimbres Weihs, *Electroosmotic drag in membranes,* in *Encyclopedia of Membranes*, edited by E. Drioli and L. Giorno (Springer Berlin Heidelberg, Berlin, Heidelberg, 2016) pp. 653–654.

[12] P. Haug, B. Kreitz, M. Koj, and T. Turek, *Process modelling of an alkaline water electrolyzer,* International Journal of Hydrogen Energy **42**, 15689 (2017).

[13] P. Scardina and M. Edwards, *Chapter 1 the fundamentals of bubble formation in water treatment,* (2009).

[14] V. Schroeder and K. Holtappels, *Explosion Characteristics of Hydrogen-Air and Hydrogen-Oxygen Mixtures at Elevated Pressures,* in *International Conference on Hydrogen Safety* (Pisa, Italy, 2005).

[15] J. Li, Z. Zhao, A. Kazakov, and F. L. Dryer, *An updated comprehensive kinetic model of hydrogen combustion,* International Journal of Chemical Kinetics **36**, 566 (2004).

[16] M. Ó Conaire, H. J. Curran, J. M. Simmie, W. J. Pitz, and C. K. Westbrook, *A comprehensive modeling study of hydrogen oxidation,* International Journal of Chemical Kinetics **36**, 603 (2004).

[17] M. P. Burke, M. Chaos, Y. Ju, F. L. Dryer, and S. J. Klippenstein, *Comprehensive H2/O2 kinetic model for high-pressure combustion,* International Journal of Chemical Kinetics **44**, 444 (2012).

[18] D. G. Goodwin, R. L. Speth, H. K. Moffat, and B. W. Weber, *Cantera: An object-oriented software toolkit for chemical kinetics, thermodynamics, and transport processes,* `https://www.cantera.org` (2018), version 2.4.0.

[19] S. Gersen, *Experimental study of the combustion properties of methane/hydrogen mixtures*, Ph.D. thesis (2007).

[20] C. T. Eichler, *Flame Flashback in Wall Boundary Layers of Premixed Combustion Systems*, Ph.D. thesis, Technical University Munich (2011).

[21] M. Schalenbach, G. Tjarks, M. Carmo, W. Lueke, M. Mueller, and D. Stolten, *Acidic or Alkaline? Towards a New Perspective on the Efficiency of Water Electrolysis,* Journal of The Electrochemical Society **163**, F3197 (2016).

[22] Z. B.V., *Sunpower solar panels,* .

[23] K. M. Inc., *Live platinum price,* (2015).

[24] P. Haug, M. Koj, and T. Turek, *Influence of process conditions on gas purity in alkaline water electrolysis,* International Journal of Hydrogen Energy **42**, 9406 (2017).

[25] P. Haug, *Experimental and theoretical investigation of gas purity in alkaline water electrolysis*, Ph.D. thesis, Clausthal University of Technology (2019).

[26] G. Gahleitner, *Hydrogen from renewable electricity: An international review of power-to-gas pilot plants for stationary applications, International Journal of Hydrogen Energy*, **38**, 2039 (2013).

[27] M. Götz, J. Lefebvre, F. Mörs, A. McDaniel Koch, F. Graf, S. Bajohr, R. Reimert, and T. Kolb, *Renewable Power-to-Gas: A technological and economic review, Renewable Energy*, **85**, 1371 (2016).

[28] L. Bertuccioli, A. Chan, D. Hart, F. Lehner, B. Madden, and E. Standen, *Study on development of water electrolysis in the EU*, Tech. Rep. (2014).

[29] I. R. E. Agency, *Innovation landscape brief: Utility-scale batteries,* (2019).

[30] M. Carmo and D. Stolten, *Energy storage using hydrogen produced from excess renewable electricity: Power to hydrogen,* in *Science and Engineering of Hydrogen-Based Energy Technologies: Hydrogen Production and Practical Applications in Energy Generation* (Elsevier, 2018) pp. 165–199.

[31] J. Mergel and D. Stolten, *Challenges in water electrolysis and its development potential as a key technology for renewable energies,* ECS Meeting Abstracts (2012), 10.1149/ma2012-02/5/348.

[32] Z. Abdin, A. Zafaranloo, A. Rafiee, W. Mérida, W. Lipiński, and K. R. Khalilpour, *Hydrogen as an energy vector,* Renewable and Sustainable Energy Reviews **120** (2020), 10.1016/j.rser.2019.109620.

[33] International Renewable Energy Agency, *Global Renewables Outlook: Energy transformation 2050,* (2020).

[34] M. Rhandi, M. Trégaro, F. Druart, J. Deseure, and M. Chatenet, *Electrochemical hydrogen compression and purification versus competing technologies: Part I. Pros and cons,* Chinese Journal of Catalysis **41**, 756 (2020).

[35] K. Zeng and D. Zhang, *Recent progress in alkaline water electrolysis for hydrogen production and applications,* Progress in Energy and Combustion Science **36**, 307 (2010).

[36] M. Bodner, A. Hofer, and V. Hacker, *H2 generation from alkaline electrolyzer,* Wiley Interdisciplinary Reviews: Energy and Environment **4**, 365 (2015).

[37] D. Pletcher and X. Li, *Prospects for alkaline zero gap water electrolysers for hydrogen production,* International Journal of Hydrogen Energy **36**, 15089 (2011).

[38] L. Schorer, S. Schmitz, and A. Weber, *Membrane based purification of hydrogen system (MEMPHYS),* International Journal of Hydrogen Energy **44**, 12708 (2019).

[39] A. Gabelman, *Adsorption basics: Part 1,* Chemical Engineering Progress **113**, 1 (2017).

[40] A. Gabelman, *Adsorption basics: Part 2,* Chemical Engineering Progress **113**, 38 (2017).

[41] J. A. Delgado Dobladez, V. I. Águeda Maté, S. Á. Torrellas, M. Larriba, and P. Brea, *Efficient recovery of syngas from dry methane reforming product by a dual pressure swing adsorption process,* International Journal of Hydrogen Energy (2020), 10.1016/j.ijhydene.2020.02.153.

[42] G. Bernardo, T. Araújo, T. da Silva Lopes, J. Sousa, and A. Mendes, *Recent advances in membrane technologies for hydrogen purification,* International Journal of Hydrogen Energy **45**, 7313 (2020).

[43] P. Bouwman, *Electrochemical Hydrogen Compression (EHC) solutions for hydrogen infrastructure,* Fuel Cells Bulletin **2014**, 12 (2014).

[44] C. Casati, P. Longhi, L. Zanderighi, and F. Bianchi, *Some fundamental aspects in electrochemical hydrogen purification/compression,* Journal of Power Sources **180**, 103 (2008).

[45] R. J. Spiegel, *Platinum and fuel cells,* Transportation Research Part D: Transport and Environment **9**, 357 (2004).

[46] O. T. Holton and J. W. Stevenson, *The Role of Platinum in Proton Exchange Membrane Fuel Cells Evaluation of platinum's unique properties for use in both the anode and cathode of a proton exchange membrane fuel cell,* Platinum Metals Review **57**, 259 (2013).

[47] V. Shepelin, D. Koshmanov, and E. Chepelin, *Catalyst for recombination of hydrogen and oxygen in confined spaces under high concentrations of hydrogen,* Nuclear Technology **178**, 29 (2012).

[48] E. Lopez-Alonso, D. Papini, and G. Jimenez, *Hydrogen distribution and Passive Autocatalytic Recombiner (PAR) mitigation in a PWR-KWU containment type,* Annals of Nuclear Energy **109**, 600 (2017).

[49] J. Xiao, Z. Zhou, and X. Jing, *Safety implementation of hydrogen igniters and recombiners for nuclear power plant severe accident management,* Tsinghua Science and Technology **11**, 549 (2006).

[50] H. Karwat, *Ignitors To Mitigate The Risk Of Hydrogen Explosions - A Critical Review,* Nuclear Engineering and Design **118**, 267 (1990).

[51] H. Saitoh, T. Otsuka, N. Yoshikawa, N. Kanno, S. Takanashi, Y. Oozawa, M. Hirata, M. Takeshita, K. Sakuragi, S. Kurihara, Y. Tsunashima, N. Aoki, and K. Tanaka, *Development of a mitigation system against hydrogen-air deflagrations in nuclear power plants,* Journal of Loss Prevention in the Process Industries **60**, 9 (2019).

[52] N. Aeronautics and S. Administration, *Nasa's flair for flare: Engineers test hydrogen burn-off igniters for space launch system,* (2015).

[53] D. A. Crowl and Y. D. Jo, *The hazards and risks of hydrogen,* Journal of Loss Prevention in the Process Industries **20**, 158 (2007).

[54] M. T. Janicke, H. Kestenbaum, U. Hagendorf, F. Schüth, M. Fichtner, and K. Schubert, *The Controlled Oxidation of Hydrogen from an Explosive Mixture of Gases Using a Microstructured Reactor/Heat Exchanger and Pt/Al2O3 Catalyst,* Journal of Catalysis **191**, 282 (2000).

[55] V. Hessel, S. Hardt, and H. Löwe, *Chemical Micro Process Engineering: Fundamentals, Modelling and Reactions*, 1st ed. (Wiley-VCH Verlag GmbH & Co. KGaA, Weinheim, 2004) pp. 295–417.

[56] A. Mehra and I. A. Waitz, *Development of a hydrogen combustor for a microfabricated gas turbine engine,* , 35 (1998).

[57] P. Trinke, P. Haug, J. Brauns, B. Bensmann, R. Hanke-Rauschenbach, and T. Turek, *Hydrogen Crossover in PEM and Alkaline Water Electrolysis: Mechanisms, Direct Comparison and Mitigation Strategies,* Journal of The Electrochemical Society **165**, F502 (2018).

[58] M. Schalenbach, W. Lueke, and D. Stolten, *Hydrogen Diffusivity and Electrolyte Permeability of the Zirfon PERL Separator for Alkaline Water Electrolysis,* Journal of The Electrochemical Society **163**, F1480 (2016).

[59] M. R. Kraglund, *Alkaline membrane water electrolysis with non-noble catalysts*, Ph.D. thesis, Technical University of Denmark (2017).

[60] H. Vogt, *On the supersaturation of gas in the concentration boundary layer of gas evolving electrodes,* Electrochimica Acta **25**, 527 (1980).

[61] H. M. Wedershoven, R. M. de Jonge, C. W. Sillen, and S. J. van Stralen, *Behaviour of oxygen bubbles during alkaline water electrolysis,* International Journal of Heat and Mass Transfer **25**, 1239 (1982).

[62] M. Sánchez, E. Amores, D. Abad, L. Rodríguez, and C. Clemente-Jul, *Aspen Plus model of an alkaline electrolysis system for hydrogen production,* International Journal of Hydrogen Energy **45**, 3916 (2020).

[63] S. Gurevich, *Lecture Notes in Numerical Methods For Complext System I on the Diffusion Equation,* (2016).

[64] S. C. Chapra and R. P. Canale, *Numerical Methods for Engineers*, 6th ed. (McGraw-Hill, New York, 2010) pp. 1–968.

[65] S. Karimkashi, H. Kahila, O. Kaario, M. Larmi, and V. Vuorinen, *Numerical study on tri-fuel combustion: Ignition properties of hydrogen-enriched methane-diesel and methanol-diesel mixtures,* International Journal of Hydrogen Energy **45**, 4946 (2020).

[66] J. Warnatz, U. Maas, and R. W. Dibble, *Combustion - Physical and Chemical Fundamentals, Modeling and Simulation, Experiments, Pollutant Formation*, 4th ed. (Springer-Verlag Berlin Heidelberg, 2006) pp. 1–378.

[67] S. S. Grossel, *Overview of combustion and flame propagation phenomena related to ddas,* in *Deflagration and Detonation Flame Arresters* (John Wiley Sons, Ltd, 2010) Chap. 4, pp. 51–75, https://onlinelibrary.wiley.com/doi/pdf/10.1002/9780470935651.ch4 .

[68] E. L. Cussler, *Diffusion - Mass Transfer in Fluid Systems*, 3rd ed. (Cambridge University Press, Cambridge, 2009).

[69] J. R. Welty, G. L. Rorrer, and D. G. Foster, *Fundamentals of Momentum, Heat, and Mass Transfer*, 6th ed. (John Wiley & Sons, Inc., 2015) p. 770, arXiv:arXiv:1011.1669v3 .

[70] I. Glassman and R. A. Yetter, *Chapter 3 - explosive and general oxidative characteristics of fuels,* in *Combustion (Fourth Edition)*, edited by I. Glassman and R. A. Yetter (Academic Press, Burlington, 2008) fourth edition ed., pp. 75 – 145.

[71] C. K. Law, T. F. Lu, and A. Makino, *On the off-stoichiometric peaking of adiabatic flame temperature,* Combustion and Flame **145** (2006), 10.1016/j.combustflame.2006.01.009.

[72] A. Shukla, A. K. Singh, and P. Singh, *A Comparative Study of Finite Volume Method and Finite Difference Method for Convection-Diffusion Problem,* American Journal of Computational and Applied Mathematics **1**, 67 (2012).

[73] M. Schalenbach, M. Carmo, D. L. Fritz, J. Mergel, and D. Stolten, *Pressurized pem water electrolysis: Efficiency and gas crossover,* International Journal of Hydrogen Energy **38**, 14921 (2013).

[74] M. Schalenbach, T. Hoefner, P. Paciok, M. Carmo, W. Lueke, and D. Stolten, *Gas permeation through nafion. part 1: Measurements,* The Journal of Physical Chemistry C **119**, 25145 (2015), https://doi.org/10.1021/acs.jpcc.5b04155 .

[75] R. G. Sargent, *Verification and validation of simulation models,* in *Proceedings of the 2010 Winter Simulation Conference*, Vol. 37 (2011) pp. 166–183.

[76] T. J. Craft, *Lecture Slides on Finite Difference Schemes for Computational Fluid Dynamics I,* (2010).